

IN 33-CR
51308
P-139

**ELECTROMAGNETIC COMMUNICATION LABORATORY
SCIENTIFIC REPORT NO. 95-1**

June 1995

**EFFICIENT MODELING OF INTERCONNECTS AND
CAPACITIVE DISCONTINUITIES
IN HIGH-SPEED DIGITAL CIRCUITS**

**K. S. Oh and Jose Schutt-Aine
University of Illinois, Urbana-Champaign**

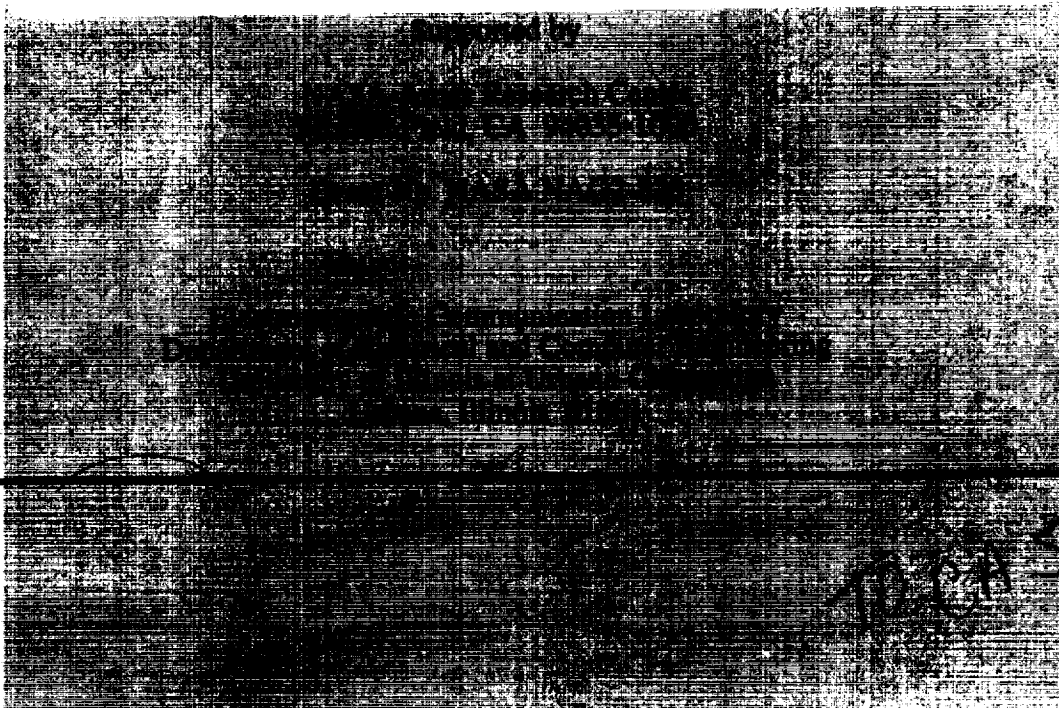


(NASA-CR-198728) EFFICIENT
MODELING OF INTERCONNECTS AND
CAPACITIVE DISCONTINUITIES IN
HIGH-SPEED DIGITAL CIRCUITS Thesis
(Illinois Univ.) 139 p

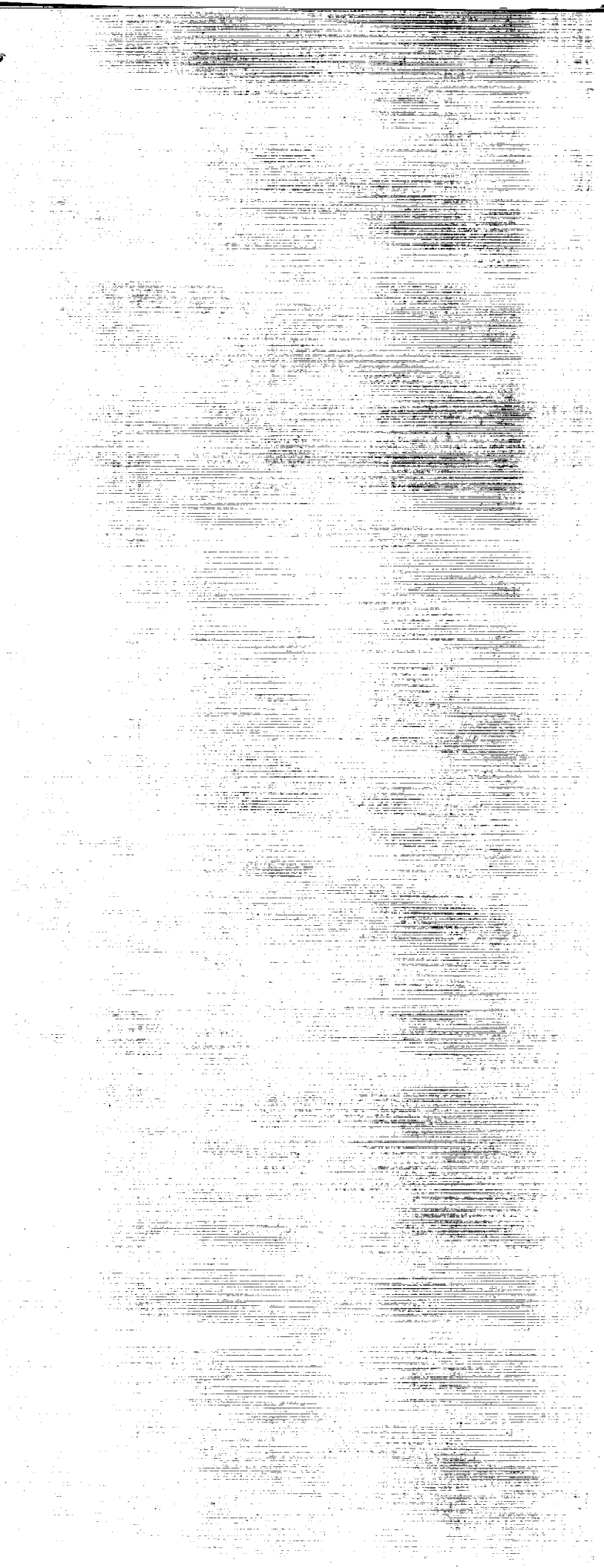
N95-28570

Unclas

G3 1/33 0051808



Vertical text or barcode on the left edge of the page.



UILU-ENG-95-2544

Electromagnetic Communication Laboratory Report No. 95-1

**EFFICIENT MODELING OF INTERCONNECTS AND CAPACITIVE
DISCONTINUITIES IN HIGH-SPEED DIGITAL CIRCUITS**

**K. S. Oh and J. Schutt-Aine
University of Illinois
Urbana, Illinois**

Scientific Report

June 1995

Supported by

NASA-Ames Research Center
Moffett Field, CA 94035-1000

Grant No. NASA NAG2-823

Electromagnetic Communication Laboratory
Department of Electrical and Computer Engineering
Engineering Experiment Station
University of Illinois at Urbana-Champaign
Urbana, Illinois 61801



PRECEDING PAGE BLANK NOT FILMED

ABSTRACT

With the recent advances in high-speed digital circuits, modeling of interconnects and associated discontinuities has gained a considerable interest over the last decade although the theoretical bases for analyzing these structures were well-established as early as the 1960s. Ongoing research at the present time is focused on devising methods which can be applied to more general geometries than the ones considered in earlier days and, at the same time, improving the computational efficiency and accuracy of these methods.

In this thesis, numerically efficient methods to compute the transmission line parameters of a multiconductor system and the equivalent capacitances of various strip discontinuities are presented based on the quasi-static approximation. The presented techniques are applicable to conductors embedded in an arbitrary number of dielectric layers with two possible locations of ground planes at the top and bottom of the dielectric layers. The cross-sections of conductors can be arbitrary as long as they can be described with polygons.

An integral equation approach in conjunction with the collocation method is used in the presented methods. A closed-form Green's function is derived based on weighted real images thus avoiding nested infinite summations in the exact Green's function; therefore, this closed-form Green's function is numerically more efficient than the exact Green's function. All elements associated with the moment matrix are computed using the closed-form formulas. Various numerical examples are considered to verify the presented methods, and a comparison of the computed results with other published results showed good agreement.

TABLE OF CONTENTS

CHAPTER	PAGE
1 INTRODUCTION.....	1
1.1 Background.....	1
1.2 The Quasi-Static Approximation.....	2
1.3 Electrostatic Solution Techniques	2
1.4 Structure of the Thesis.....	4
1.5 References	6
2 DERIVATION OF THE CLOSED-FORM GREEN'S FUNCTION FOR A MULTILAYERED DIELECTRIC MEDIUM.....	10
2.1 Introduction.....	10
2.2 Derivation of the Spectral-Domain Green's function.....	11
2.3 Derivation of the Space-Domain Green's function	16
2.3.1 Closed-form Green's functions for geometries without any ground planes or only with the bottom ground plane	18
2.3.2 Closed-form Green's functions for geometries with both top and bottom ground planes	21
2.4 Closed-form Integration Formulas for the Elements of Moment Matrices.....	23
2.5 The Comparison of the Exact and Approximate Green's Functions.....	25
2.6 Physical Interpretation of the Closed-Form Green's Functions	33
2.7 Summary.....	35
2.8 References	35
3 COMPUTATION OF THE TRANSMISSION PARAMETERS OF A MULTICONDUCTOR SYSTEM	37
3.1 Introduction.....	37
3.2 Computation of the Capacitance Matrix.....	39
3.2.1 Theory	39

3.2.2	Numerical examples	43
3.3	Computation of the Inductance Matrix	48
3.3.1	Isomorphism between electrostatic and magnetostatic problems ...	49
3.3.2	Numerical examples	52
3.4	Computation of the Conductance Matrix	52
3.4.1	Theory	52
3.4.2	Numerical examples	56
3.5	Computation of the Resistance Matrix	60
3.5.1	Theory	60
3.5.2	Losses due to imperfectly conducting ground planes	65
3.5.3	Remarks on the various methods used in the computation of the resistance matrix	68
3.5.4	Numerical examples	69
3.6	Summary	73
3.7	References	73
4	COMPUTATION OF THE EQUIVALENT CAPACITANCES OF VARIOUS STRIP DISCONTINUITIES: AN OPEN END, A BEND, AND VARIOUS JUNCTIONS	76
4.1	Introduction	76
4.2	General Statement of the Problem	78
4.3	Formulation of an Integral Equation	78
4.4	Numerical Examples	84
4.5	Summary	85
4.6	References	92
5	COMPUTATION OF THE EQUIVALENT CAPACITANCE OF A VIA IN A MULTILAYERED BOARD	94
5.1	Introduction	94
5.2	General Statement of the Problem	95

5.3	Formulation of an Integral Equation	95
5.4	Numerical Examples	100
5.5	Summary	102
5.6	References	104
6	COMPUTATION OF THE EQUIVALENT CAPACITANCE OF A STRIP CROSSOVER IN A MULTILAYERED MEDIUM	105
6.1	Introduction	106
6.2	General Statement of the Problem	107
6.3	Formulation of an Integral Equation	108
6.4	The Fast Multipole Method (FMM)	113
6.5	Numerical Examples	115
6.6	Summary	122
6.7	References	123
7	SUMMARY AND FUTURE WORK	125
	APPENDIX A THE REAL-VALUED EXPONENTIAL APPROXIMATION BASED ON THE RELAXATION OF CURVE FITTING	128
	A.1 References	131
	APPENDIX B THE GREEN'S FUNCTION EXPRESSION FOR A STRIP LINE	132
	B.1 References	133

CHAPTER 1

INTRODUCTION

1.1 Background

In recent years, the numerical modeling and simulation of interconnections and their discontinuities in digital integrated circuits have gained significant interest due to the modern development of VLSI technology. As the complexity, density, and speed of the integrated circuits continue to increase, signal delay and rise times are increasingly limited by interconnections rather than device speeds, and accurate estimations of the signal delay and distortion due to interconnections become crucial at virtually every level of circuit integration.

To accurately characterize signal delay distortion and crosstalk noise due to interconnection lines, interconnects must be modeled as multiconductor transmission lines instead of conventional lumped circuit elements, and associated discontinuities, such as crossovers, bends, junctions, and vias, must also be accurately modeled. Although a substantial amount of work has been performed over the last three decades to characterize interconnections and their discontinuities in the electromagnetic community [1]-[3], most of these theoretical studies resulted in methods which involve high computational cost and, hence, are not suitable for the real-time design of CAD tools.

To overcome this difficulty associated with the theoretical analysis, a model-based interconnect capacitance extraction tool is studied in the circuit community [4]-[6]. In the model-based approach, analytical or table-look-up models are fitted to the data generated by numerical simulation of EM-based techniques or experimental measurements. Although this approach may reduce the time to compute parameters associated with interconnects, it requires an impractical number of models, which limits its practical usage. Fortunately, even when the layout of a circuit is very complex, the number of distinct interconnections and their discontinuities is often very limited; furthermore, an accurate characterization of interconnects is required only for the critical components (path) in the circuit. Thus, if a method based on the electromagnetic analysis is sufficiently fast, it may be incorporated into a layout CAD tool.

This thesis focuses on the discussion of computationally efficient methods for interconnection modeling. In particular, this thesis presents methods based on the quasi-

static approximation to compute the transmission parameters of a multiconductor interconnection line and the equivalent capacitances of interconnection discontinuities embedded in a multilayered dielectric medium.

1.2 The Quasi-Static Approximation

A multiconductor transmission line in a multilayered dielectric medium does not support TEM modes due to the inhomogeneity of a dielectric medium [7], and full-wave analysis must be considered to accurately characterize hybrid modes in the transmission line. However, when the transverse components of the electric and magnetic fields are predominant over the longitudinal components, the fundamental hybrid mode becomes a quasi-TEM mode, in which TEM properties dominate the hybrid modes, and lines which support a quasi-TEM mode are called quasi-TEM lines (similarly, lines supporting a TEM mode are called TEM lines.) The valid range of a quasi-TEM mode is often determined using the dimensional analysis on the Maxwell equations [8], [9]. For most quasi-TEM lines, a quasi-TEM mode is valid up to several gigahertz; particularly, it is valid up to the cutoff frequency of the next higher (hybrid) mode.

Since the electric field distribution of a TEM mode is identical to that of the static case [ch. 3, 10] and static analysis is simpler and computationally less intensive than full-wave analysis, quasi-TEM lines are often analyzed using a static analysis, which is then called the quasi-static approximation. All methods presented in this thesis are based on this quasi-static approximation. It should be noted that although not all transmission lines are quasi-TEM lines, interconnections encountered in digital integrated circuits belong to quasi-TEM lines

1.3 Electrostatic Solution Techniques

Under the quasi-static approximation, the analysis of interconnects and discontinuities is performed by solving electrostatic and magnetostatic problems. As will be discussed in Chapter 3, for two-dimensional problems, for example, solving for the transmission parameters of interconnects, there exists an analogy between electrostatic and magnetostatic problems; therefore, the solutions of two-dimensional magnetostatic problems can be obtained by solving the equivalent electrostatic problems. Furthermore, since this thesis focuses on the modeling of only the capacitive nature of discontinuities for three-dimensional problems, electrostatic solution techniques are sufficient for analyzing the problems considered in this thesis.

Electrostatic problems are governed by Laplace's equation or Poisson's equation with appropriate boundary conditions. Various methods have been employed to obtain the solution in two-dimensional space [11]-[19]. Two commonly used techniques for both 2-D and 3-D are integral equation methods [20], [21] and the domain methods, such as the finite difference method (FD) [22] and finite element method (FEM) [23], [24].

In the domain methods, the unknown potential distribution is solved to compute the charge distribution over an entire domain by either directly approximating the differential equation with the finite difference equation (FD) or using the equivalent variational expression in conjunction with the method of subareas (FEM). The major disadvantage of the domain methods is that the unknown potential distribution to be sought is over the entire geometry considered, including the dielectric region; hence, it may be computationally inefficient for the open geometry case even with the use of absorbing boundary conditions to truncate the open geometry. The computational inefficiency of the finite difference method is improved by employing the method of line (MoL) [25], [26]. In MoL, all but one of the independent variables of Laplace's equation are discretized to obtain a system of ordinary linear differential equations. These ordinary differential equations are then decoupled using the orthogonal transformation matrix and solved analytically. Although MoL is computationally very efficient for two-dimensional problems, it is still burdensome for three-dimensional problems. Moreover, this method is only applicable to infinitely thin conductors.

On the other hand, the conventional integral equation approach first obtains the Green's function for a layered medium using the image theory, which consists of rather slowly converging infinite series. Then, an integral equation is formulated using this Green's function as its kernel and is solved by employing the method of moments (MoM) to determine the unknown charge density on the conductor surfaces. Since unknowns in this approach only lie on the surface of conductors, methods based on an integral equation, in general, are more efficient than the domain methods. As noted in [12], for N layers, the expression for the Green's function would consist of a nested $N-1$ infinite series; hence, the evaluation of this Green's function is somewhat computationally burdensome. Alternatively, the free-space Green's function is used in [12] and [13] to avoid infinite series, but additional unknown charges on the dielectric interface and ground planes on top of the unknown charges on the conductor surface must be included, resulting in a larger moment matrix. Yet another approach to avoid an infinite summation is to solve the

integral equation in the spectral domain (SDA) [27], where the Green's function is in a closed form; however, this approach can not be applied to conductors with finite thicknesses, such as MoL.

In this thesis, the spatial closed-form Green's function is used to avoid the evaluation of an infinite series without any additional unknowns used in the method based on the free-space Green's function. A closed-form Green's function for a multilayered dielectric medium was first introduced in [28]. This Green's function utilizes a finite number of weighted complex images instead of an infinite number of real images required for the exact Green's function. A closed-form Green's function based on a finite number of weighted real images is first proposed in this thesis to avoid the use of expensive complex operations.

1.4 Structure of the Thesis

As mentioned in the previous section, the technique to solve an electrostatic problem (Laplace's equation) plays an important role in the quasi-TEM analysis, and methods based on an integral equation are used throughout this thesis to solve various electrostatic problems related to interconnections and discontinuities. All the integral equations encountered in this thesis are solved using the method of moments (MoM) [29], [30] with pulse basis functions and point matching (delta testing), and the moment matrices associated with the integral equations are constructed using an analytical formula for most cases, avoiding numerical integration or infinite summations.

The core of an integral equation approach is the determination of the Green's function. The exact Green's function for a multilayered medium is often obtained by using the image theory, and it consists of an infinite number of images. Chapter 2 discusses an efficient expression of this Green's function based on numerical approximation. This new expression of the approximate Green's function uses only a finite number of images; hence, it is in a closed form. To obtain this closed-form expression, the spectral-domain Green's function is first derived in this chapter; then, the spectral-domain Green's function is approximated with real-valued exponential functions using the method based on the relaxation of curve fitting. The closed-form Green's functions for a point, line, and semi-infinite line charges are then obtained by analytically converting the approximate spectral-domain Green's function to the space domain.

Chapter 3 discusses the computation of the four parameters of a multiconductor transmission line, viz., the capacitance matrix \mathbf{C} , the inductance matrix \mathbf{L} , the resistance matrix \mathbf{R} , and the conductance matrix \mathbf{G} . The capacitance matrix \mathbf{C} is computed from the free charge distribution on the surface of conductors, which is determined from the electrostatic analysis. To compute the inductance matrix \mathbf{L} , an analogy between electrostatic and magnetostatic problems for uniform transmission line configurations is used. Hence, the conduction surface current distribution is computed by solving the equivalent electrostatic problem and then used to compute \mathbf{L} .

The resistance matrix \mathbf{R} is also computed from the current distribution used in the computation of the inductance matrix by performing the perturbation analysis on this current distribution. Conventionally, the resistance matrix is defined in terms of power loss on conductors. The resulting matrix is nondiagonal in nature and is strongly dependent on the current excitations used in the computation. Thus, if the resistance matrix is obtained before the actual current distribution on the conductor has been determined, the result would not be too meaningful. In this chapter, the diagonal resistance matrix is defined in a manner such that it is relatively insensitive to the choice of current excitations compared to the nondiagonal resistance matrix, which is often computed using the perturbation on attenuation constants [31]. In addition to losses on the conductor traces, those due to imperfectly conducting ground planes are also incorporated into the resistance matrix.

The remaining transmission parameter, the conductance matrix \mathbf{G} , models dielectric losses and can be computed from the shunt current density. Since this current density is related to the normal component of the electric field at the surface of a conductor, which, in turn, is related to the surface charge density, the shunt current density can be obtained from the surface charge density of the lossless system when losses due to the imperfect dielectric media are small.

Chapter 4 is devoted to modeling of various strip discontinuities. In particular, a method to compute the equivalent (excess) capacitance of junction discontinuities, such as open ends, step junctions, bends, and T-junctions, are presented. Unlike other approaches, only one integral equation is employed to handle the above discontinuities instead of formulating a different integral equation for each discontinuity type. The integral equation is formulated in terms of the excess charge distribution to avoid the numerical

instabilities associated with the total charge formulation, where the integral equation is formulated in terms of the total charge distribution [21].

Chapters 5 and 6 discuss the modeling of yet other discontinuity types, vias and crossovers, respectively. These discontinuities differ from the ones discussed in Chapter 4 since conductor traces in these discontinuities could be located in the different dielectric layers. Furthermore, for a crossover case, traces are no longer electrically connected; hence, the equivalent capacitance of a crossover contains a mutual term in addition to two self-terms, and the coupled integral equations have to be solved instead of a single integral equation. Again, all integral equations are formulated in terms of the excess charge distributions. The utilization of the Fast Multipole Method (FMM) [32]-[36] in accelerating the MoM-based computation of the excess capacitance of a crossover is also considered in Chapter 6.

Finally, the conclusions and some future work evolving from this thesis are presented in Chapter 7.

1.5 References

- [1] K. C. Gupta, R. Gary, and I. J. Bahl, *Microstrip Lines and Slotlines*. Norwood, MA: Artech House, 1979.
- [2] T. C. Edwards, *Foundations for Microstrip Circuit Design*, 2nd ed. New York, NY: Wiley, 1992.
- [3] T. Itoh, Ed., *Planar Transmission Line Structures*. New York, NY: IEEE Press, 1987.
- [4] K.-J. Chang, S.-Y. Oh, and K. Lee, "HIVE: an efficient interconnect capacitance extractor to support submicron multilevel interconnect designs," *IEEE International Conference on Computer-Aided Design*, pp. 294-297, 1991 .
- [5] J. Chem, J. Huang, L. Arledge, P. C. Li, and P. Yang, "Multilevel metal capacitance for CAD design synthesis systems," *IEEE Electron Device Lett.*, vol. 13, pp. 32-34, January 1992.
- [6] U. Choudhury and A. Sangiovanni-Vincentelli, "An analytical-model generator for interconnect capacitances," *Proc. Custom Integrated Circuit Conference*, 1991.
- [7] R. K. Hoffmann, *Handbook of Microwave Integrated Circuits*. Norwood, MA: Artech House, 1987.

- [8] I. V. Lindell, "On the quasi-TEM modes in inhomogeneous multiconductor transmission lines," *IEEE Trans. Microwave Theory Tech.*, vol. 29, pp. 812-817, August 1981.
- [9] M. Horno, R. L. Mesa, F. Medina, and R. Marques, "Quasi-TEM analysis of multilayered multiconductor coplanar structures with dielectric and magnetic anisotropy including substrate losses," *IEEE Trans. Microwave Theory Tech.*, vol. 38, pp. 1059-1068, August 1990.
- [10] R. E. Collin, *Field Theory of Guided Waves*, 2nd ed. New York, NY: IEEE Press, 1991.
- [11] W. T. Weeks, "Calculation of coefficients of capacitance of multiconductor transmission lines in the presence of a dielectric interface," *IEEE Trans. Microwave Theory Tech.*, vol. 18, pp. 35-43, January 1970.
- [12] C. Wei, R. F. Harrington, J. R. Mautz, and T. K. Sarkar, "Multiconductor transmission lines in multilayered dielectric media," *IEEE Trans. Microwave Theory Tech.*, vol. 32, pp. 439-450, April 1984.
- [13] G. W. Pan, G. Wang, and B. K. Gilbert, "Edge effect enforced boundary element analysis of multilayered transmission lines," *IEEE Trans. Circuits Syst.*, vol. 39, pp. 955-963, November 1992.
- [14] W. Delbare and D. D. Zutter, "Space-domain Green's function approach to the capacitance calculation of multiconductor lines in multilayered dielectrics with improved surface charge modeling," *IEEE Trans. Microwave Theory Tech.*, vol. 37, pp. 1562-1568, October 1989.
- [15] E. Yamashita, "Variational method for the analysis of microstrip-like transmission lines," *IEEE Trans. Microwave Theory Tech.*, vol. 16, pp. 529-535, May 1964.
- [16] H. A. Wheeler, "Transmission line properties of parallel wide strips by a conformal mapping approximation," *IEEE Trans. Microwave Theory Tech.*, vol. 12, pp. 280-289, May 1964.
- [17] J. Svacina, "Analysis of multilayer microstrip lines by a conformal mapping method," *IEEE Trans. Microwave Theory Tech.*, vol. 40, pp. 769-772, April 1992.
- [18] A. Farrar and A. T. Adams, "Multilayer microstrip transmission lines," *IEEE Trans. Microwave Theory Tech.*, vol. 12, pp. 889-891, October 1974.
- [19] W. E. Matzke, B. Heinemann, and Telschow, "On the calculation of the capacitance coefficients for VLSI multilevel metallization lines by using domain methods," *IEEE Trans. Electron. Devices*, vol. 36, pp. 447-449, February 1989.
- [20] S. Papatheodorou, R. F. Harrington, and J. R. Mautz, "The equivalent circuit of a microstrip crossover in a dielectric substrate," *IEEE Trans. Microwave Theory Tech.*, vol. 38, pp. 135-140, February 1990.

- [21] P. Benedek and P. Silvester, "Equivalent capacitances for microstrip gaps and steps," *IEEE Trans. Microwave Theory Tech.*, vol. 20, pp. 729-733, November 1972.
- [22] N. N. Rao, *Elements of Engineering Electromagnetics*, 3rd ed. Englewood Cliffs, NJ: Prentice Hall, 1991.
- [23] P. P. Silvester and R. L. Ferrari, *Finite Elements for Electrical Engineers*, 2nd ed. New York, NY: Cambridge, 1990.
- [24] J. Jin, *The Finite Element Method in Electromagnetics*. New York, NY: Wiley, 1993.
- [25] T. Itoh, Ed., *Numerical Techniques for Microwave and Millimeter-Wave Passive Structures*. New York, NY: Wiley, 1989.
- [26] Z-H. Zhu, W. Hong, Y. Chen, Y. Wang, and J. Tao, "Electromagnetic modeling and transient simulation of interconnects in high speed VLSI," *IEEE Multi-Chip Module Conf.*, pp. 93-98, 1995.
- [27] C. H. Chan and R. Mittra, "Analysis of MMIC structures using an efficient iterative approach," *IEEE Trans. Microwave Theory Tech.*, vol. 36, pp. 96-105, January 1988.
- [28] Y. L. Chow, J. J. Yang, and G. E. Howard, "Complex images for electrostatic field computation in multilayered media," *IEEE Trans. Microwave Theory Tech.*, vol. 40, pp. 1120-1125, July 1991.
- [29] R. F. Harrington, *Field Computation by Moment Methods*. Malabar, FL: Krieger, 1968.
- [30] J. J. H. Wang, *Generalized Moment Methods in Electromagnetics: Formulation and Computer Solution of Integral Equations*. New York, NY: Wiley, 1991.
- [31] R. F. Harrington and C. Wei, "Losses on multiconductor transmission lines in multilayered dielectric media," *IEEE Trans. Microwave Theory Tech.*, vol. 32, pp. 705-710, July 1984.
- [32] J. Carrier, L. Greengard, and V. Rokhlin, "A fast adaptive multipole algorithm for particle simulations," *SIAM J. Sci. Stat. Comp.*, vol. 9, pp. 669-686, July 1988.
- [33] K. Nabors and J. White, "FastCap : a multipole accelerated 3-D capacitance extraction program," *IEEE Trans. Computer-Aided Design*, vol. 10, pp. 1447-1459, November 1991.
- [34] C. R. Anderson, "An implementation of the fast multipole method without multipoles," *SIAM J. Sci. Stat. Comp.*, vol. 13, pp. 923-947, July 1992.
- [35] K. Nabors and J. White, "Multipole-accelerated capacitance extraction algorithms for 3-D structures with multiple dielectrics," *IEEE Trans. Circuits Syst.-I*, vol. 39, pp. 946-954, November 1992.

- [36] V. Jandhyala, E. Michielssen, and R. Mittra, "Multipole-accelerated capacitance computation for 3-D structures in a stratified dielectric medium," *Int. J. Microwave and Millimeter-Wave Computer-Aided Engg.*, submitted for publication.

CHAPTER 2

DERIVATION OF THE CLOSED-FORM GREEN'S FUNCTION FOR A MULTILAYERED DIELECTRIC MEDIUM

2.1 Introduction

Among the various electrostatic solution techniques mentioned in Section 1.3, an integral equation approach requires the most analytical effort, mainly due to the determination of the expression of the Green's function for a multilayered dielectric medium. Fortunately, the spectral-domain expression of the Green's function has already been found by several authors: the expression for full-wave analysis can be found in texts [1], [2], whereas the expression for an electrostatic problem can be found in several journal papers [3]-[6].

The conventional approach to obtain the expression of the Green's function is the use of the Fourier transformation, in which the equation governing the physics of problems, the Helmholtz wave equation for full-wave analysis and the Laplace equation for electrostatic analysis, is converted to the spectral domain by transforming all but one of space variables. Then, the resulting equation, which is an ordinary differential equation in terms of the remaining one space variable, is analytically solved to obtain the expression of the Green's function in the spectral domain. The major bottleneck of this approach is that the direct analytical inversion of this spectral-domain Green's function to the space domain is often impossible.

A simple but brute force approach for this inversion is the use of numerical integration [6], [7]. Although this approach is commonly used in full-wave analysis because of the complexity of the expression of the spectral-domain Green's function [7], it is seldom used in static analysis since this approach is computationally intensive and does not allow an analytical expression for the Green's function in the space domain.¹ Yet another simple approach is to expand the spectral-domain expression using the geometric series. Then, an analytical expression in the space domain is found by applying the inverse Fourier transformation formulas to the resulting series: the Sommerfeld identity (for 2-D

¹The comparison of the CPU time used in this approach and other alternative approaches is given in Section 3.2.2.

problems) and the Weyl identity (for 3-D problems) for full-wave analysis [Chapter 2, 2] and the equivalent identities ((2.16a) and (2.16b)) for static analysis. The resulting expression in the space domain can be shown to be identical to one obtained by applying the image theory directly in the space domain [8]. The major disadvantage of this approach or equivalently the approach based on the image theory is that the resulting expression involves the summation of a nested infinite series; for N layers, the expression would consist of a nested $N-1$ infinite series as mentioned in Chapter 1.

In this chapter, the closed-form expression of the Green's function in the space domain, which does not involve any numerical integration or nested infinite summations, is presented. The expression of the spectral-domain Green's function is first derived in the following section. This expression is different than the ones given in [3]-[6], and, as will be shown in Section 2.3, this form of the expression is more convenient for the purpose of obtaining the closed-form Green's function. Then, the spectral-domain Green's function is approximated with real-valued exponential functions, and the resulting approximate Green's function is analytically inverted to the space domain to obtain the closed-form Green's function.

2.2 Derivation of the Spectral-Domain Green's function

The cross-sectional view of the general geometry of a multilayered medium is shown in Fig. 2.1. An arbitrary number N_d of nonmagnetic lossless dielectric layers are backed by two optional ground planes with possible top or bottom locations. All dielectric layers and ground planes are assumed to be infinite and uniform in the xz plane.

Consider a unit point charge located at the m th layer at (x_o, y_o, z_o) (Fig. 2.2). The three-dimensional Green's function G^{3D} is the potential due to this point charge and satisfies the following Poisson's equation:

$$\nabla^2 G^{3D}(x, y, z|x_o, y_o, z_o) = \frac{1}{\epsilon(y)} \delta(x - x_o) \delta(y - y_o) \delta(z - z_o) \quad (2.1)$$

To assure the unique solution to the above equation, G^{3D} has to satisfy the appropriate conditions at the boundary: G^{3D} is constant at the surface of the ground planes, and G^{3D} and the normal components of the displacement field must be continuous across the dielectric interfaces. Noting that the dielectric medium is uniform in two directions, we can

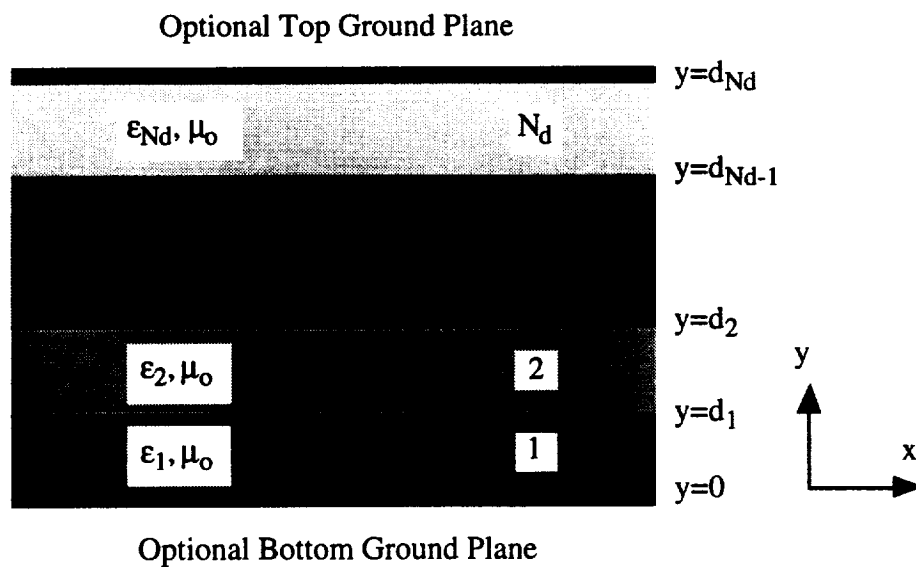


Figure 2.1. The cross-sectional view of a multilayered dielectric medium.

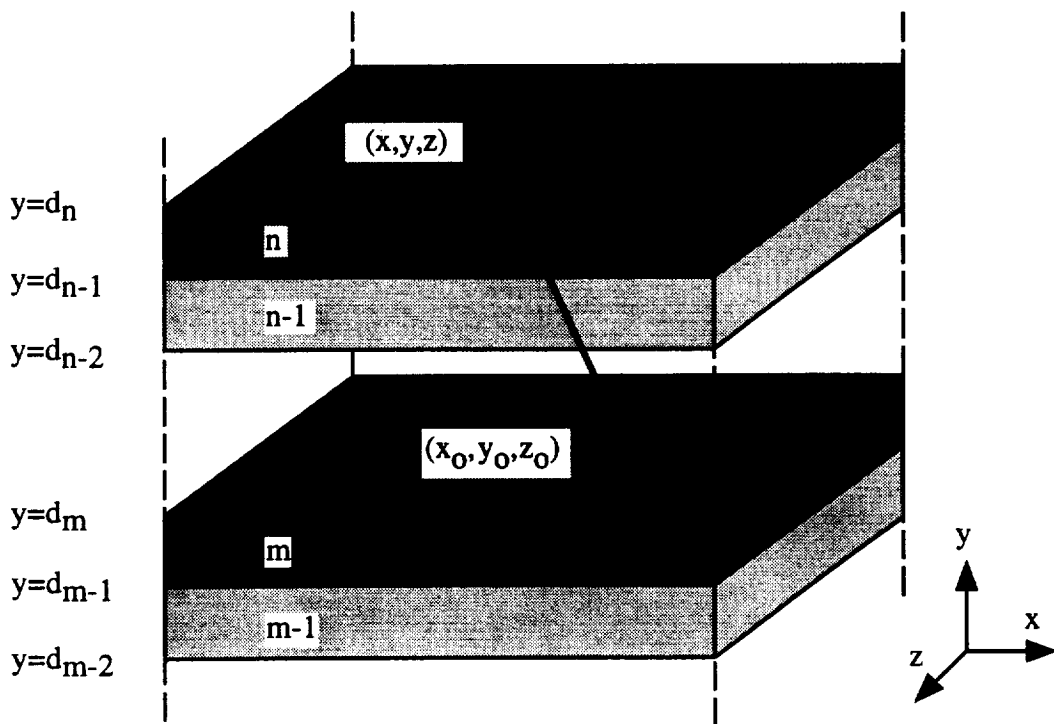


Figure 2.2. The geometric configuration used to determine the spectral-domain expression of the Green's function.

represent the Green's function and the point charge in the spectral domain in terms of their transforms in the x - and z -directions. The space-domain and the spectral-domain Green's functions are then related by

$$G^{3D}(x, y, z|x_o, y_o, z_o) = \frac{1}{(2\pi)^2} \int_{-\infty}^{+\infty} \int_{-\infty}^{+\infty} d\alpha d\beta e^{-j\alpha(x-x_o)-j\beta(z-z_o)} \tilde{G}^{3D}(\alpha, y, \beta|x_o, y_o, z_o) \quad (2.2a)$$

$$\tilde{G}^{3D}(\alpha, y, \beta|x_o, y_o, z_o) = \int_{-\infty}^{+\infty} \int_{-\infty}^{+\infty} dx dz e^{j\alpha(x-x_o)+j\beta(z-z_o)} G^{3D}(x, y, z|x_o, y_o, z_o) \quad (2.2b)$$

where $\tilde{G}^{3D}(\alpha, y, \beta|x_o, y_o, z_o)$ is the 3-D spectral-domain Green's function and α and β are the transform variables associated with the x - and z -directions, respectively. Then, the corresponding equation for (2.1) in the spectral domain is written as

$$\left(\frac{\partial^2}{\partial y^2} - \alpha^2 - \beta^2 \right) \tilde{G}^{3D}(\alpha, y, \beta|x_o, y_o, z_o) = \frac{1}{\epsilon(y)} \delta(y - y_o) \quad (2.3)$$

The general solution of the above equation is given by

$$\tilde{G}^{3D}(\gamma, y|r_o) = \frac{Ae^{-\gamma y} + Be^{\gamma y}}{2\epsilon_m \gamma}, \quad \gamma = \sqrt{\alpha^2 + \beta^2} \quad (2.4)$$

where the first subscript m denotes the layer where the source is located, whereas the second subscript n will be used to denote the layer where the Green's function is evaluated. A and B are unknown expressions to be determined. Note that ϵ_m appears in (2.4) unlike (2.3), where ϵ_n appears.

An identical expression can be obtained for the 2-D spectral-domain Green's function $\tilde{G}^{2D}(\gamma, y|\rho_o)$ by Fourier transforming $G^{2D}(x, y|x_o, y_o)$ in the x -direction with the transform variable γ assuming the layers are uniform in the x -direction. Furthermore, since the unknown coefficients A and B are to be determined using the boundary conditions only in the y -direction, it is easily seen that the expressions for \tilde{G}^{2D} and \tilde{G}^{3D} must be identical under these Fourier transformations. Thus, in what follows, the superscripts for the spectral-domain Green's functions are omitted.

Applying the boundary conditions at the dielectric interfaces and ground planes, (2.4) can be written as

$$\tilde{G}(\gamma, y|r_0) = \frac{A_{m,n}^+}{2\varepsilon_m\gamma} \left(e^{-\gamma y} + \tilde{\Gamma}_{n,n+1} e^{-\gamma(2d_n-y)} \right) \quad y \geq y_0 \quad (2.5a)$$

$$\tilde{G}(\gamma, y|r_0) = \frac{A_{m,n}^-}{2\varepsilon_m\gamma} \left(e^{+\gamma y} + \tilde{\Gamma}_{n,n-1} e^{+\gamma(2d_{n-1}-y)} \right) \quad y \leq y_0 \quad (2.5b)$$

where

$$A_{m,n}^+ = A_{m,m}^+ \prod_{j=m}^{n-1} S_{j,j+1}^+ \quad A_{m,n}^- = A_{m,m}^- \prod_{j=n+1}^m S_{j,j-1}^- \quad (2.6)$$

$$S_{j,j+1}^+ = \frac{T_{j,j+1}}{1 + \Gamma_{j,j+1} \tilde{\Gamma}_{j+1,j+2} e^{2\gamma(d_j-d_{j+1})}} \quad (2.7a)$$

$$S_{j,j-1}^- = \frac{T_{j,j-1}}{1 + \Gamma_{j,j-1} \tilde{\Gamma}_{j-1,j-2} e^{2\gamma(d_{j-1}-d_j)}} \quad (2.7b)$$

$$\tilde{\Gamma}_{j,j+1} = \frac{\Gamma_{j,j+1} + \tilde{\Gamma}_{j+1,j+2} e^{2\gamma(d_j-d_{j+1})}}{1 + \Gamma_{j,j+1} \tilde{\Gamma}_{j+1,j+2} e^{2\gamma(d_j-d_{j+1})}} \quad (2.8b)$$

$$\tilde{\Gamma}_{j,j-1} = \frac{\Gamma_{j,j-1} + \tilde{\Gamma}_{j-1,j-2} e^{2\gamma(d_{j-2}-d_{j-1})}}{1 + \Gamma_{j,j-1} \tilde{\Gamma}_{j-1,j-2} e^{2\gamma(d_{j-2}-d_{j-1})}} \quad (2.8b)$$

$$\Gamma_{i,j} = \frac{\varepsilon_i - \varepsilon_j}{\varepsilon_i + \varepsilon_j} \quad T_{i,j} = \frac{2\varepsilon_i}{\varepsilon_i + \varepsilon_j} \quad (2.9)$$

Here, $\Gamma_{i,j}$ and $T_{i,j}$ are the reflection and transmission coefficients. $\Gamma_{j,j+1}$ takes the value of 0 or -1 if the j th layer is a half space, or the $(j+1)$ th layer is a ground plane, respectively. $\tilde{\Gamma}_{n,n+1}$ is the generalized reflection coefficient, which is the ratio of the amplitudes of the potentials at $y = d_n$ due to the image charges located above and below $y = d_n$. $A_{m,m}^+$ and $A_{m,m}^-$ are unknown expressions to be determined. The superscripts + and - are used to denote the cases for $y \geq y_0$ and $y \leq y_0$, respectively.

Using the facts, at $y = y_o$, that (2.5a) and (2.5b) must be equal and that the normal component of the displacement field must be discontinuous by the magnitude of the charge, we can obtain expressions for $A_{m,m}^+$ and $A_{m,m}^-$ as follows:

$$A_{m,m}^+ = M_m \left[e^{+\gamma y_o} + \tilde{\Gamma}_{m,m-1} e^{+\gamma(2d_{m-1}-y_o)} \right] \quad (2.10a)$$

$$A_{m,m}^- = M_m \left[e^{-\gamma y_o} + \tilde{\Gamma}_{m,m+1} e^{-\gamma(2d_m-y_o)} \right] \quad (2.10b)$$

where

$$M_m = \left[1 - \tilde{\Gamma}_{m,m-1} \tilde{\Gamma}_{m,m+1} e^{2\gamma(d_{m-1}-d_m)} \right]^{-1} \quad (2.11)$$

The complete expression of the spectral-domain Green's function has now been derived. In (2.5a), $A_{m,n}^+$ can be physically interpreted as image charges (and the actual charge when m is equal to n) located below the observation point y , whereas the product of $A_{m,n}^+$ and $\tilde{\Gamma}_{n,n+1}$ can be interpreted as image charges located above the observation point. A similar interpretation can be given to (2.5b).

It is interesting to note that all of the above equations have the following form:

$$f_k(\gamma) = \frac{c_1}{1 - c_2 f_{k-1}(\gamma) e^{\gamma c_3}} \quad (2.12)$$

where c_1 , c_2 , and c_3 are some constants which satisfy $0 \leq c_2 f_{k-1}(\gamma) e^{\gamma c_3} \leq 1$, and the expression of $f_{k-1}(\gamma)$ is in the same form as $f_k(\gamma)$ for $k > 1$ and is a constant function for $k = 1$. The value of k depends on the number of dielectric layers; for instance, for N dielectric layers k takes values from 1 to N . Since $0 \leq c_2 f_{k-1}(\gamma) e^{\gamma c_3} \leq 1$ for all k , the geometric series can be used to expand $f_k(\gamma)$, and the resulting series is a nested $N-1$ infinite series. The entire expression of the spectral-domain Green's function can then be written in terms of this series, and each term of the series can be conveniently inverted to the space domain using the integration formulas (2.16a) and (2.16b) to be given in the following section. It can further be shown that the resulting expression of the Green's function in the space domain is identical to the one obtained by using the image theory. Hence, the exact expression of the Green's function in the space domain generally consists of a nested infinite series.

In the following section, the closed-form spatial Green s function, which avoids this nested infinite series, is derived based on the expression of the spectral-domain Green s function obtained in this section.

2.3 Derivation of the Space-Domain Green s function

In this section, the closed-form expression of the Green s function in the space domain is obtained by applying the exponential approximation to the spectral-domain Green s function. To obtain the closed-form expression of the Green s function in the space domain, the spectral-domain expression of the Green s function derived in the previous section is first rearranged by factoring out all y and y_o dependencies as follows:

$$\begin{aligned} \tilde{G}(\gamma, y|r_o) = & \frac{1}{2\varepsilon_m\gamma} \left(K_1^+(\gamma, m, n)e^{\gamma(y+y_o-2d_n)} + K_2^+(\gamma, m, n)e^{\gamma(y-y_o+2(d_{m-1}-d_n))} \right. \\ & \left. + K_3^+(\gamma, m, n)e^{\gamma(-y+y_o)} + K_4^+(\gamma, m, n)e^{\gamma(-y-y_o+2d_{m-1})} \right) \quad y \geq y_o \quad (2.13a) \end{aligned}$$

$$\begin{aligned} \tilde{G}(\gamma, y|r_o) = & \frac{1}{2\varepsilon_m\gamma} \left(K_1^-(\gamma, m, n)e^{\gamma(y+y_o-2d_m)} + K_2^-(\gamma, m, n)e^{\gamma(y-y_o)} \right. \\ & \left. + K_3^-(\gamma, m, n)e^{\gamma(-y+y_o+2(d_{n-1}-d_m))} + K_{m,n,4}^-e^{\gamma(-y-y_o+2d_{n-1})} \right) \quad y \leq y_o \quad (2.13a) \end{aligned}$$

where

$$\begin{aligned} K_1^+(\gamma, m, n) &= M_m \tilde{\Gamma}_{n,n+1} \prod_{j=m}^{n-1} S_{j,j+1}^+ \\ K_2^+(\gamma, m, n) &= M_m \tilde{\Gamma}_{n,n+1} \tilde{\Gamma}_{m,m-1} \prod_{j=m}^{n-1} S_{j,j+1}^+ \\ K_3^+(\gamma, m, n) &= M_m \prod_{j=m}^{n-1} S_{j,j+1}^+ \\ K_4^+(\gamma, m, n) &= M_m \tilde{\Gamma}_{m,m-1} \prod_{j=m}^{n-1} S_{j,j+1}^+ \end{aligned} \quad (2.14a)$$

$$\begin{aligned}
K_1^-(\gamma, m, n) &= M_m \tilde{\Gamma}_{m,m+1} \prod_{j=n+1}^m S_{j,j-1}^- \\
K_2^-(\gamma, m, n) &= M_m \prod_{j=n+1}^m S_{j,j-1}^- \\
K_3^-(\gamma, m, n) &= M_m \tilde{\Gamma}_{m,m+1} \tilde{\Gamma}_{n,n-1} \prod_{j=n+1}^m S_{j,j-1}^- \\
K_4^-(\gamma, m, n) &= M_m \tilde{\Gamma}_{n,n-1} \prod_{j=n+1}^m S_{j,j-1}^- \tag{2.14b}
\end{aligned}$$

The determination of the closed-form spatial Green's function can now be preceded by approximating the above four coefficient functions $K_i^\pm(\gamma, m, n)$ using exponential functions. It is important to mention that although $K_i^\pm(\gamma, m, n)$ is dependent on m and n , it is not a function of the source and observation locations, y and y_o ; hence, the approximation can be performed without any prior knowledge of the geometry of the conductors.

One physically intuitive approach to approximate the potential due to a charge in the layered medium may be the use of a finite number of weighted image charges in the homogenous medium, which is equivalent to approximating the coefficient functions $K_i^\pm(\gamma, m, n)$ with exponential functions. These weighted images can be either complex or real depending on whether complex-valued or real-valued exponential functions are used in the approximation. The equivalence between the weighted image charges in the space domain and exponential functions in the spectral domain will be shown later in (2.18a) and (2.18b).

In electromagnetic analyses, the complex-valued exponential functions are often used for pole-zero modeling of signals, such as an electromagnetic-scatterer response. The least-square formulation of this exponential approximation results in nonlinear equations and can only be solved by iterative methods, such as gradient descent procedures or the Newton method. Due to the computational inefficiency of these algorithms, some other suboptimal noniterative techniques are proposed: the least-squares Prony method and the generalized pencil-of-function (GPOF) method [9], [10]. These suboptimal methods are

used to obtain the closed-form Green's function for full-wave analysis [11]-[13]² and further applied to obtain the closed-form Green's function for electrostatic analysis [8]. Although these algorithms are noniterative, their computation involves matrix inversions and a polynomial factoring or a solution of the generalized eigenvalue problem, which still can be considered as computationally inefficient.

Fortunately, the four coefficient functions $K_i^\pm(\gamma, m, n)$ in (2.13a) and (2.13b) are nonoscillatory and smooth functions of γ ; hence, each coefficient function can be sufficiently approximated with real-valued exponential functions instead of complex-valued exponential functions, avoiding computationally expensive complex operations. The real-valued exponential approximation method described in [14] is employed in this thesis. The method is based on the relaxation of curve fitting, and the details of the procedure are given in Appendix A. Although this method is simple and iterative in nature, it converges to reasonable accuracy in a few iterations and requires much less computation time as compared to those for the previously mentioned methods.

It can be seen that a pole exists at $\gamma = 0$ for a medium with both top and bottom ground planes, and $K_i^\pm(\gamma, m, n)$ can no longer be accurately approximated with exponential functions. Thus, a special treatment is required for this case to extract the pole from $K_i^\pm(\gamma, m, n)$. In the following subsection, the closed-form Green's function is obtained for cases with no ground planes or only the bottom ground plane, and the subsequent subsection discusses the derivation of the Green's function for a case with both top and bottom ground planes.

2.3.1 Closed-form Green's functions for geometries without any ground planes or with only the bottom ground plane

When the dielectric layers are not backed by both top and bottom ground planes, the four coefficient functions $K_i^\pm(\gamma, m, n)$ do not have any poles; furthermore, they are nonoscillatory and smooth functions of γ . Hence, they can be approximated using the exponential approximation method discussed in Appendix A as follows:

²Strictly speaking, the closed-form Green's function does not exist for a full-wave case since y and y_0 dependencies cannot be removed from the coefficient functions before the approximation.

$$K_i^\pm(m, n, \gamma) = \sum_{j=1}^{N_{m,n,i}^\pm} C_{m,n,i}^{\pm,j} e^{a_{m,n,i}^{\pm,j} \gamma} \quad (2.15)$$

where $N_{m,n,i}^\pm$ denotes the number of exponential functions used in the approximation of $K_i^\pm(\gamma, m, n)$, which typically ranges from 5 to 10. In general, $K_i^\pm(\gamma, m, n)$ have asymptotic values, and an analytical extraction of these values should be performed to increase the accuracy of the approximation or to reduce the computation time. These asymptotic values can be easily obtained either analytically or numerically. Furthermore, some of these coefficient functions are often zero or one, and these properties can also be explored for further computer time savings.

Once the exponential approximation is performed in the spectral domain, the closed-form Green's functions for 2-D and 3-D can be obtained in the space domain by using the following inverse Fourier transformation formulas:

$$-\ln(\rho) = -\ln(\sqrt{x^2 + y^2}) = \frac{1}{2\pi} \int_{-\infty}^{+\infty} d\gamma e^{-j\gamma x} \frac{e^{-|\gamma y|}}{|\gamma|} \quad (2.16a)$$

$$\frac{1}{r} = \frac{1}{\sqrt{x^2 + y^2 + z^2}} = \frac{1}{2\pi} \int_{-\infty}^{+\infty} \int_{-\infty}^{+\infty} d\alpha d\beta e^{-j(\alpha x + \beta z)} \frac{e^{-\gamma|y|}}{\gamma} \quad (2.16b)$$

where $\gamma = \sqrt{\alpha^2 + \beta^2}$ in (2.16b). The above identities can be easily derived by considering the potentials due to the unit point and line charges in a homogeneous medium without any ground planes, and the corresponding identities for a full-wave case are Sommerfeld's and Weyl's identities, respectively. Applying the above formulas to (2.13a) and (2.13b), the closed-form 2-D and 3-D Green's functions are written as

$$G^{2D}(\rho|\rho_o) = -\frac{1}{2\pi\epsilon_m} \sum_{i=1}^4 f_i^{2D,\pm}(\rho|\rho_o) \quad (2.17a)$$

$$G^{3D}(r|r_o) = \frac{1}{4\pi\epsilon_m} \sum_{i=1}^4 f_i^{3D,\pm}(r|r_o) \quad (2.17b)$$

For $i = 1$ and $y \geq y_o$, the expressions of $f_i^{2D,\pm}(r|r_o)$ and $f_i^{3D,\pm}(r|r_o)$ are given by

$$f_1^{2D,+}(\rho|\rho_o) = \sum_{j=1}^{N_{m,n,1}^+} C_{m,n,1}^{+,j} \cdot \ln\left(\sqrt{(x-x_o)^2 + (y+y_o - 2d_n + a_{m,n,1}^{+,j})^2}\right) \quad (2.18a)$$

$$f_1^{3D,+}(r|r_o) = \sum_{j=1}^{N_{m,n,1}^+} \frac{C_{m,n,1}^{+,j}}{\sqrt{(x-x_o)^2 + (y+y_o - 2d_n + a_{m,n,1}^{+,j})^2 + (z-z_o)^2}} \quad (2.18b)$$

Similar expressions can be obtained for $f_i^{2D,\pm}(r|r_o)$ and $f_i^{3D,\pm}(r|r_o)$ for other values of i .

The derivations of the closed-form Green s functions for a point charge and a line charge are now completed for geometries without both top and bottom ground planes. Considering the forms of (2.18a) and (2.18b) it is clear that the exponential functions used to approximate the Green s function in the spectral domain correspond to the weighted images in the space domain.

In the computation of the equivalent capacitances of interconnection discontinuities, the Green s function for a uniform semi-infinite line charge, $G^{semi}(r|r_o, \xi)$, is required to formulate the integral equation in terms of the excess charge distribution. The closed-form Green s function for a semi-infinite line charge is derived in the rest of this subsection.

To derive $G^{semi}(r|r_o, \xi)$, the auxiliary Green s function for a line charge with polarity reversal is employed [15]. Consider a uniform line charge, which starts from $z = \xi$ and is infinitely extended in the positive z -direction (see Fig. 2.3); then $G^{semi}(r|r_o, \xi)$ can be expressed as

$$G^{semi}(r|r_o, \xi) = \frac{1}{2} \left[G^{2D}(\rho|\rho_o) + G^P(r|r_o, \xi) \right] \quad (2.19)$$

where $G^P(r|r_o, \xi)$ is the Green s function for a line charge with an abrupt polarity reversed from minus to plus at $z = \xi$. Since the closed-form expression of $G^{2D}(\rho|\rho_o)$ can be obtained using the previous technique, the closed-form expression of $G^{semi}(r|r_o, \xi)$ can be determined once the closed-form expression is derived for $G^P(r|r_o, \xi)$. The expression for $G^P(r|r_o, \xi)$ is rather easily obtained by integrating the potential due to a point charge:

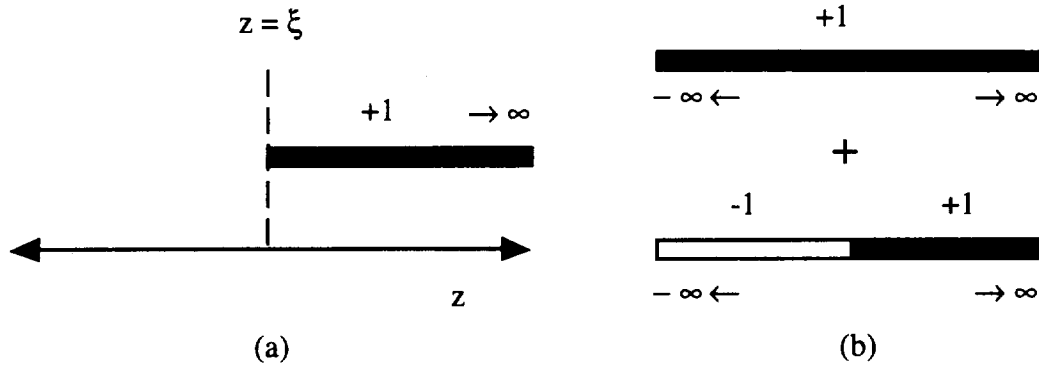


Figure 2.3. The decomposition of (a) the uniform semi-infinite line charge to (b) an infinite uniform line charge and an infinite line charge with the polarity reversal at $z = \xi$.

$$G^P(r|r_o, \xi) = - \int_{-\infty}^{\xi} G^{3D}(r|r_o) + \int_{\xi}^{\infty} G^{3D}(r|r_o) = \frac{1}{4\pi\epsilon_m} \sum_{i=1}^4 f_i^{P,\pm}(r|r_o, \xi) \quad (2.20)$$

The integration can be performed using the following formula [(3.3.40), 16]:

$$\int \frac{dx}{\sqrt{x^2 \pm a^2}} = \ln \left| x + \sqrt{x^2 \pm a^2} \right| \quad (2.21)$$

Again, for $i = 1$ and $y \geq y_o$, $f_i^{P,\pm}(r|r_o, \xi)$ is given by

$$f_1^{P,+}(r|r_o, \xi) = \sum_{j=1}^{N_{m,n,1}^+} C_{m,n,1}^{+,j} \cdot \ln \left(\frac{\sqrt{(x-x_o)^2 + (y+y_o - 2d_n + a_{m,n,1}^{+,j})^2 + (z-\xi)^2} + (z-\xi)}{\sqrt{(x-x_o)^2 + (y+y_o - 2d_n + a_{m,n,1}^{+,j})^2 + (z-\xi)^2} - (z-\xi)} \right) \quad (2.22)$$

2.3.2 Closed-form Green's functions for geometries with both top and bottom ground planes

As mentioned earlier, when both top and bottom ground planes are present, all of the four coefficient functions $K_i^{\pm}(\gamma, m, n)$ are still nonoscillatory but contain a pole at $\gamma = 0$. Since exponential functions are bounded, they cannot be used to approximate unbounded functions; therefore, this singularity must be extracted prior to the exponential approximation to preserve good approximation results. In [11], the complex exponential approximation has been performed without considering this singularity and used to obtain the closed-form Green's function. As a consequence, the resulting capacitance values from this

Green's function were shown to contain large errors. The extraction of this pole can be accomplished by rewriting $\tilde{G}(\gamma, y|r_o)$ in the following manner:

$$\tilde{G}(\gamma, y|r_o) = R_{m,n} \tilde{G}^h(\gamma, y|r_o) + \tilde{G}'(\gamma, y|r_o) \quad (2.23)$$

where $\tilde{G}^h(\gamma, y|r_o)$ is the spectral-domain Green's function for a homogeneous medium with the same ground planes, i.e., all dielectric layers are replaced by the source layer. Again, $\tilde{G}^h(\gamma, y|r_o)$ contains a pole at $\gamma = 0$. $R_{m,n}$ is a constant which is determined such that $\tilde{G}'(\gamma, y|r_o)$ is a well-behaved function without any poles. $R_{m,n}$ can be obtained either numerically or analytically by taking limits of $\tilde{G}(\gamma, y|r_o)$ and $\tilde{G}^h(\gamma, y|r_o)$ as $\gamma \rightarrow 0$.

Now the technique used in the previous section can be applied to obtain the closed-form expression for $\tilde{G}'(\gamma, y|r_o)$ in the space domain, and the expressions of $\tilde{G}(\gamma, y|r_o)$ are obtained once the space-domain expressions of $\tilde{G}^h(\gamma, y|r_o)$ are determined. Since the medium is homogeneous for $\tilde{G}^h(\gamma, y|r_o)$, the expressions can be easily obtained using the image theory and are given by

$$G^{2D,h}(\rho|\rho_o) = -\frac{1}{2\pi} \sum_{k=-\infty}^{\infty} \ln \left(\frac{\sqrt{(x-x_o)^2 + (y-y_o-2kh)^2}}{\sqrt{(x-x_o)^2 + (y+y_o-2kh)^2}} \right) \quad (2.24a)$$

$$G^{3D,h}(r|r_o) = \frac{1}{4\pi} \sum_{k=-\infty}^{\infty} \left(\frac{1}{\sqrt{(x-x_o)^2 + (y-y_o-2kh)^2 + (z-z_o)^2}} - \frac{1}{\sqrt{(x-x_o)^2 + (y+y_o-2kh)^2 + (z-z_o)^2}} \right) \quad (2.24b)$$

$$G^{p,h}(r|r_o, \xi) = \frac{1}{4\pi} \sum_{k=-\infty}^{\infty} \ln \left(\frac{\sqrt{(x-x_o)^2 + (y-y_o-2kh)^2 + (z-\xi)^2} + (z-\xi)}{\sqrt{(x-x_o)^2 + (y-y_o-2kh)^2 + (z-\xi)^2} - (z-\xi)} \cdot \frac{\sqrt{(x-x_o)^2 + (y+y_o-2kh)^2 + (z-\xi)^2} - (z-\xi)}{\sqrt{(x-x_o)^2 + (y+y_o-2kh)^2 + (z-\xi)^2} + (z-\xi)} \right) \quad (2.24c)$$

Unfortunately, all expressions are written in terms of infinite series. $G^{2D,h}(\rho|\rho_o)$ can be alternatively expressed using a closed-form formula [17], but this closed-form expression requires numerical integration when the moment matrix is computed, unlike (2.24a), which

can be integrated analytically (see Section 2.4). The detailed discussion of alternative expressions for $G^{2D,h}(\rho|\rho_o)$ is given in Appendix B. For the remaining Green's functions, $G^{3D,h}(r|r_o)$ and $G^{P,h}(r|r_o,\xi)$, such a closed-form formula does not exist at least without special functions and an infinite-series expression cannot be avoided when both top and bottom ground planes are present. However, the expressions for $G^{2D}(\rho|\rho_o)$, $G^{3D}(r|r_o)$, and $G^P(r|r_o,\xi)$ given in this subsection are still numerically more efficient than the ones obtained from the conventional image method since a nested infinite series ($N-1$ nested infinite series for N layers) of the conventional method is reduced to a simple infinite series without any nesting as shown in the above equations. For this reason we shall still refer to the Green's functions expressed by (2.23), (2.24a), (2.24b) and (2.24c) as closed-form Green's functions.

2.4 Closed-form Integration Formulas for the Elements of Moment Matrices

When integral equations are solved using the method of moments (MoM), the elements of the moment matrix are computed by integrating the Green's function over basis and testing functions; the closed-form formula for this integration is discussed in this section. The general forms of the integrations required to construct the moment matrix are

$$\int_{l_t} \int_{l_s} T(\rho) G^{2D}(\rho|\rho_s) B(\rho_s) d\rho_s d\rho \quad (2.25a)$$

$$\int_{\Omega_t} \int_{\Omega_s} T(r) G^{3D}(r|r_s) B(r_s) dr_s dr \quad (2.25b)$$

where T and B are testing and basis functions, l_s is the source line segment, and l_t is the testing line segment where the potential is evaluated for 2-D problems. Similarly, Ω_s and Ω_t are the source and testing patches for 3-D problems. The method of collocation uses the delta testing function (point matching) to reduce the above double integrations to a single integration; it is used in this thesis whenever the moment method is employed. The testing point is usually chosen at the center of a segment or a patch.

For basis functions used to expand the surface charge density, pulse-type functions, which are commonly used in the method of collocation, are used in this thesis. Then, (2.25a) and (2.25b) simplify to

$$\int_{l_s} G^{2D}(\rho_c|\rho_s) d\rho_s \quad (2.26a)$$

$$\int_{\Omega_s} G^{3D}(r_c|r_s) dr_s \quad (2.26b)$$

where ρ_c and r_c are the centers of the testing segment and patch. Similarly, the integral associated with $G^{semi}(r_c|r_s, \xi)$ can be written as

$$\int_{l_s} G^{semi}(r_c|r_s, \xi) d\rho_s \quad (2.26c)$$

Equation (2.26a) appears in the computation of the moment matrix for 2-D problems or the right-hand side vector (excitation vector) computation for the equivalent capacitance of a crossover. Equation (2.26b) only appears in the computation of the moment matrix for 3-D problems, whereas (2.26c) only appears in the computation of the right-hand side vector for the equivalent capacitances for various junction discontinuities.

After substituting (2.17a) and (2.18a) into (2.26a), the line integrals associated with each term in the summation can be put into the following form with manipulations in y , y_o , and the terms due to the exponential approximation:

$$\int_c \ln\left(\sqrt{(x-x')^2 + (y-y')^2}\right) dl' = \int_c \ln(|\rho - \rho'|) dl' = \int_c \ln(P) dl' \quad (2.27a)$$

Similarly, for 3-D problems we have

$$\iint_s \frac{ds'}{\sqrt{(x-x')^2 + (y-y')^2 + (z-z')^2}} = \iint_s \frac{ds'}{|\mathbf{r} - \mathbf{r}'|} = \iint_s \frac{ds'}{R} \quad (2.27b)$$

The evaluations of (2.19a) and (2.19b) over an arbitrary polygonal patch and a line segment are well-known and the closed-form formulas are given in [18]. On the other hand, (2.26c) can also be integrated analytically using the following integration formula [19]:

$$\begin{aligned}
\int_{l_1}^{l_2} \ln \left[\frac{\sqrt{a^2 + b^2 + l^2} + a}{\sqrt{a^2 + b^2 + l^2} - a} \right] dl &= 2|b| \left[\tan^{-1} \left(\frac{al_1}{|b|\sqrt{a^2 + b^2 + l_1^2}} \right) \right. \\
&- \tan^{-1} \left(\frac{al_2}{|b|\sqrt{a^2 + b^2 + l_2^2}} \right) \left. \right] + 2a \ln \left(\frac{l_2 + \sqrt{a^2 + b^2 + l_2^2}}{l_1 + \sqrt{a^2 + b^2 + l_1^2}} \right) \\
&+ l_2 \ln \left(\frac{\sqrt{a^2 + b^2 + l_2^2} + a}{\sqrt{a^2 + b^2 + l_2^2} - a} \right) - l_1 \ln \left(\frac{\sqrt{a^2 + b^2 + l_1^2} + a}{\sqrt{a^2 + b^2 + l_1^2} - a} \right) \quad (2.27c)
\end{aligned}$$

Finally, using the above integration formulas all elements of the moment matrices and the right-hand side vectors encountered in this thesis can be performed analytically.

2.5 The Comparison of the Exact and Approximate Green s Functions

In this section, the comparison of the closed-form Green s function, which is approximate, and the exact Green s function is presented. As a first example, the medium shown in Fig. 2.4 is considered. The maximum number of 11 exponential functions are

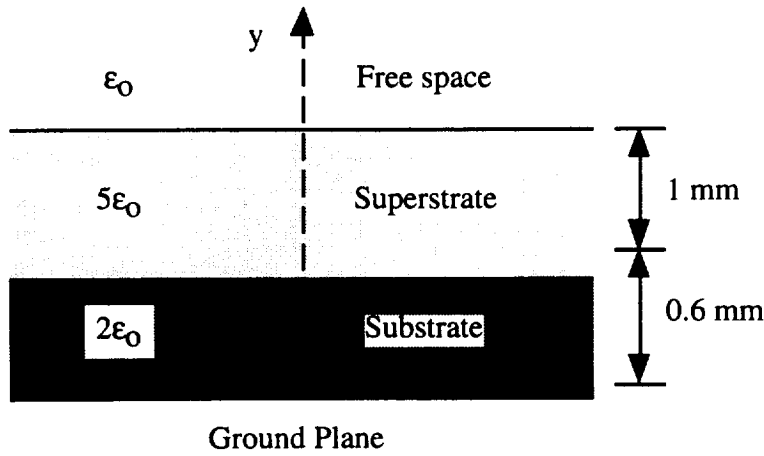


Figure 2.4. The first geometry used to test the closed-form Green s function.

used in the approximation. The observation and source points, y and y_o , were taken to be 0.6 mm and 1.6 mm, respectively. Figure 2.5(a) shows the comparison of the approximate and the exact Green s functions, and Fig. 2.5(b) shows the relative errors; the maximum relative error was less than 0.023 %. It is important to observe that although the exponential approximation might fail for the large argument case due to its fast decaying nature, by extracting the asymptotic values and the y and y_o related exponential factors from the coefficient functions, the limiting behavior of the overall approximated Green's function would still remain accurate for the large values of γ .

As a second example, the two-layer medium case shown in Fig. 2.6 is considered. A maximum number of exponential functions used in the approximation was five. y and y_o were again taken to be 0.6 mm and 1.6 mm. The comparison is shown in Figs. 2.7(a) and 2.7(b), and an excellent agreement was found. The approximate closed-form Green s function is also compared with the exact Green s function in the space domain. The exact 2-D Green s function is obtained using the image method and is given by

$$G^{2D}(\rho|\rho_o) = \frac{(1+\Gamma)}{4\pi\epsilon_o} \sum_{k=1}^{\infty} \ln \left(\frac{(x-x_o)^2 + (y-y_o - (2k-1)h)^2}{(x-x_o)^2 + (y-y_o - (2k-3)h)^2} \right) \quad y \geq h \quad (2.28a)$$

$$G^{2D}(\rho|\rho_o) = \frac{(1+\Gamma)}{4\pi\epsilon_o} \sum_{k=1}^{\infty} \Gamma^{k-1} \ln \left(\frac{(x-x_o)^2 + (y+(2k-1)h)^2}{(x-x_o)^2 + (y+(2k-3)h)^2} \right) \quad y \leq h \quad (2.28b)$$

where

$$\Gamma = \frac{\epsilon_o - \epsilon_1}{\epsilon_o + \epsilon_1} \quad (2.28c)$$

In the above expressions, it is assumed that the line source is located at the dielectric interface.

The comparison results are shown in Figs. 2.8(a) and 2.8(b), and the results were in good agreement. This example justifies the validity of the approximation of the Green s function in the spectral domain. It is observed from numerous approximations that the smaller number of dielectric layers required fewer exponential functions to approximate, as expected. In fact, for one layer with a ground plane, the closed-form Green s function becomes exact since there is only one image charge.

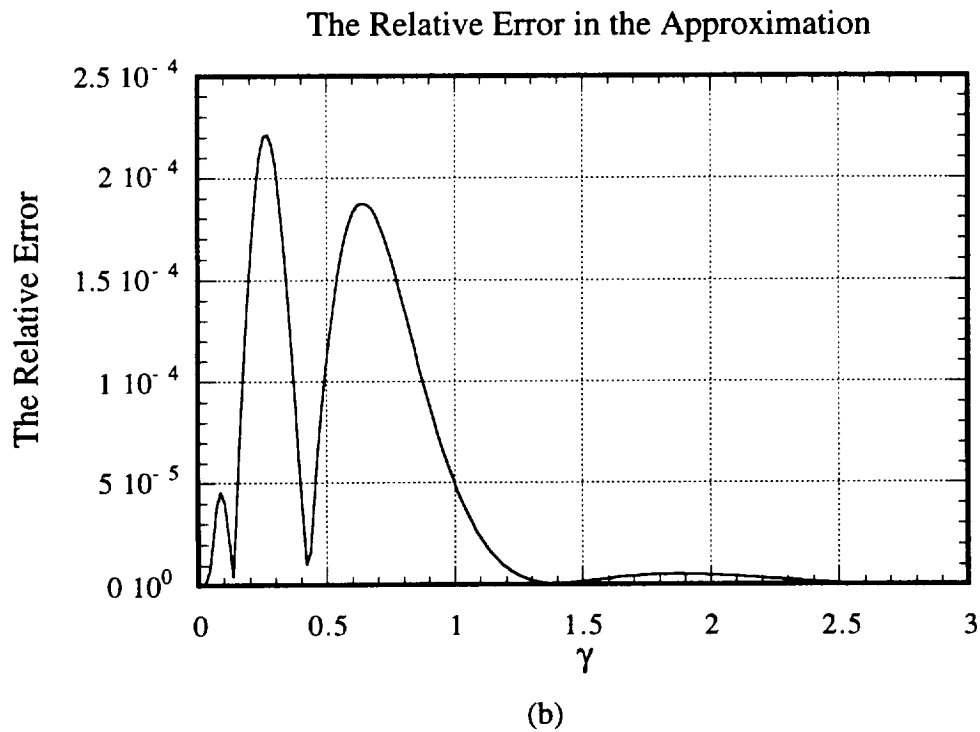
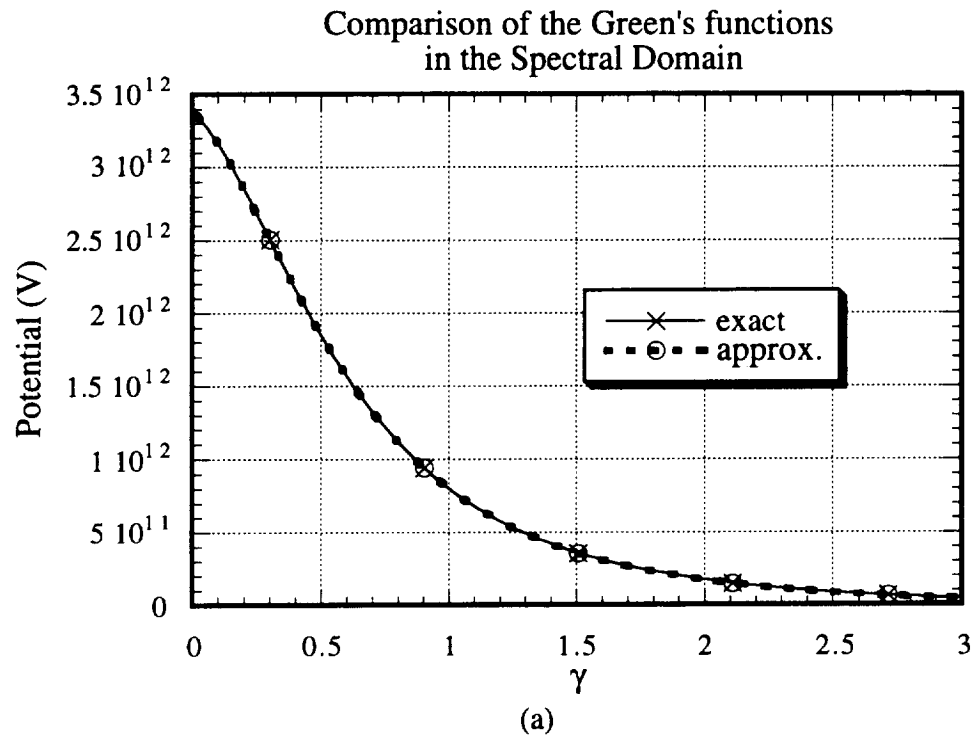


Figure 2.5. (a) Comparison of approximated and exact Green's functions in the spectral domain for the medium shown in Fig. 2.4 and (b) the plot of the relative error.

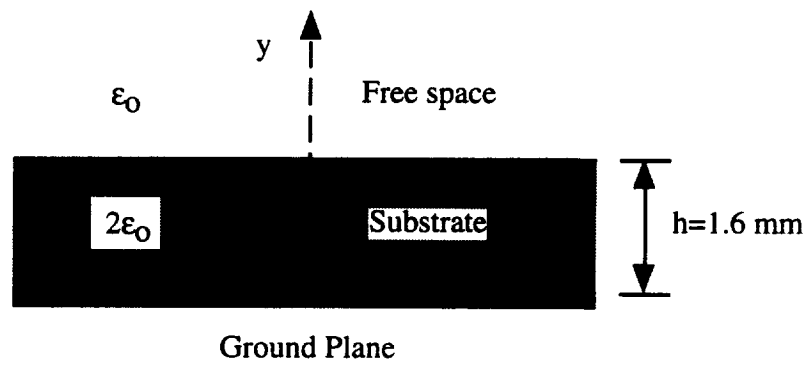


Figure 2.6. The second geometry used to test the closed-form Green's function.

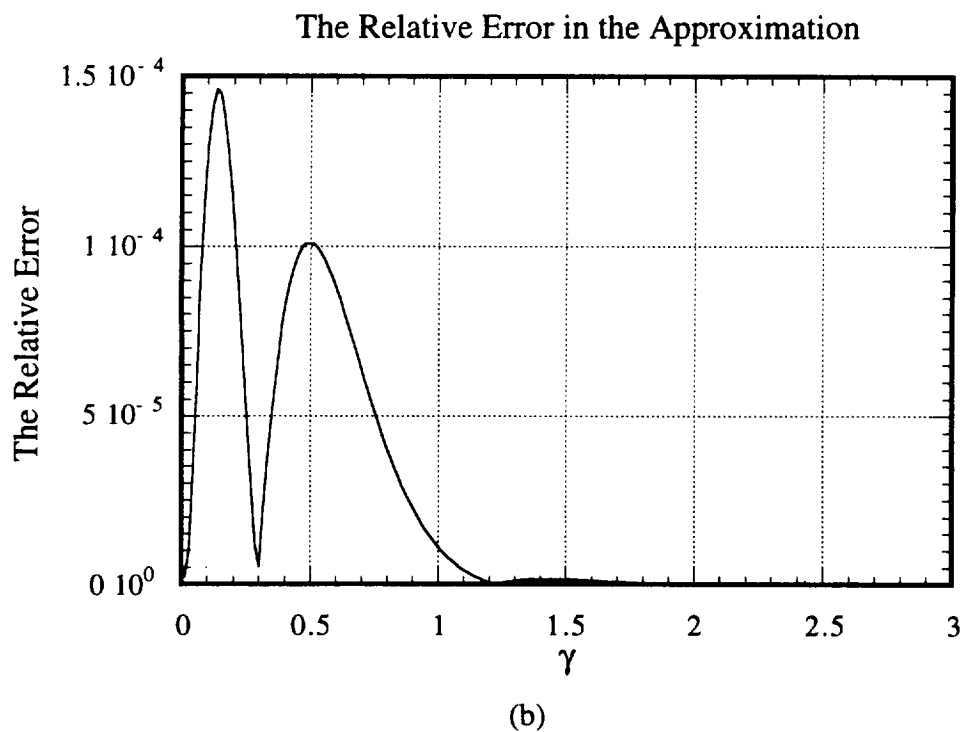
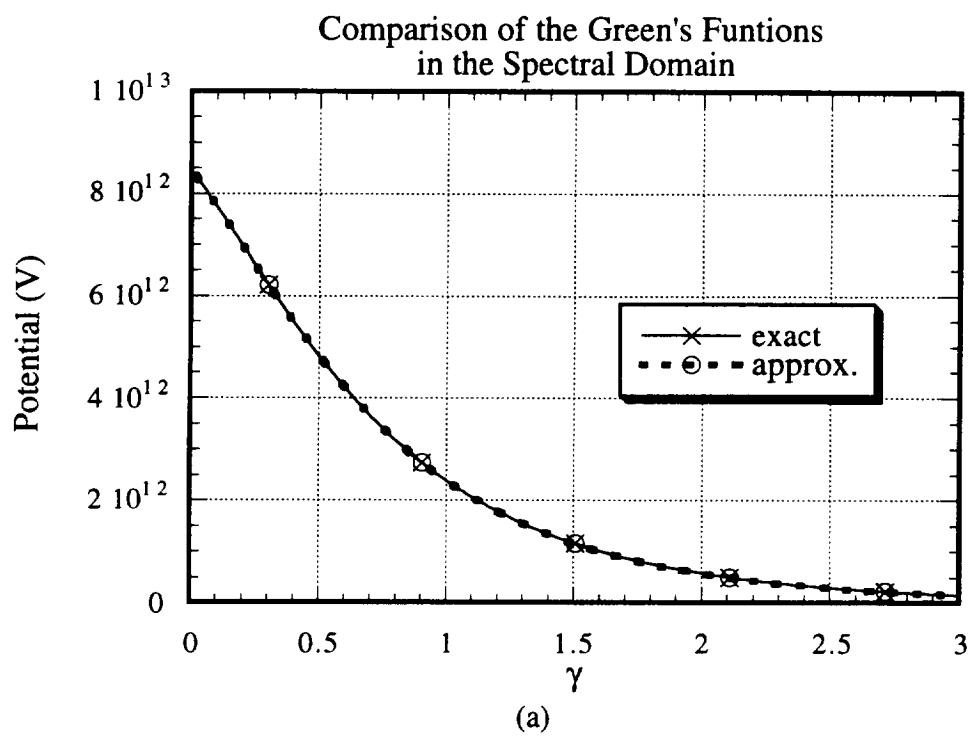


Figure 2.7. (a) Comparison of approximated and exact Green's functions in the spectral domain for the medium shown in Fig. 2.6 and (b) the plot of the relative error.

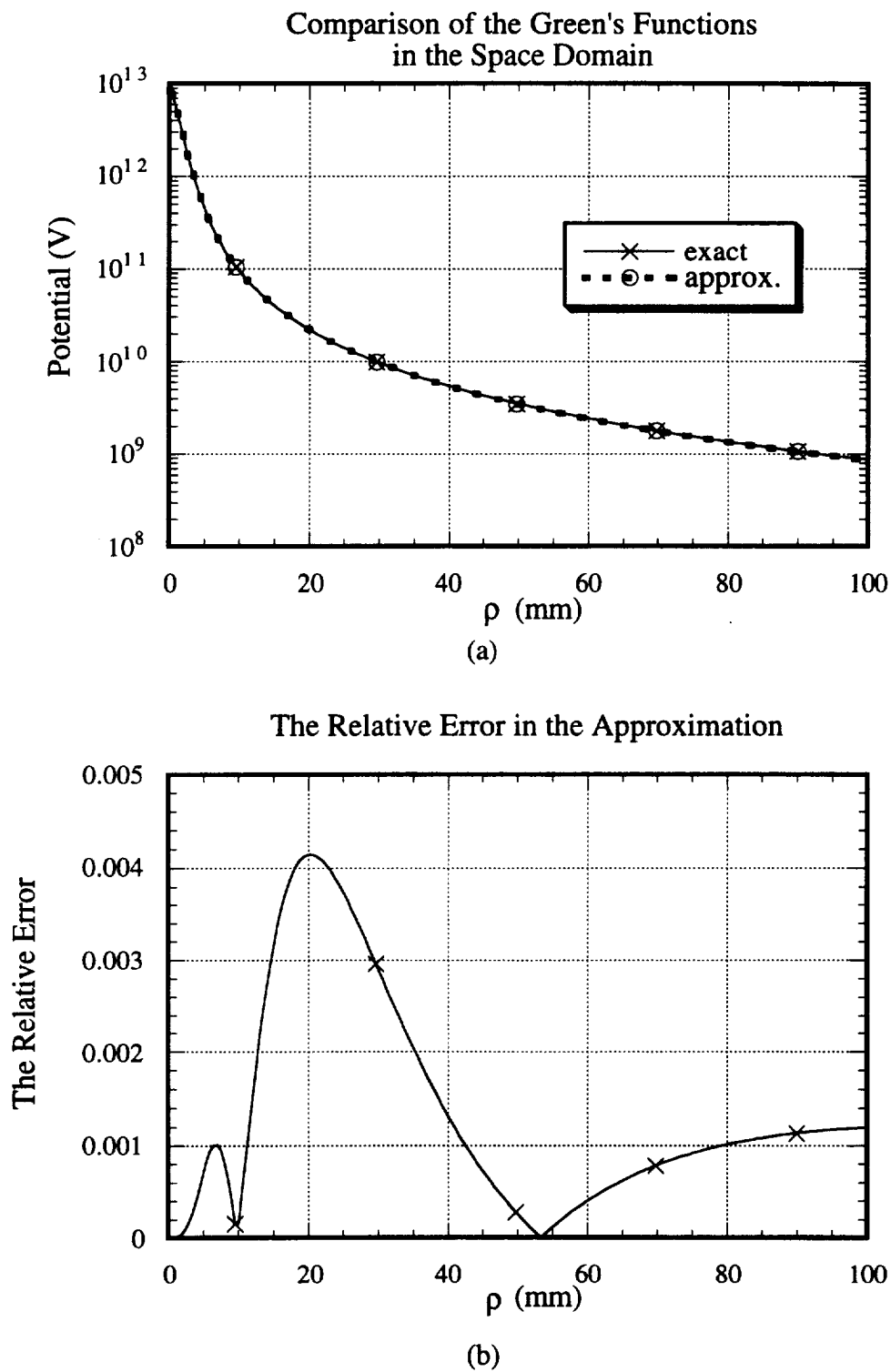


Figure 2.8. (a) Comparison of approximated and exact Green's functions in the space domain for the medium shown in Fig. 2.6 and (b) the plot of the relative error.

For the final example, the stripline case shown in Fig. 2.9 is considered. In general, a slightly larger number of exponential functions was required for a strip case, where both the top and bottom ground planes were present, and a maximum number of 13 exponential functions were used in this approximation. Both y and y_0 were taken to be 0.1 mm. To compare the approximation results, $\tilde{G}(\gamma, y|r_0)$ in (2.23) is considered instead of $\tilde{G}(\gamma, y|r_0)$. The comparison results are shown in Figs. 2.10(a) and 2.10(b), and a good agreement was found.

For most numerical examples given in this thesis, the exponential approximation took less than a second of the CPU time in Sparc 10 and Alpha workstations; thus, the CPU time used in the approximation was negligible compared to the one for the construction or the inversion of the moment matrix.

Finally, it should be mentioned that since the method of moments is an approximate way of solving an integral equation, only a moderate accuracy is required for the Green's function. In general, five exponential functions for cases with the presence of either one of the top and bottom ground planes and seven exponential functions for cases with the presence of both the top and bottom ground planes were enough to solve most capacitance problems.

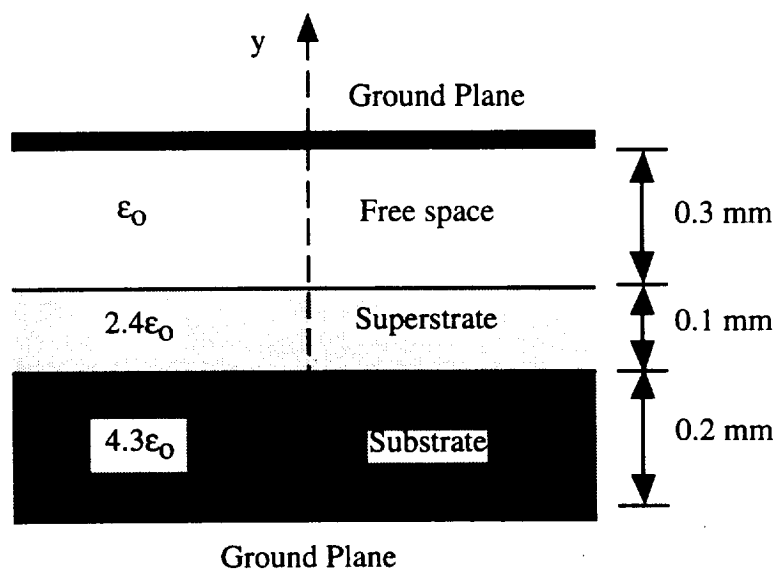


Figure 2.9. The second geometry used to test the closed-form Green's function.

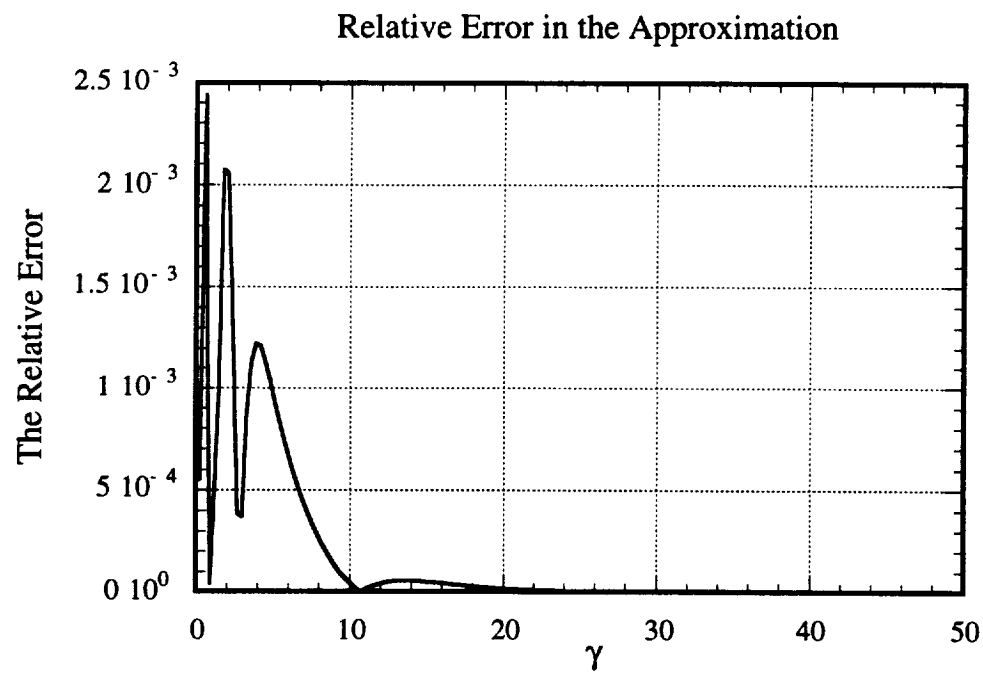
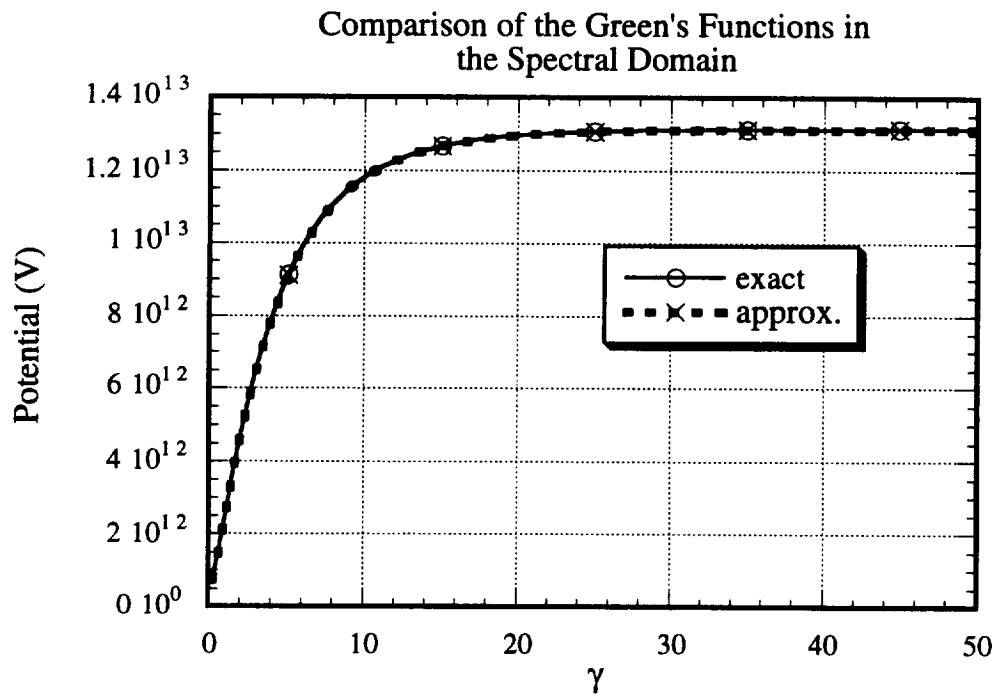


Figure 2.10. Comparison of approximated and exact Green's functions in the spectral domain for the medium shown in Fig. 2.9.

2.6 Physical Interpretation of the Closed-Form Green's Functions

As shown in the previous section, the closed-form Green's function well approximated the exact Green's function, which requires an infinite number of images, using only a finite number of weighted images. In this section, the underlying physics of this closed-form Green's function is discussed to understand the difference between the images due to the image principle and the exponential approximation.

Let us first assume that we are only interested in the circular region around a point source as depicted in Fig. 2.11(a). Then, the infinite number of images in the exact Green's function may be truncated to a finite number of images to evaluate the potential due to this point source inside of the region of interest up to a certain desired accuracy as shown in Fig. 2.11(b). This finite number of images is spaced and weighted such that its extension to the infinite number of images satisfies the boundary condition at the dielectric interface over infinite distances. The boundary condition on the portion of the dielectric interface that lies inside the region of interest may still be satisfied by employing a new set of images, which are nonuniformly spaced and weighted. Because of the nonuniform spacing and weighting, the smaller number of images than the one for Fig. 2.11(b) may be required to satisfy the boundary condition as illustrated in Fig. 2.11(c). Thus, the finite weighted images in the closed-form Green's function may be used to evaluate the potential distribution inside this region of interest.

Since the closed-form Green's function utilizes only a finite number of images, these images are located over a finite region; thus, these images cannot satisfy the boundary condition at large distances and may not be used to evaluate the potential at such large distances. The similar situation applies to the truncated version of an infinite number of images. However, the valid range of the weighted images resulting from the spectral-domain exponential approximation turns out to be large enough for most practical problems. For instance, the mutual capacitance between the two conductors computed using the closed-form Green's function is accurate until the separation distance between the two conductors becomes large enough that the mutual capacitance becomes negligible as compared to the self-capacitances.

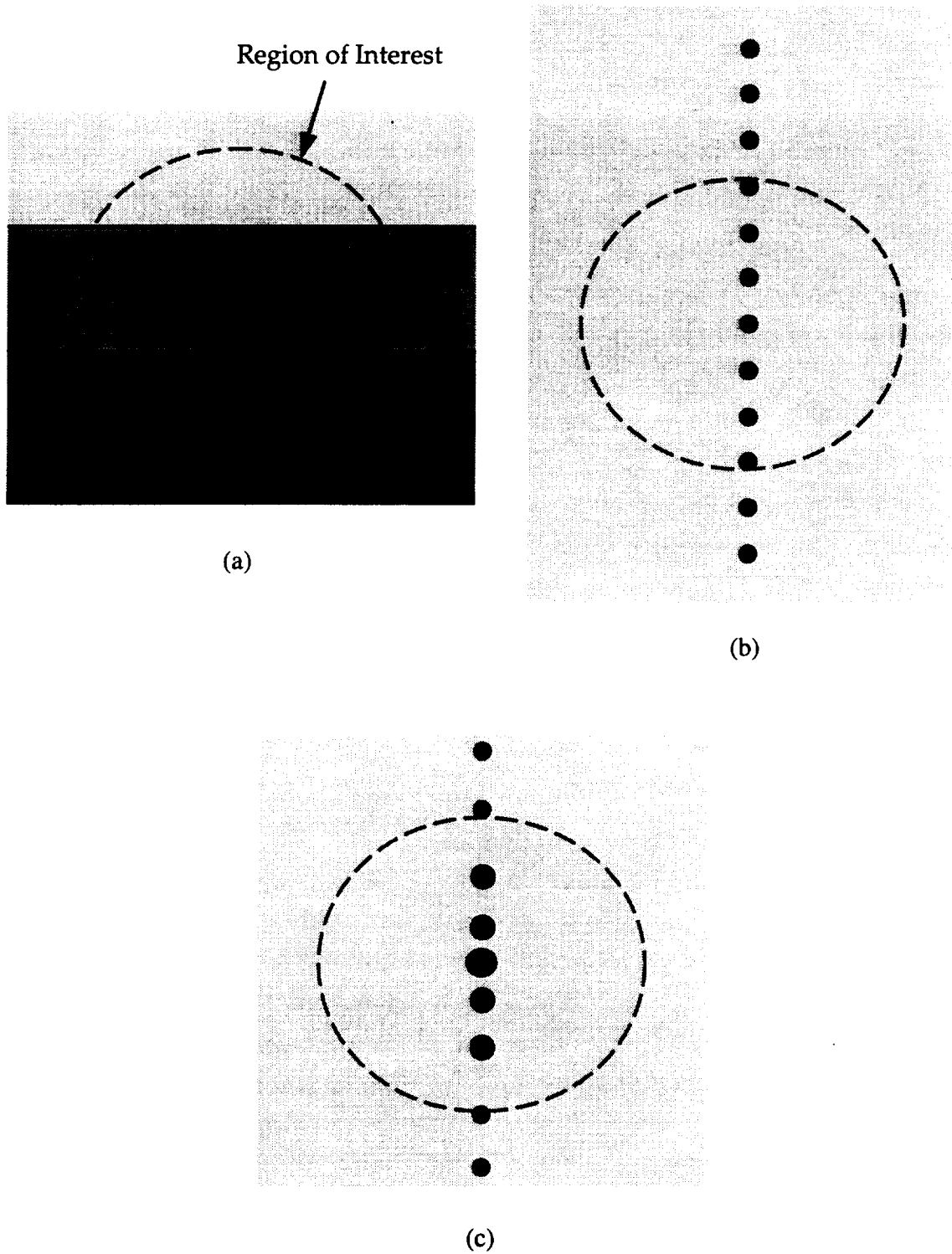


Figure 2.11. (a) A point source in inhomogeneous media and its equivalent systems using (b) the image theory and (c) weighted images.

2.7 Summary

Numerically efficient forms of the Green's functions for a point charge, a line charge, and a semi-infinite line charge embedded in a multilayered dielectric media with two optional ground planes were presented in this chapter. The presented Green's functions are approximate and utilize a finite number of weighted images instead of an infinite number of images used in the conventional exact Green's function. The analytical integration formulas to integrate these Green's functions to evaluate the elements of the moment matrices and the excitation vectors were also presented.

2.8 References

- [1] T. Itoh, Ed., *Numerical Techniques for Microwave and Millimeter-Wave Passive Structures*. New York, NY: Wiley, 1989.
- [2] W. C. Chew, *Waves and Fields in Inhomogeneous Media*. New York, NY: Van Nostrand Reinhold, 1990.
- [3] R. Crapagne, M. Ahmadpanah, and J.-L. Guiraud, "A simple method for determining the Green's function for a large class of MIC lines having multilayered dielectric structures," *IEEE Trans. Microwave Theory Tech.*, vol. 26, pp. 82-87, February 1978.
- [4] N. Farrar and A. T. Adams, "Multilayered microstrip transmission lines," *IEEE Trans. Microwave Theory Tech.*, vol. 22, pp. 889-891, October 1974.
- [5] R. Marques, M. Horno, and R. Medina, "A new recurrence method for determining the Green's function of planar structures with arbitrary anisotropic layers," *IEEE Trans. Microwave Theory Tech.*, vol. 33, pp. 424-428, May 1985.
- [6] W. Delbare and D. D. Zutter, "Space-domain Green's function approach to the capacitance calculation of multiconductor lines in multilayered dielectrics with improved surface charge modeling," *IEEE Trans. Microwave Theory Tech.*, vol. 37, pp. 1562-1568, October 1989.
- [7] K. A. Michalski and D. Zheng, "Electromagnetic scattering and radiation by surfaces of arbitrary shape in layered media, part II: implementation and results for contiguous half-spaces," *IEEE Trans. Antennas Propagat.* vol. 38, pp. 345-352, March 1990.
- [8] Y. L. Chow, J. J. Yang, and G. E. Howard, "Complex images for electrostatic field computation in multilayered media," *IEEE Trans. Microwave Theory Tech.*, vol. 40, pp. 1120-1125, July 1991.
- [9] S. L. Marple, *Digital Spectral Analysis*. Englewood Cliffs, NJ: Prentice-Hall, 1987.

- [10] Y. Hua and T. K. Sarkar, "Generalized pencil-of-function method for extracting poles of an EM system from its transient response," *IEEE Trans. Antennas Propagat.*, vol. 37, pp. 229-234, February 1989.
- [11] Y. L. Chow, J. J. Yang, D. G. Fang, and G. E. Howard, "A closed-form spatial Green's functions," *IEEE Trans. Microwave Theory Tech.* vol. 39, pp. 588-592, March 1991.
- [12] M. I. Aksun and R. Mittra, "Derivation of closed-form Green's functions for a general microstrip geometry," *IEEE Trans. Microwave Theory Tech.* vol. 40, pp. 2055-2062, November 1992.
- [13] I. Park, R. Mittra, and M. I. Aksun, "Numerically efficient analysis of planar microstrip configurations using closed-form Green's functions," *IEEE Trans. Microwave Theory Tech.* vol. 43, pp. 394-400, February 1995.
- [14] D. B. Kuznetsov, "Transmission line modeling and transient simulation," M.S. thesis, University of Illinois at Urbana-Champaign, 1992.
- [15] P. Silvester and P. B. Benedek, "Equivalent capacitances of microstrip open circuits," *IEEE Trans. Microwave Theory Tech.*, vol. 20, pp. 511-516, Aug. 1972.
- [16] M. Abramowitz and I. A. Stegun, Ed., *Handbook of Mathematical Functions*. New York, NY: Dover, 1972.
- [17] D. W. Kammer, "Calculation of characteristic admittances and coupling coefficients for strip transmission lines," *IEEE Trans. Microwave Theory Tech.*, vol. 16, pp. 925-937, Nov. 1968.
- [18] D. R. Wilton et al., "Potential integrals for uniform and linear source distributions on polygon and polyhedral domains," *IEEE Trans. Antennas Propagat.*, vol. 32, pp. 276-281, March 1984.
- [19] Stephen Wolfram, *Mathematica*. Redwood, CA: Addison-Wesley, 1991.

CHAPTER 3

COMPUTATION OF THE TRANSMISSION PARAMETERS OF A MULTICONDUCTOR SYSTEM

3.1 Introduction

As the word “transmission” implies, electromagnetic fields associated with a transmission line are dynamic in nature. However, for TEM lines, the transverse distribution of the fields at any instant of time is identical to that for the static solution. As a consequence, the four parameters for multiconductor TEM transmission lines, viz., the resistance matrix \mathbf{R} , the inductance matrix \mathbf{L} , the conductance matrix \mathbf{G} , and the capacitance matrix \mathbf{C} , may be derived from a static analysis with good accuracy. Similarly, under the quasi-TEM approximation, the spatial distribution of the fields in a multilayered dielectric medium is essentially identical to that predicted by the static analysis; hence, the \mathbf{R} , \mathbf{L} , \mathbf{G} , and \mathbf{C} matrices obtained from the static analysis still represent good approximations to the quasi-TEM transmission line parameters.

It is well-known that by making an analogy between electrostatic and magnetostatic problems for uniform transmission line configurations, both the charge and current distributions can be obtained from the electrostatic analysis [1], and the capacitance matrix \mathbf{C} and the inductance matrix \mathbf{L} follow from these distributions. Among various methods to determine the charge distribution on a multiconductor system [1]-[9], the most common method is the integral equation approach. A brief comparison of various methods used for electrostatic problems was presented in Section 1.3. In this chapter, an integral equation is formulated in terms of the closed-form Green’s function derived in the previous chapter; thus, the charge distribution is determined in an efficient manner such that no nested infinite summations nor numerical integrations are performed. To determine the current distribution, the equivalent electrostatic problem is solved using the same technique employed in the computation of the charge distribution.

Losses due to imperfect dielectrics by themselves do not alter the quasi-TEM nature of multiconductor transmission lines; hence, the conductance matrix \mathbf{G} can still be computed from the solution of the electrostatic problem by introducing a complex dielectric constant to account for the finite loss tangent [10], [11]. This procedure, however, is computationally inefficient (compared to the proposed method in this chapter) as it involves complex operations. An alternate approach, which is based on the conductance analogy of

capacitances, is often applied to single lines (two conductors) embedded in a homogeneous medium. In this chapter, the above concept is generalized to compute the conductance matrix \mathbf{G} of n -lines embedded in a multilayered dielectric medium.

Unlike the case for the computation of the conductance matrix, where the electrostatic problem could have been formulated with a complex permittivity, a formulation for the resistance matrix \mathbf{R} in the quasi-static regime is not so evident since the quasi-TEM approximation inevitably neglects the longitudinal components of fields, which must be present due to the conductor loss. The incremental induction method [12] is commonly used to compute the resistance for single line cases; however, it cannot be applied to general multiconductor cases. Yet another commonly used method is one based on the perturbational analysis on attenuation constants [10]. This approach first computes the attenuation constant by taking the ratio of the perturbed modal power loss and the total modal power of a lossless system; then, the resistance matrix is obtained by solving a set of N^2 linear equations for N modes, and the resulting resistance matrix is shown to be nondiagonal. Although this approach is variational (second-order accurate) in terms of attenuation constants, it is no longer variational for the resistance matrix.

As indicated in [11] and Section 3.5 in this chapter, the resistance matrix of coupled transmission lines is a nondiagonal matrix and is strongly dependent upon the choice of the current excitations used in the computation; the value of the resistance matrix varies significantly as different current excitations are used. This undesirable phenomenon is more prominent for the off-diagonal elements of the resistance matrix, and prevents the computation of \mathbf{R} without the knowledge of the actual current distribution, which is known only in the simulation time. Consequently, the nondiagonal matrix form of the \mathbf{R} matrix may be of no practical use. In this chapter, the diagonal matrix form of the resistance matrix, which is computed from the total power loss, is proposed. The resulting matrix is shown to be relatively insensitive to the choice of current excitations; hence, the proposed diagonal matrix is more suitable for the computation of the resistance matrix. Furthermore, the procedure to compute this matrix does not involve eigenvalue analysis unlike the perturbational approach mentioned previously.

In the following four sections, the details of the previously proposed methods to compute \mathbf{C} , \mathbf{L} , \mathbf{G} , and \mathbf{R} matrices of a multiconductor system is presented. Figure 3.1

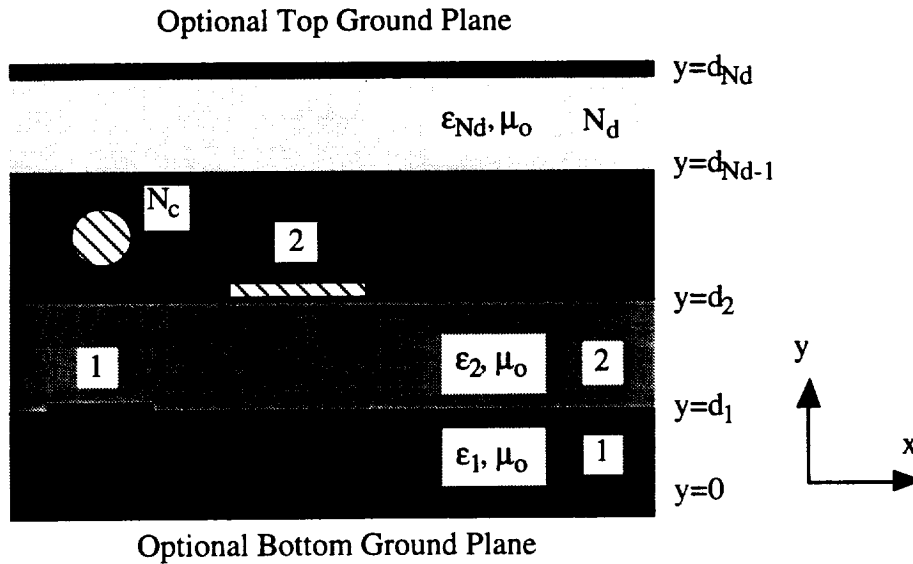


Figure 3.1. The cross-sectional view of a possible configuration of multiconductors in a multilayered dielectric medium.

demonstrates the general geometry of a multiconductor system embedded in a multilayered dielectric medium. The dielectric layers are the same as the ones considered in the previous chapter. An arbitrary number N_c of conductors are placed throughout the layers, and the cross sections and planar geometries of the conductors can be arbitrary as long as their boundaries can be described with a piecewise linear function.

3.2 Computation of the Capacitance Matrix

3.2.1 Theory

An impressed potential on conductors results in free charge accumulation on the surfaces of conductors, and the electrostatic potential $\phi(r)$ at any point except inside the conductors is then related to this surface charge density $q(\rho)$ per unit length via the following integral equation:

$$\phi(r) = \int_{\Omega} G^{2D}(\rho|\rho') q(\rho') dr' = \langle G^{2D}, q \rangle \quad (3.1)$$

where Ω denotes the contours of all conductors except for ground planes. $G^{2D}(\rho|\rho')$ is the 2-D closed-form Green's function for a multilayered medium discussed in the previous

chapter, and it accounts for polarization charges on the dielectric and conductor interfaces and free charges on the surfaces of ground planes. The integration is symbolically written as $\langle \cdot, \cdot \rangle$ to simplify the notation. To solve the above integral equation numerically, the method of collocation is used. First, the conductors are approximated with polygons and the unknown charge density is expanded with the pulse basis functions; then, the point matching technique is applied to the centers of each basis functions. The integral equation (3.1) can now be put into the following matrix form:

$$\begin{bmatrix} \bar{V}_1 \\ \bar{V}_2 \\ \cdot \\ \bar{V}_{N_c} \end{bmatrix} = \mathbf{M} \begin{bmatrix} \bar{q}_1 \\ \bar{q}_2 \\ \cdot \\ \bar{q}_{N_c} \end{bmatrix} = \begin{bmatrix} \mathbf{M}_{1,1} & \mathbf{M}_{1,2} & \cdot & \mathbf{M}_{1,N_c} \\ \mathbf{M}_{2,1} & \cdot & & \\ \cdot & & & \\ \mathbf{M}_{N_c,1} & & & \mathbf{M}_{N_c,N_c} \end{bmatrix} \begin{bmatrix} \bar{q}_1 \\ \bar{q}_2 \\ \cdot \\ \bar{q}_{N_c} \end{bmatrix} \quad (3.2a)$$

where

$$\bar{V}_i = [V_i, \dots, V_i]^T \quad (3.2b)$$

$$\bar{q}_i = [q_1^i, \dots, q_{N_i}^i]^T \quad (3.2c)$$

$$[\mathbf{M}_{i,j}]_{p,q} = \int_{\Gamma_q^j} G^{2D}(\rho_c^{i,p} | \rho) d\rho \quad (3.2d)$$

where the superscript T denotes the transpose, \bar{V}_i and \bar{q}_i are vectors of size N_i , and $\mathbf{M}_{i,j}$ is an N_i by N_j matrix, where N_j is the number of basis functions used to discretize the j th conductor. V_i is the voltage of the i th conductor with respect to the ground planes, q_j^i is the unknown coefficient associated with the j th basis function of the i th conductor, Γ_q^j is the q th line segment of the j th conductor, and $\rho_c^{i,p}$ is the center point of the p th basis function of the i th conductor. The expression of $G^{2D}(\rho | \rho')$ is given in Section 2.3, and the closed-form formula for the integration in (3.2d) is discussed in Section 2.4. Now, given the excitation voltages, the corresponding charge distribution can be determined by solving the linear system of Equations (3.2).

The capacitance matrix \mathbf{C} is defined to relate the total free charges on the conductors to the voltages in the following manner:

$$\mathbf{C}\bar{V} = \bar{Q} \quad (3.3a)$$

where the i th elements of \bar{V} and \bar{Q} are the voltage and the total charge of the i th conductor, and the i th element of \bar{Q} , Q_i , is given by

$$Q_i = \sum_{j=1}^{N_i} l_j^i q_j^i \quad (3.3b)$$

Here, l_j^i and q_j^i are the length and the charge density coefficient of the j th segment of the i th conductor.

The capacitance matrix can now be determined by solving the charge distributions for N independent voltage excitation vectors and can be put into the following matrix form:

$$\mathbf{C} = \mathbf{QV}^{-1} \quad (3.4)$$

where the i th columns of \mathbf{V} and \mathbf{Q} are the i th voltage excitation vector and charge vector. To avoid the matrix inversion, the identity matrix is chosen for the \mathbf{V} matrix in this chapter. With this choice of \mathbf{V} matrix, \mathbf{C} is simply equal to \mathbf{Q} , and the following physical properties of the capacitance matrix can be deduced:

- Since \mathbf{Q} is symmetric due to reciprocity, \mathbf{C} is also symmetric:

$$C_{i,j} = C_{j,i} \quad (3.5a)$$

- Since the diagonal elements of \mathbf{Q} are the charges on the excited conductors and the off-diagonal elements of \mathbf{Q} are the induced charges on the rested conductors, the diagonal elements of \mathbf{Q} are positive and all of the off-diagonal elements are negative:

$$C_{i,i} > 0 \text{ and } C_{i,j} < 0 \text{ for } j \neq i \quad (3.5b)$$

- Furthermore, the magnitude of the sum of the induced charges must be smaller than the charges on the excited conductor; hence, \mathbf{C} is a positive definite matrix:

$$|C_{i,i}| > \left| \sum_{j \neq i} C_{i,j} \right| \quad (3.5c)$$

The capacitance matrix defined by (3.3) is called the Maxwellian capacitance, and the physical self- and mutual capacitances are related to this Maxwellian capacitance matrix by

$$C_{i,j} = -C_{i,j}^m \quad (3.6a)$$

$$C_{i,i} = C^s + \sum_{j \neq i} C_{i,j}^m \quad (3.6b)$$

So far, we have implicitly assumed that there is at least one ground plane, which is the reference conductor. If there are no ground planes, any one of the conductors can be chosen as a reference conductor, and the terms corresponding to this reference conductor should be removed in (3.3a) and (3.4). Unfortunately, when there are no ground planes, the physical condition in which the total charges in the system must add to zero for 2-D problems is not necessarily satisfied by the integral equation (3.1), which was naturally enforced by the Green's function when there is at least one ground plane. Thus, this condition must be incorporated into (3.1) to obtain the correct charge distribution. To enforce this condition, another row is added to (3.2) as follows:

$$\begin{bmatrix} \bullet \\ \bullet \\ \bullet \\ 0 \end{bmatrix} = \begin{bmatrix} \bullet & \bullet & \bullet & \bullet \\ \bullet & \bullet & \bullet & \bullet \\ \bullet & \bullet & \bullet & \bullet \\ 1 & 1 & 1 & 0 \end{bmatrix} \begin{bmatrix} \bullet \\ \bullet \\ \bullet \\ -V_{ref} \end{bmatrix} \quad (3.7)$$

where V_{ref} is the potential value at the reference conductor, which is yet to be determined.

It is interesting to note why the above physical condition has to be satisfied in addition to the boundary condition embedded in (3.2) in spite of the facts that all necessary boundary conditions appeared to be embedded in (3.2) and that the solution of the Laplace equation is unique once the boundary conditions are satisfied. The answer to this question is that since the magnitudes of the fields have to be finite everywhere except at the source region, they have to be finite at infinity also, and this boundary condition at infinity turns out to be missing in the integral equation (3.1) for cases in which no ground plane is presented. This boundary condition at infinity can be enforced by setting the total charge in the system to zero. It should be noted that when there is one ground plane, this boundary

is embedded in the Green's function, and when dielectric layers are bounded by two ground planes, this boundary condition no longer has to be satisfied.

3.2.2 Numerical examples

In this section, various numerical examples are given to verify the method discussed in the previous section. As a first example, a single microstrip line shown in Fig. 3.2 is considered. The line thickness was taken to be infinitely thin. The capacitance value is computed with various numbers of basis functions, and the result is compared with those for the iterative spectral-domain technique [13], [14] in Fig. 3.3. This spectral domain method solves the integral equation iteratively in conjunction with the minimization in the boundary condition error. The maximum number of exponential functions used in the approximation of each coefficient function was seven. The charge density on the microstrip is plotted in Fig. 3.4.

A more complex geometry, a three-conductor system in a layered medium, shown in Fig. 3.5, is considered. The number of basis functions used was fifty for each conductor. Again, the maximum number of exponential functions used in the approximation was seven. A comparison with the results obtained from [4] is shown in Table 3.1. In [4], the spectral-domain Green's function is numerically integrated to obtain the space-domain Green's function using a Gaussian quadrature formula in conjunction with an analytical asymptotic extraction. The potential distribution in the system with the excitation at the center conductor is plotted in Fig. 3.6. The white spaces in Fig 3.6 represent the conductors.

A ten-conductor transmission-line system above a thick dielectric substrate, shown in Fig. 3.7, is also considered. The total number of 300 basis functions was used to represent the unknown charges, and nine exponential functions were used to approximate each coefficient function of the Green's function. Table 3.2 shows the computed results. The same structure is considered in [3] using the free-space Green's function with the basis functions, which incorporate the edge singularities of the charge near the corners of the conductors. In [3], data are obtained using 160 and 190 basis functions for conductors and dielectric interfaces, respectively. The methods used in [1] and [4] are also employed to compute the capacitance matrix of the same structure in [3]. According to [3], the methods used in [1] and [4] resulted in nonphysical values, for instance, negative self-capacitance

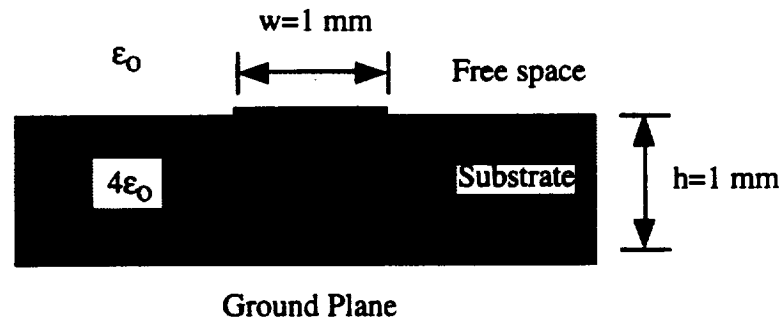


Figure 3.2. A single microstrip line.

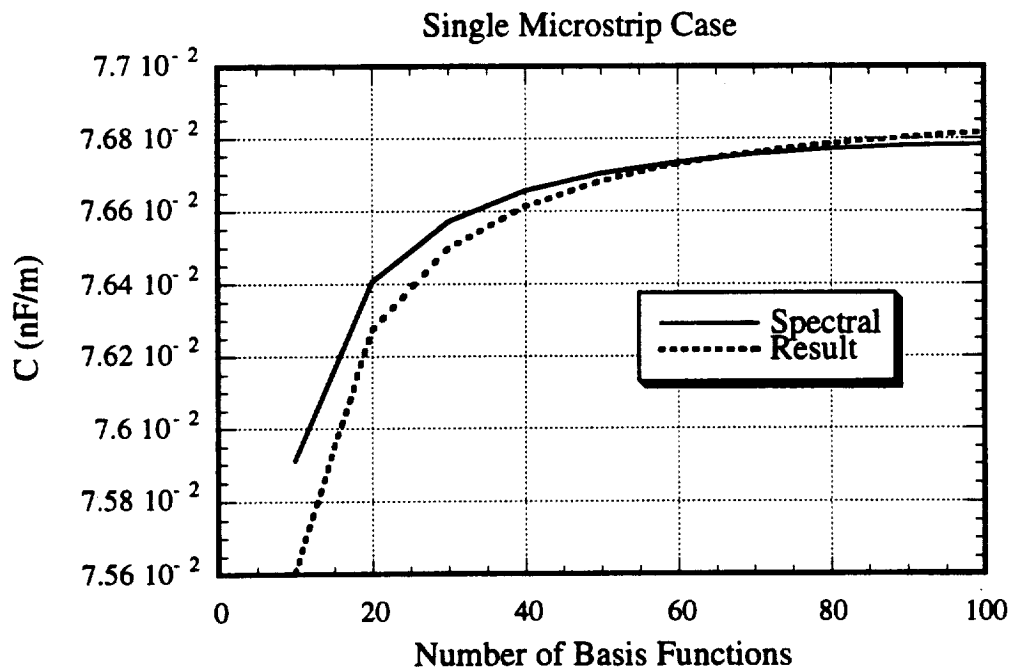


Figure 3.3. Comparison of the present method with the spectral domain approach as a function of the number of basis functions.

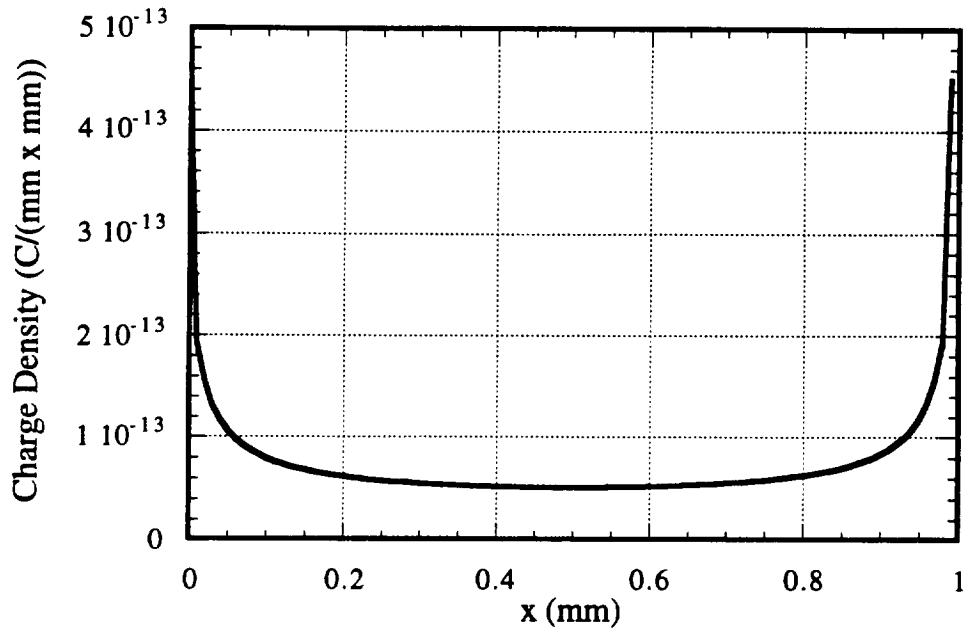


Figure 3.4. The plot of the surface charge density on the microstrip shown in Fig. 3.2.

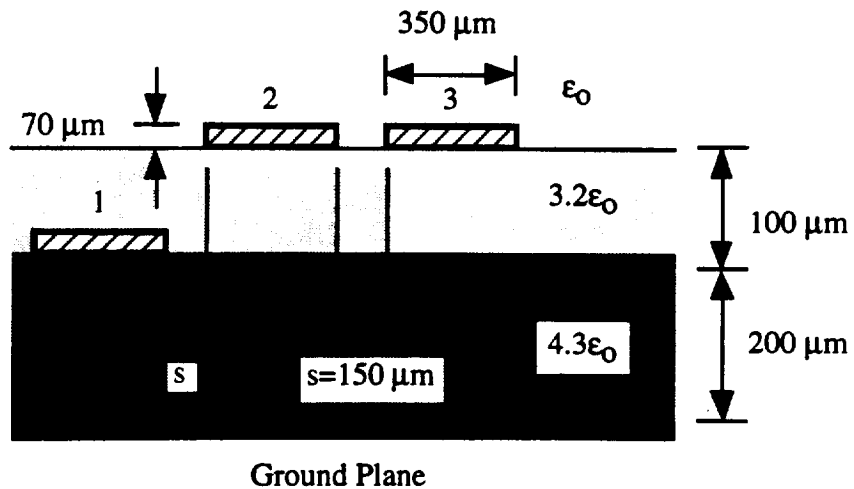


Figure 3.5. Three conductors in a layered medium. All dimensions of conductors and spacings are identical.

Table 3.1. Comparison of the capacitance matrix for the three-conductor structure shown in Fig. 3.5 with [4].

Computation	Delbare and Zutter [4]
$\begin{bmatrix} 141.41 & -21.492 & -0.8952 \\ -21.492 & 92.951 & -17.859 \\ -0.8952 & -17.859 & 87.494 \end{bmatrix} \text{ (pF/m)}$	$\begin{bmatrix} 142.09 & -21.765 & -0.8920 \\ -21.733 & 93.529 & -18.098 \\ -0.8900 & -18.097 & 87.962 \end{bmatrix} \text{ (pF/m)}$

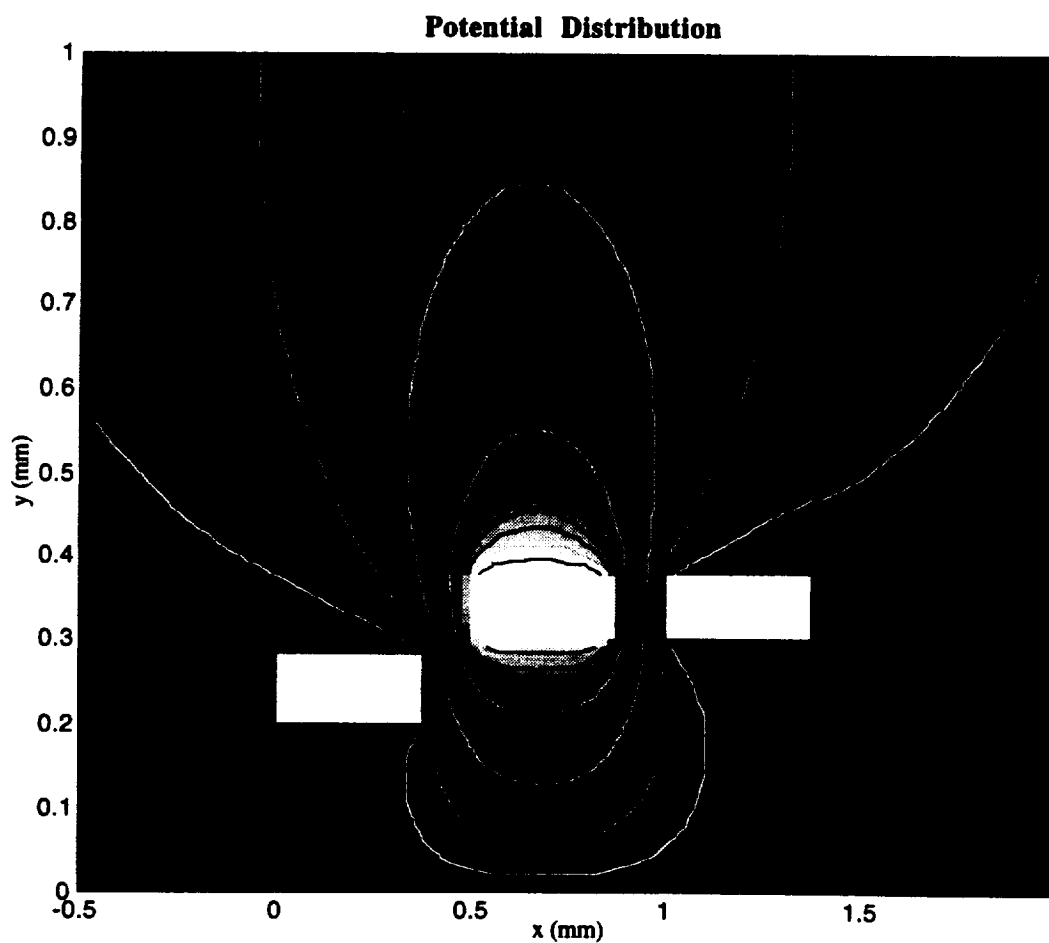


Figure 3.6. The potential distribution of the system shown in Fig. 3.5 with the excitation at the center conductor.

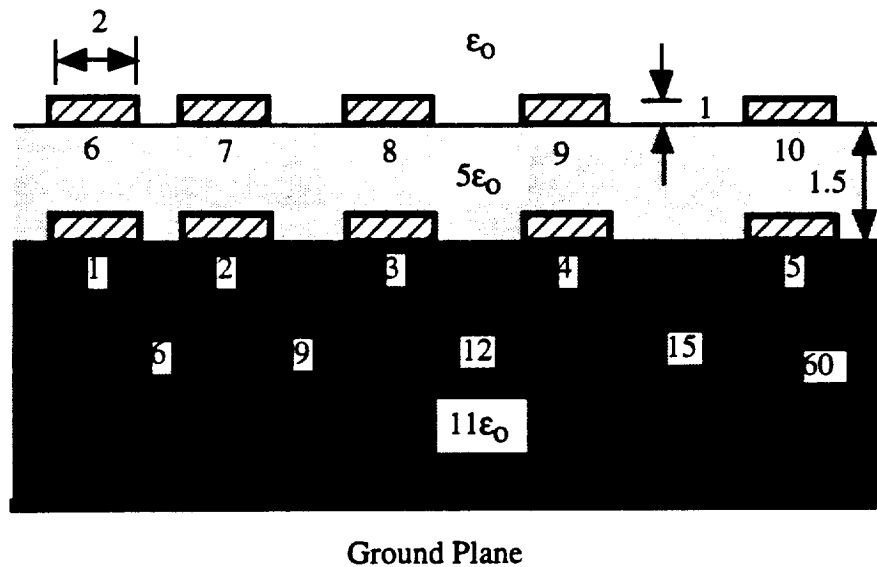


Figure 3.7. Ten conductors in a layered medium. Dimensions of conductors are identical, and all units are in micrometers.

Table 3.2. Capacitance matrix (pF/m) for the ten-conductor system shown in Fig. 3.7.

307.13	-41.2	-11.34	-6.28	-5.351	-218.8	-4.966	-1.385	-0.814	-0.729
-41.20	319.6	-28.04	-7.79	-4.987	-5.025	-216.95	-3.54	-0.985	-0.666
-11.34	-28.04	310.5	-24.29	-8.587	-1.366	-3.503	-218.4	-3.18	-1.148
-6.279	-7.79	-24.29	303.5	-24.73	-0.798	-0.946	-3.164	-219.4	-3.345
-5.351	-4.988	-8.588	-24.73	290.5	-0.708	-0.627	-1.12	-3.325	-221.3
-218.8	-5.01	-1.363	-0.796	-0.709	231.7	-2.074	-0.393	-0.182	-0.134
-4.954	-216.97	-3.494	-0.944	-0.628	-2.074	232.0	-1.19	-0.255	-0.135
-1.382	-3.532	-218.4	-3.157	-1.12	-0.393	-1.19	231.8	-0.8752	-0.242
-0.813	-0.982	-3.174	-219.5	-3.32	-0.182	-0.255	-0.875	231.6	-0.763
-0.729	-0.665	-1.145	-3.34	-221.4	-0.134	-0.135	-0.242	-0.763	231.3

values. The capacitance values given in Table 3.2 are stable and agree well with the ones given in [3]. The method used in [4] required the CPU times of 89611.19 s on an IBM RS-6000 station with 300 basis functions, whereas the method in [3] took 458.67 s. On the same machine, the presented method took only 85.7 s of CPU time.

For the final 2-D example, a multilayered stripline case, shown in Fig. 3.8, is also analyzed. Fifty basis functions are used to discretize each conductor. The computed capacitances were $C_{11} = C_{22} = 217.07$ pF/m and $C_{12} = C_{21} = -107.76$ pF/m. Data obtained from the Ansoft Maxwell software are $C_{11} = C_{22} = 217.65$ pF/m and $C_{12} = C_{21} = -108.24$ pF/m.

3.3 Computation of the Inductance Matrix

Inductances are obtained by solving magnetostatic problems, which, in general, are governed by a vector equation unlike electrostatic problems, which are governed by a scalar equation. As a consequence, the computations of inductances are often computationally more intensive than the computations of capacitances. However, for 2-D problems (the uniform transmission-line configurations) the magnetostatic problems can also be written by a scalar equation using only the z -component of the magnetic vector potential \vec{A} . For

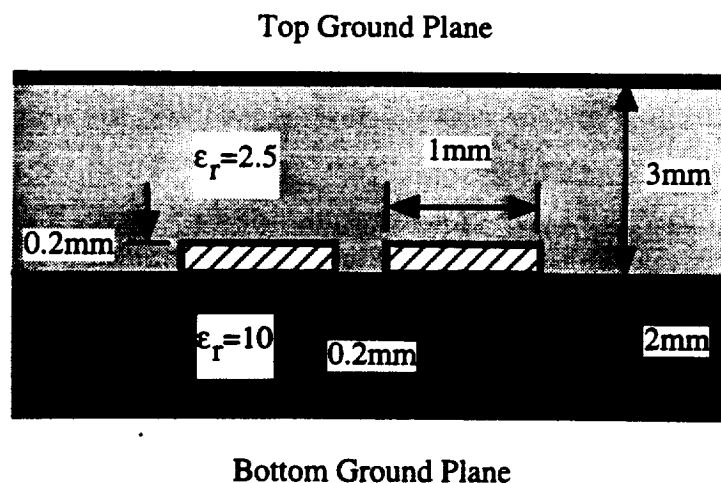


Figure 3.8. Two conductors in a layered medium with two ground planes. Dimensions of conductors are identical.

these configurations, an isomorphism exists between the magnetostatic and electrostatic problems [1], [15], and the solutions of the magnetostatic problems are often obtained from solving the equivalent electrostatic problems. Therefore, the technique used to solve the capacitance in the previous section can still be applied to the inductance calculation.

In the following subsection, this isomorphism between magnetostatic and electrostatic problems is first discussed, and then the expression relates the inductance matrix to the capacitance matrix of the equivalent electrostatic problem is derived.

3.3.1 Isomorphism between electrostatic and magnetostatic problems

To simplify the analysis, we will assume that there are two isotropic layers. Then, at the source-free region, electrostatic problems for a multiconductor system embedded in a multilayered medium are governed by the following Laplace equation:

$$\frac{\partial^2 V_i}{\partial x^2} + \frac{\partial^2 V_i}{\partial y^2} = \nabla_t^2 V_i = 0 \quad i = 1, 2 \quad (3.8)$$

where V_i is the potential distribution in the i th layer, and the associated boundary condition at the dielectric interface is

$$E_1^t = E_2^t \quad D_1^n = D_2^n \quad (3.9)$$

Here, the superscripts t and n denote the transverse and normal components of the vectors. Rewriting the above equations in terms of V_i ,

$$(\hat{z} \times \hat{n}) \cdot \nabla_t V_1 = (\hat{z} \times \hat{n}) \cdot \nabla_t V_2 \quad \hat{n} \cdot (\epsilon_{r1} \nabla_t V_1) = \hat{n} \cdot (\epsilon_{r2} \nabla_t V_2) \quad (3.10)$$

The associated boundary condition of (3.8) at the conductor interface is

$$E_i^t = 0 \quad D_i^n = -q_s \quad (3.11)$$

where q_s is the surface charge density, and again, rewriting (3.11) in terms of V_i ,

$$(\hat{z} \times \hat{n}) \cdot \nabla_t V_i = 0 \quad \hat{n} \cdot (\epsilon_{ri} \nabla_t V_i) = -\frac{q_s}{\epsilon_0} \quad (3.12)$$

Now for magnetostatic problems, we have the following equation at the source-free region:

$$\nabla_t \times \bar{B}_i = 0 \quad i = 1, 2 \quad (3.13)$$

where \bar{B}_i is the magnetic flux density in the i th layer. Using the facts, $\bar{B}_i = \nabla \times \bar{A}_i$ and only the z -component of the magnetic vector potential \bar{A}_i is nonzero under the quasi-static approximation, the above equation can be written as

$$\nabla_t \times (\hat{z} \times \nabla_t A_{zi}) = \hat{z}(\nabla_t \cdot \nabla_t A_{zi}) = 0 \Rightarrow \nabla_t^2 A_{zi} = 0 \quad (3.14)$$

The associated boundary condition of (3.13) at the dielectric interface is

$$H_1^t = H_2^t \quad B_1^n = B_2^n \quad (3.15)$$

and the above equations in terms of A_{zi} are

$$\hat{n} \cdot \left(\frac{1}{\mu_{r1}} \nabla_t A_{z1} \right) = \hat{n} \cdot \left(\frac{1}{\mu_{r2}} \nabla_t A_{z2} \right) \quad \hat{n} \cdot (\hat{z} \times \nabla_t A_{z1}) = \hat{n} \cdot (\hat{z} \times \nabla_t A_{z2}) \quad (3.16)$$

Applying vector identities to the above equations, we have

$$\hat{n} \cdot \left(\frac{1}{\mu_{r1}} \nabla_t A_{z1} \right) = \hat{n} \cdot \left(\frac{1}{\mu_{r2}} \nabla_t A_{z2} \right) \quad (\hat{i} \times \hat{n}) \cdot \nabla_t A_{z1} = (\hat{i} \times \hat{n}) \cdot \nabla_t A_{z2} \quad (3.17)$$

The associated boundary condition of (3.13) at the conductor interface is

$$\hat{n} \times \bar{H}_i = J_z \hat{z} \quad B_1^n = 0 \quad (3.18)$$

where J_z is the longitudinal surface current density, and again, rewriting the above conditions in terms of A_{zi} ,

$$\hat{n} \cdot \left(\frac{1}{\mu_{ri}} \nabla_t A_{zi} \right) = -\mu_o J_z \quad (\hat{z} \times \hat{n}) \cdot \nabla_t A_{zi} = 0 \quad (3.19)$$

Now comparing (3.8), (3.10), and (3.12) with (3.14), (3.17), and (3.19), it is clear that if we replace $1/\mu_{ri}$ and $\mu_o J_z$ with ϵ_{ri} and q_s/ϵ_o in (3.17) and (3.19), A_{zi} is equal to V_i . Therefore, A_{zi} can be computed by solving the equivalent electrostatic problem with replacing ϵ_{ri} by $1/\mu_{ri}$, and the current distribution $J_z(\rho)$ can be obtained using the following formula:

$$J_z(\rho) = c^2 q_s(\rho) \quad (3.20)$$

where c is the speed of light, and $q_s(\rho)$ is the surface charge density of the equivalent electrostatic problem.

The inductance matrix \mathbf{L} is defined to relate the magnetic flux differences between the signal conductors and the reference conductor to the currents on the signal conductors in the following manner:

$$\mathbf{L}\bar{\mathbf{I}} = \bar{\boldsymbol{\psi}} \quad (3.21)$$

where the i th elements of $\bar{\boldsymbol{\psi}}$ and $\bar{\mathbf{I}}$ are the magnetic flux difference between the i th signal conductor and the reference conductor and the current on the i th conductor. The inductance matrix can now be determined by solving the current distributions for N independent $\bar{\psi}_i$ and can be put into the following matrix form:

$$\mathbf{L} = \boldsymbol{\psi}\mathbf{I}^{-1} \quad (3.22)$$

where the i th columns of $\boldsymbol{\psi}$ and \mathbf{I} are the i th magnetic flux excitation vector and current vector. Solving the equivalent electrostatic problem with $\mathbf{V} = \boldsymbol{\psi}$, and using the fact that $\mathbf{I} = c^2\mathbf{Q}_{\text{eq}}$, we have

$$\mathbf{L} = \frac{1}{c^2}\mathbf{C}_{\text{eq}}^{-1} \quad (3.23)$$

where \mathbf{Q}_{eq} and \mathbf{C}_{eq} are \mathbf{Q} and \mathbf{C} matrices in (3.4) for the equivalent electrostatic problem. For nonmagnetic media, the above equation becomes

$$\mathbf{L} = \frac{1}{c^2}\mathbf{C}_0^{-1} \quad (3.24)$$

where \mathbf{C}_0 is the capacitance matrix for a free-space case in which all dielectric layers are replaced with free space.

Since the inductance matrix is related to the inverse of the capacitance matrix, the following properties can be deduced from (3.5a), (3.5b), and (3.5c):

$$L_{i,j} = L_{j,i} \quad (3.25a)$$

$$L_{i,j} > 0 \quad (3.25b)$$

$$L_{i,i} > \sum_{j \neq i} L_{i,j} \quad (3.25c)$$

Hence, \mathbf{L} is also a positive definite symmetric matrix. This Maxwellian inductance matrix defined by (3.21) is related to the physical self- and mutual inductances by

$$L_{i,j} = L_{i,j}^m \quad (3.26a)$$

$$L_{i,i} = L^s \quad (3.26b)$$

3.3.2 Numerical examples

Since the inductance matrix can be obtained using the electrostatic solution technique discussed in Section 3.2 and this technique has been shown to be very accurate and efficient, the resulting inductance matrix from this technique is also expected to be accurate and efficient. Hence, only a few examples are presented for the inductance calculations in this section, and more examples will be given as the remaining two parameters, the conductance and resistance matrices, are discussed.

The three-conductor system shown in Fig. 3.9 is considered as a first example. The resulting capacitance and inductance matrices are compared with others in Table 3.3. The maximum number of exponential functions used in the approximation was seven, and 16 basis functions are used to discretize each rectangular conductor, whereas 24 basis functions are used for the circular conductor. For a second example, the three-conductor system shown in Fig. 3.5 in Section 3.2 is again considered, and a comparison with the result obtained from [4] is given in Table 3.4. An excellent agreement was found for both cases.

3.4 Computation of the Conductance Matrix

3.4.1 Theory

As mentioned in the beginning of this chapter, the inclusion of dielectric losses does not violate the quasi-static condition of a multiconductor system, and the conductance matrix \mathbf{G} , which models losses due to the finite loss tangent of an imperfect dielectric, can be computed from the solution of the Laplace equation by means of a complex dielectric constant [10]. Since the dielectric constant is complex for this approach, the closed-form

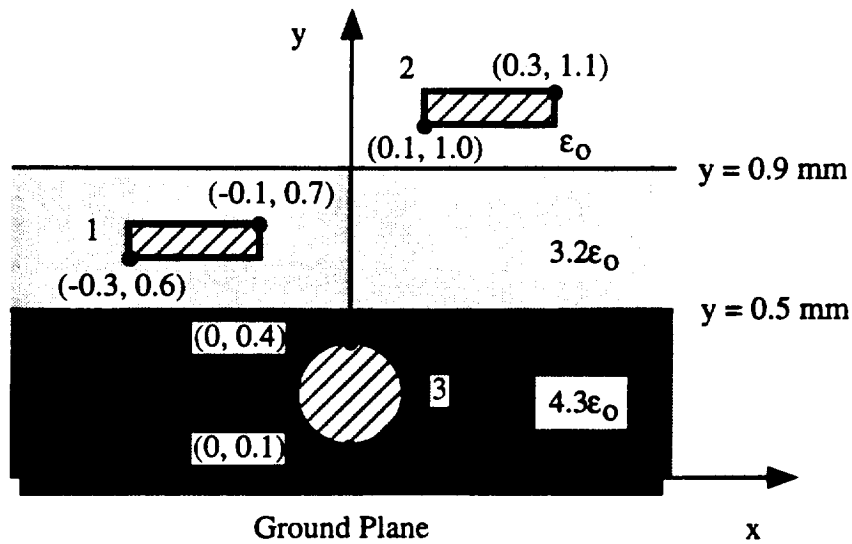


Figure 3.9. Three conductors in a layered medium. The dimensions used in coordinates are in millimeters.

Table 3.3. Comparison of the inductance matrix for the three-conductor structure shown in Fig. 3.9.

	C (pF/m)	L (nH/m)
Computation	$\begin{bmatrix} 116.9 & -13.33 & -62.79 \\ -13.33 & 33.71 & 74.96 \\ -62.79 & 74.96 & 362.3 \end{bmatrix}$	$\begin{bmatrix} 489.0 & 196.1 & 114.7 \\ 196.1 & 612.8 & 74.96 \\ 114.7 & 74.96 & 219.1 \end{bmatrix}$
Wei et al. [1]	$\begin{bmatrix} 124.4 & -13.00 & -68.25 \\ -13.00 & 33.40 & -7.196 \\ -68.25 & -7.196 & 352.3 \end{bmatrix}$	$\begin{bmatrix} 496.5 & 199.6 & 118.3 \\ 199.6 & 616.3 & 77.28 \\ 118.3 & 77.28 & 233.1 \end{bmatrix}$
Delbare and Zutter [4]	$\begin{bmatrix} 125.9 & -13.12 & -69.55 \\ -13.12 & 34.10 & -7.182 \\ -69.55 & -7.182 & 357.6 \end{bmatrix}$	$\begin{bmatrix} 491.9 & 198.9 & 117.5 \\ 198.9 & 612.83 & 76.781 \\ 117.5 & 76.781 & 229.94 \end{bmatrix}$

Table 3.4. Comparison of the inductance matrix for the three-conductor structure shown in Fig. 3.5 in Section 3.2 with [4].

Computation	Delbare and Zutter [4]
$\begin{bmatrix} 277.90 & 87.569 & 36.629 \\ 87.569 & 328.87 & 115.52 \\ 36.629 & 115.52 & 338.16 \end{bmatrix} \text{ (nH/m)}$	$\begin{bmatrix} 277.73 & 87.758 & 36.770 \\ 87.758 & 328.60 & 115.77 \\ 36.770 & 115.77 & 337.98 \end{bmatrix} \text{ (nH/m)}$

Green's function discussed in Chapter 2, which was obtained using the real exponential approximation, can no longer be applied. In principle, a new closed-form expression for the Green's function which accounts for the complex dielectric constant can be derived; however, this approach will be computationally intensive as it involves complex operations, and a simple perturbation approach is employed in this section.

The conductance matrix \mathbf{G} for a multiconductor system embedded in a multilayered lossy dielectric medium is defined by

$$\mathbf{G} \bar{\mathbf{V}}_i = \bar{\mathbf{I}}_i^s \quad i = 1, 2, \dots, N \quad (3.27)$$

where $\bar{\mathbf{V}}_i$'s are N independent line voltage vectors, $\bar{\mathbf{I}}_i^s$'s are the corresponding shunt current vectors per unit length that arise due to dielectric losses, and N is the number of modes (N signal conductors or N lines). Equation (3.27) in the matrix form is

$$\mathbf{G} = \mathbf{I}^s \mathbf{V}^{-1} \quad (3.28)$$

where the i th columns of matrices \mathbf{V} and \mathbf{I}^s are $\bar{\mathbf{V}}_i$ and $\bar{\mathbf{I}}_i^s$, respectively. The j th element of the matrix \mathbf{I} , which is the shunt current on the j th line due to the voltage excitation of $\bar{\mathbf{V}}_i$, can be obtained from the normal component of the electric field at the surface of the corresponding conductor of the j th line:

$$I_{j,i}^s = \oint_{c_j} J_i^s(\rho') d\rho' = \oint_{c_j} \sigma(\rho') \hat{n} \cdot \bar{\mathbf{E}}_i(\rho') d\rho' \quad (3.29)$$

Here, $J_i^s(\rho)$ and $\vec{E}_i(\rho)$ are the shunt surface current density and the electric field corresponding to the \vec{V}_i excitation vector, $\sigma(\rho)$ are the conductivities of the dielectric media, \hat{n} is the surface normal vector, and c_j is the surface contour of the conductor. Using the fact that the normal component of the displacement field at the surface of a conductor is related to the charge density, (3.29) can be rewritten as

$$I_{j,i}^s = \oint_{c_j} q^i(\rho') \sigma(\rho') / \epsilon(\rho') d\rho' \quad (3.30)$$

It can be shown that the potential distribution near the surface of the conductor does not change substantially when a slight loss is introduced in the dielectrics¹; consequently, neither the electric field nor the charge density is much different for the lossy and lossless cases on the conductor. Thus, the charge density from a lossless system, which can be determined using the method given in Section 3.2, can still be used as the charge density $q^i(\rho)$ of a lossy system. Finally, once the charge densities have been obtained for N independent voltage excitations from the lossless system, the conductance matrix \mathbf{G} can be derived from (3.28) and (3.30).

Since the \mathbf{I} matrix in (3.28) is directly related to the \mathbf{Q} matrix in (3.8), the properties of the conductance matrix are the same as that for the capacitance matrix:

$$G_{i,j} = G_{j,i} \quad (3.31a)$$

$$G_{i,i} > 0 \text{ and } G_{i,j} < 0 \text{ for } j \neq i \quad (3.31b)$$

$$|G_{i,i}| > \left| \sum_{j \neq i} G_{i,j} \right| \quad (3.31c)$$

and the relationship between the conductance matrix and the physical self- and mutual conductances is similar to that for the capacitance case, and is given by

$$G_{i,j} = -G_{i,j}^m \quad (3.32a)$$

¹This can be seen from the fact that neither the lines of force nor the equipotential lines near the surface of the conductor are affected by the introduction of the dielectric losses.

$$G_{i,i} = G^s + \sum_{j \neq i} G_{i,j}^m \quad (3.32b)$$

3.4.2 Numerical examples

A cylindrical conductor above a perfectly conducting ground plane shown in Fig. 3.10 is considered for a first example. Analytical formulas for the transmission line parameters of this system can be obtained from the two-wire line case [1], [17] and given by

$$L = \frac{\mu}{2\pi} \cosh^{-1}(2H/d) \quad (3.33a)$$

$$C = \frac{2\pi\epsilon}{\cosh^{-1}(2H/d)} \quad (3.33b)$$

$$R = \frac{2R_s H/d}{\pi d \sqrt{(2H/d)^2 - 1}} \quad (3.33c)$$

$$G = \frac{2\pi\sigma}{\cosh^{-1}(2H/d)} \quad (3.33d)$$

where H is the distance from the center of the cylinder to the ground plane, d is the diameter of the cylinder, R_s is the surface resistivity of the conductor, and σ is the conductivity of the dielectric medium. The computed results are compared in Table 3.5 with the analytical solutions and numerical results from [1]. Forty basis functions were used to solve the electrostatic problem. The comparison shows excellent agreement.

For the next example, the four-conductor system shown in Fig. 3.11 is considered, and the results are compared in Table 3.6. The loss tangents of the bottom, middle, and top dielectric layers are 6.4×10^{-4} , 8.6×10^{-4} , and 2.4×10^{-4} , respectively.

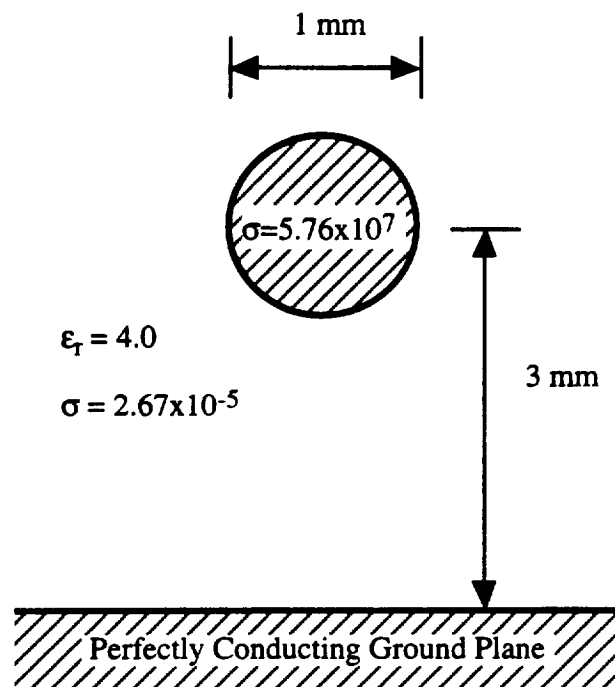


Figure 3.10. A cylindrical conductor above a PEC ground plane.

Table 3.5. Comparison of the computed data with the analytical solutions for the cylindrical case shown in Fig. 3.10.

	Analytical Solutions	Computed Data	Wei et al. [1]
C (pF/m)	89.80	89.75	89.44
G (μ S/m)	67.71	67.66	67.44

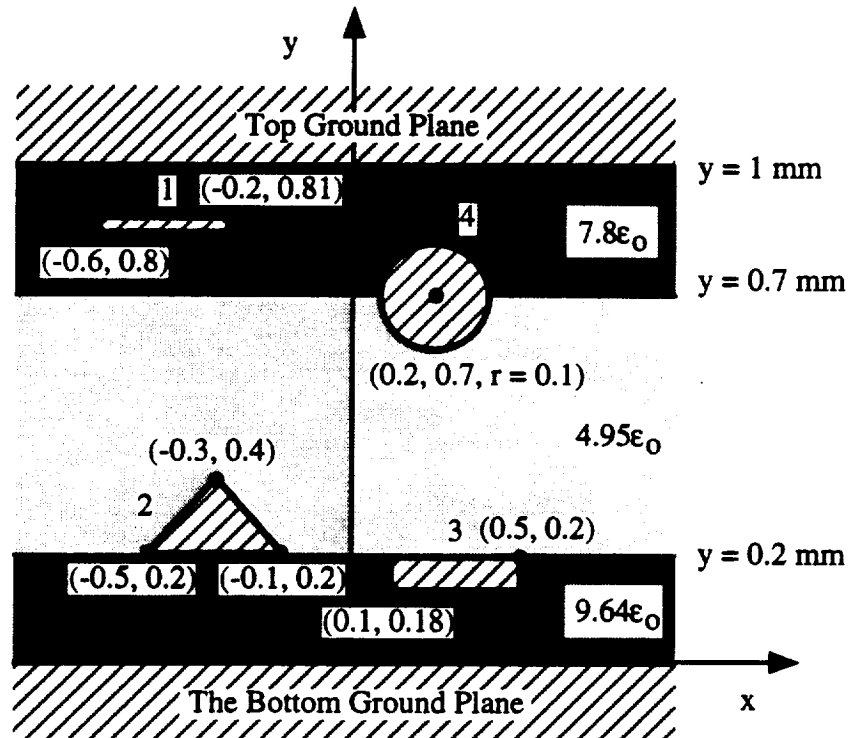


Figure 3.11. Four-conductor transmission lines embedded in a layered medium.

Table 3.6. Comparison of the computed results with data obtained from [1] for the four-conductor system shown in Fig. 3.11.

i	j	[C] _{ij} (pF/m)		[L] _{ij} (nH/m)		[G] _{ij} (nS/m)	
		Presented	[1]	Presented	[1]	Presented	[1]
1	1	316.9	308.8	264.9	271.4	477.8	642.0
1	2	-38.38	-36.06	43.71	44.88	-133.3	-170.1
1	3	-2.532	-2.848	13.18	12.95	-7.000	-13.27
1	4	-26.79	-24.59	34.70	34.42	-64.17	-60.70
2	2	360.3	333.1	248.3	259.4	1642	1481
2	3	-34.37	-30.45	35.52	34.47	-154.8	-149.8
2	4	-16.91	-16.41	36.83	37.42	-73.04	-96.88
3	3	372.1	380.6	251.7	257.0	1496	1608
3	4	-33.28	-31.78	51.77	52.48	-148.6	-177.7
4	4	242.1	232.8	320.8	332.6	694.0	638.3

3.5 Computation of the Resistance Matrix

3.5.1 Theory

At the frequencies near dc, the current is uniformly distributed throughout the cross sections of conductors, and the resistance matrix, which is diagonal, is obtained by taking the inverse of the product of the conductivity and the cross-sectional area of each conductor. In this section, we will focus on the computation of the resistance matrix in the high-frequency region where the skin effect is prominent, and the transverse current distribution is approximately the same as that for a perfect conductor case.

At this high-frequency region, the transverse current distribution on lossy conductors is no longer uniform due to the edge and the proximity effects [16], [17], and the longitudinal voltage drop due to the surface resistivities of the conductors becomes a function of position in the transverse plane. This nonuniform voltage drop cannot be characterized by the resistance matrix; hence, the effect of the finite conductivities of conductors is rather complicated in the high-frequency region in contrast to the effect of the finite loss tangents of the dielectric media, which was readily modeled with the conductance matrix \mathbf{G} based on the shunt current. However, if one is only interested in modeling the power loss on conductors, the resistance matrix \mathbf{R} can still be used to characterize the conductor power loss per unit length, and is computed either from the conductor power loss or from attenuation constants, which, in turn, are obtained from the power loss on conductors [10], [11]. Modeling the power loss with the resistance matrix results in the effective longitudinal voltage drop, which gives the correct power loss per unit length and is uniform over the transverse plane

Unfortunately, the power loss on the conductor is not only dependent on the magnitude of the current but is also a function of the current distribution on the surface of the conductor; therefore, the resistance matrix is also affected by the current distributions employed to compute it. Furthermore, although the current distribution for a single transmission line is not affected by excitations except for scaling of the magnitude, it becomes strongly dependent on the types of excitations for coupled transmission lines [11]. Hence, it follows that the resistance matrix, in general, is dependent on excitations for multiconductor systems. Because of this undesirable dependency, the resistance matrix may not be computed unless the current distribution has been determined. In this section, the nondiagonal resistance matrix is first considered to illustrate this dependency; then, the

diagonal resistance matrix, which is relatively insensitive to the choice of excitations, is proposed.

To simplify the analysis, let us assume that there is only one ground plane at the bottom of the dielectric layers and that the ground plane is perfectly conducting. Then, let us define the resistance matrix \mathbf{R}_1 such that it gives the correct power losses on each conductor as follows:

$$\mathbf{R}_1 \bar{I}_i^c = \bar{V}_i^{eff} \quad i = 1, 2, \dots, N \quad (3.34)$$

where \bar{I}_i^c 's are N independent conduction current vectors, the j th element of \bar{I}_i^c is given by

$$[\bar{I}_i^c]_j = \oint_{c_j} J_i^c(\rho') d\rho' \quad (3.35)$$

and \bar{V}_i^{eff} 's are the line voltage vectors, which represent the effective voltage drops, and are computed from the power loss due to the conduction current vectors \bar{I}_i^c 's. The j th element of \bar{V}_i^{eff} is

$$[\bar{V}_i^{eff}]_j = \frac{P_{i,j}}{[\bar{I}_i^c]_j} = \frac{1}{[\bar{I}_i^c]_j} \oint_{c_j} R_{s,j} [J_i^c(\rho')]^2 d\rho' \quad (3.36)$$

where $P_{i,j}$ is a power loss on the j th conductor, and $R_{s,j}$ is the surface resistivity [17] of the j th conductor given by

$$R_{s,j} = \sqrt{\frac{\pi f \mu}{\sigma_j}} = \frac{1}{\sigma_j \delta_j} \quad (3.37)$$

Here, δ is the skin depth. The above equation is valid when the thickness of a conductor is at least two skin depths thick, and it is assumed in this section that (3.37) is valid for the frequency of interest.

Now the resistance matrix can be readily obtained once the conduction surface current densities $J_i^c(\rho)$, which result in N independent conduction current vectors, are determined. In the high-frequency region where the skin effect is prominent, the surface current density $J_i^c(\rho)$ on good conductors is close to that for perfect conductors. Moreover, as discussed in Section 3.3, the surface current density on perfect conductors

can be obtained by solving the equivalent electrostatic problem, which is constructed by replacing all dielectric media with free space. Hence, $J_i^c(\rho)$ can be computed using (3.20). This approximation of $J_i^c(\rho)$ with the current density for a perfect conductor case is also valid for cases where losses are not relatively large but they are mostly due to the small cross sections of conductors instead of the small values of finite conductivities [18].

Equation (3.34) is applied to compute the resistance matrix for the coupled microstrip lines shown in Fig. 3.12. The conductivity of both microstrip lines is 57.6 MS/m, and the ground plane is assumed to be perfectly conducting. The method described in Section 3.2 is used to solve the equivalent electrostatic problem, and forty pulse basis functions per each line are used to represent the charge distribution. The computed values of \mathbf{R}_1 at a frequency of 1 MHz with various excitations are shown in Table 3.7. The first column shows the excitation voltage used in the equivalent electrostatic problem, and the second column shows the resulting excitation currents. The third to sixth columns correspond to the computed values of \mathbf{R}_1 based on (3.34). All elements of \mathbf{R}_1 varied as the excitation vectors are changed except for the case in which the two excitation vectors are simply scaled (see first and second rows); the variation is especially prominent for the off-diagonal elements of \mathbf{R}_1 , which changed from negative to positive when different excitations were used.

As observed from Table 3.7, the diagonal elements of the resistance matrix are somewhat less sensitive to the choice of current excitations than the off-diagonal elements. Hence, it may be natural to define the resistance matrix as a diagonal matrix, as it is for a dc case, such that the resistance matrix becomes less dependent on the choice of excitations. To obtain the diagonal resistance matrix, let us define the resistance matrix by matching the total power loss on the multiconductor system rather than by matching the power losses on each conductor:

$$\bar{I}_i^c \mathbf{R}_2 \bar{I}_i^c = P_i \quad i = 1, 2, \dots, N \quad (3.38)$$

where \mathbf{R}_2 is assumed to be a diagonal matrix, $(\bar{I}_i^c)^T$ is the transpose of \bar{I}_i^c , and P_i is the total power loss on the system due to the current vector \bar{I}_i^c , obtained by

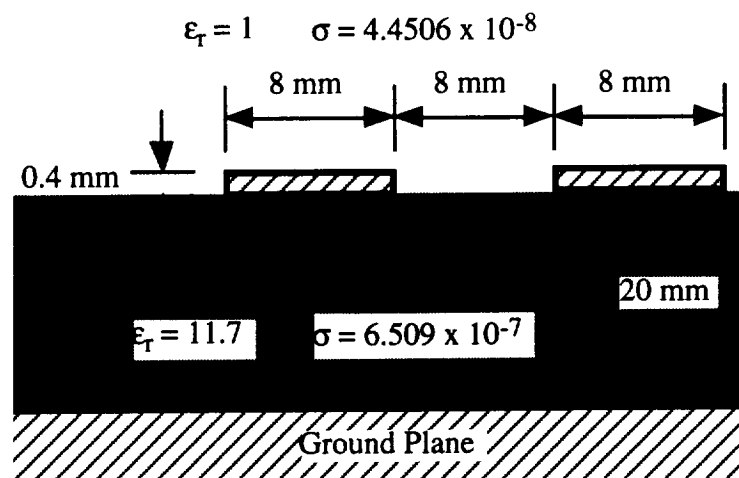


Figure 3.12. Coupled microstrip lines.

Table 3.7. The resistance matrix \mathbf{R} of the coupled microstrip lines shown in Fig. 3.12 with various excitations.

Excitation		\mathbf{R} (nondiagonal) ($\mu\Omega/\text{m}$)				\mathbf{R} (diagonal) ($\mu\Omega/\text{m}$)	
Voltage	Current	R_{11}	R_{12}	R_{21}	R_{22}	R_{11}	R_{22}
(1, 0) (0, 1)	(2.00e9, -7.21e8) (-7.21e8, 2.00e9)	23.65	-5.439	-5.439	23.65	27.13	27.13
(5, 0) (0, 2)	(9.99e9, -3.60e9) (-1.44e9, 4.00e9)	23.65	-5.439	-5.439	23.65	27.13	27.13
(1, 1) (1, -1)	(1.28e9, 1.28e9) (2.72e9, -2.72e9)	26.38	-1.176	-1.176	26.38	•	•
(1, 1) (1, 2)	(1.28e9, 1.28e9) (5.56e8, 3.27e9)	17.00	8.200	0.416	24.78	24.37	26.03
(1, 0) (1, 2)	(2.00e9, -7.21e8) (5.56e8, 3.27e9)	27.91	6.347	-4.717	25.66	27.28	25.95

$$P_i = \sum_{j=1}^N \oint_{c_j} R_{s,j} [J_i^c(\rho')]^2 d\rho' \quad (3.39)$$

where N is the number of signal conductors in the system. Now, noting that \mathbf{R}_2 is a diagonal matrix, (3.38) can be put into the following matrix form:

$$\mathbf{Z}\vec{R} = \vec{P} \quad (3.40)$$

Here, the i th element of the vector \vec{P} is P_i , and \vec{R} is a vector which consists of the diagonal elements of \mathbf{R}_2 . The ij th element of \mathbf{Z} is a square of $I_{i,j}^c$, where $I_{i,j}^c$ is the j th component of \vec{I}_i^c . The diagonal resistance matrix can be obtained by solving the above system of linear equations. Note that N independent conduction current vectors of \vec{I}_i^c no longer guarantee the matrix \mathbf{Z} to be nonsingular. One simple way to obtain N current vectors, which result in a nonsingular \mathbf{Z} matrix, is to excite the voltage only at one conductor at a time in the equivalent electrostatic problem as shown in the first row in Table 3.7. This choice of excitation vectors is shown to result in a more stable resistance matrix as shown in the next numerical example.

To examine the variation of the diagonal resistance matrix for the different choices of excitation vectors, the previous microstrip lines are considered again, and the computed results are shown in Table 3.7. As discussed in the previous paragraph, when the voltage excitations of (1, 1) and (1, -1) are used, \mathbf{Z} becomes a singular matrix; the diagonal resistance matrix could not be determined for this case. As the resistance matrix is defined to be a diagonal matrix, the nondiagonal elements, which are strongly affected by the choice of excitation vectors, no longer cause any problem in the diagonal resistance matrix. Furthermore, as shown in Table 3.7, the diagonal elements of the diagonal resistance matrix are also less dependent on the choice of excitation vectors than the diagonal elements of the nondiagonal resistance matrix. The best choice of excitation vectors appears to be the first two rows in Table 3.7 since the two elements of the resistance matrix are identical as expected from the symmetry of the system.

In practice, the excitations of the resistance matrix based on (3.34) should be chosen so that the resulting resistance matrix is a symmetric matrix to preserve the reciprocity principle. Being a diagonal matrix, reciprocity is naturally satisfied for the resistance matrix based on (3.38). In general, the Maxwellian resistance matrix calculated

from (3.34), (3.38), or the perturbational analysis on attenuation constants is related to the physical self- and mutual resistances by

$$R_{i,j} = R_{i,j}^m \quad (3.41a)$$

$$R_{i,i} = R^s \quad (3.41b)$$

3.5.2. Losses due to imperfectly conducting ground planes

To account for losses due to imperfectly conducting ground planes, the surface current distribution on the ground planes must be determined for the given current excitation on the signal lines. In general, an integral equation has to be formulated to compute the surface current density on the ground planes, and a detailed discussion of the determination of the current densities on ground planes is presented in this section.

Let us first assume that a multilayered dielectric medium is backed by two ground planes below and above the layers, as shown in Fig. 3.13. Let $J(x,y)$, $J^{s,1}(x)$, and $J^{s,2}(x)$ be the current densities on the surfaces of the signal lines, the bottom ground plane, and the top ground plane, respectively. Then, assume that the surface current density on the signal lines $J(x,y)$ is given by

$$J(x,y) = \sum_{k=1}^{N_t} J_k P_k(x,y) \quad (3.42)$$

where $P_k(x,y)$ is an appropriate pulse basis function used to expand the current density on the surface of signal conductors, and N_t is the total number of basis functions used to discretize the contours of the conductors. Then, the tangential magnetic field $H_t(x)$ at the bottom ground plane due to $J(x,y)$ and $J^{s,2}(x)$ at the bottom ground plane can be written as (see Fig. 3.13)

$$H_t(x) = \frac{1}{2\pi} \sum_{k=1}^{N_t} \frac{J_k l_k y_k}{(x-x_k)^2 + y_k^2} + \frac{1}{2\pi} \int_{-\infty}^{+\infty} \frac{J^{s,2}(x') h}{(x-x')^2 + h^2} dx' \quad (3.43)$$

Since the tangential magnetic field due to all the image currents of $J(x,y)$ and $J^{s,2}(x)$ must also be equal to $H_t(x)$ at the bottom ground plane, the total tangential magnetic field at the bottom ground plane must be twice that of $H_t(x)$. Since the negative value of this total

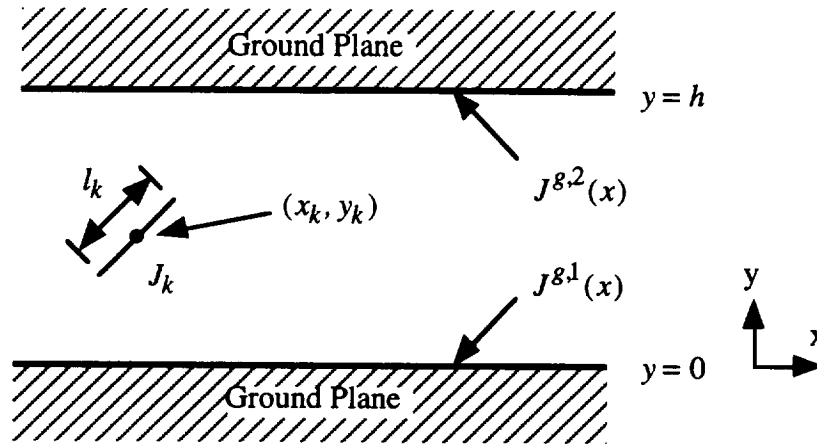


Figure 3.13. The k th segment of conductor contours between the two ground planes.

tangential magnetic field is equal to the actual surface current density $J^g,1(x)$, the following integral equation can be formulated:

$$J^g,1(x) + \frac{1}{\pi} \int_{-\infty}^{+\infty} \frac{J^g,2(x')h}{(x-x')^2 + h^2} dx' = -\frac{1}{\pi} \sum_{k=1}^{N_t} \frac{J_k l_k y_k}{(x-x_k)^2 + y_k^2} \quad (3.44)$$

A similar argument holds for the tangential magnetic field at the top ground plane, and the resulting integral equation is

$$J^g,2(x) + \frac{1}{\pi} \int_{-\infty}^{+\infty} \frac{J^g,1(x')h}{(x-x')^2 + h^2} dx' = -\frac{1}{\pi} \sum_{k=1}^{N_t} \frac{J_k l_k (h-y_k)}{(x-x_k)^2 + (h-y_k)^2} \quad (3.45)$$

Now, truncating the ground planes to finite lengths and expanding $J^g,1(x)$ and $J^g,2(x)$ using the pulse basis functions,² (3.44) and (3.45) can be put into the following form:

$$\begin{bmatrix} \mathbf{I} & \mathbf{M}_{12} \\ \mathbf{M}_{21} & \mathbf{I} \end{bmatrix} \begin{bmatrix} \mathbf{J}^g,1 \\ \mathbf{J}^g,2 \end{bmatrix} = \begin{bmatrix} \mathbf{V}_1 \\ \mathbf{V}_2 \end{bmatrix} \quad (3.46)$$

²This truncation is possible since the actual current is confined near the conductor regions. To achieve good computational efficiency, nonuniform pulse basis functions should be used in the expansion of the current.

where \mathbf{M}_{ij} is an N_{gi} by N_{gj} matrix, $\mathbf{J}^{\mathbf{g},i}$ and \mathbf{V}_i are N_{gi} dimensional vectors, N_{gi} is the number of basis functions used to expand $J^{\mathbf{g},i}(x)$, and \mathbf{I} denotes the identity matrix. The expressions for the elements of the matrices and vectors are given by

$$[\mathbf{M}_{12}]_{i,j} = \frac{1}{\pi} \frac{l_j^{\mathbf{g},2} h}{(x_i^{\mathbf{g},1} - x_j^{\mathbf{g},2})^2 + h^2} \quad [\mathbf{M}_{21}]_{i,j} = \frac{1}{\pi} \frac{l_j^{\mathbf{g},1} h}{(x_i^{\mathbf{g},2} - x_j^{\mathbf{g},1})^2 + h^2} \quad (3.47)$$

$$[\mathbf{V}_1]_i = -\frac{1}{\pi} \sum_{k=1}^{N_t} \frac{J_k l_k y_k}{(x_i^{\mathbf{g},1} - x_k^{\mathbf{s}})^2 + y_k^2} \quad [\mathbf{V}_2]_i = -\frac{1}{\pi} \sum_{k=1}^{N_t} \frac{J_k l_k (h - y_k)}{(x_i^{\mathbf{g},2} - x_k^{\mathbf{s}})^2 + (h - y_k)^2} \quad (3.48)$$

where $l_j^{\mathbf{g},m}$ is the length associated with $J_j^{\mathbf{g},m}$, which is the j th element of $\mathbf{J}^{\mathbf{g},m}$, and x_m and y_m represent the center point of the m th basis function. The superscripts $g, l, g, 2$, and s are attached to x to denote x 's on the bottom and top ground planes and the signal conductors, respectively. Now performing a simple substitution, a computationally more efficient form of (3.46) can be obtained:

$$[\mathbf{I} - \mathbf{M}_{21}\mathbf{M}_{12}]\mathbf{J}^{\mathbf{g},2} = \mathbf{V}_2 - \mathbf{M}_{21}\mathbf{V}_1 \quad (3.49)$$

$$\mathbf{J}^{\mathbf{g},1} = \mathbf{V}_1 - \mathbf{M}_{12}\mathbf{J}^{\mathbf{g},2} \quad (3.50)$$

Now, the current distribution on the ground planes can be obtained by first solving the system of linear equations given by (3.49) for $\mathbf{J}^{\mathbf{g},2}$ and using (3.50) for $\mathbf{J}^{\mathbf{g},1}$.

When there is no top ground plane, (3.46) is simplified to

$$\mathbf{J}^{\mathbf{g},1} = \mathbf{V}_1 \quad (3.51)$$

Note that no solution of a system of linear equations is necessary for this case.

Once the current density on the ground planes has been determined, (3.39) can be modified to include ground losses as follows:

$$P_i = \sum_{j=1}^N \oint_{c_j} R_{s,j} [J_i^c(\rho')]^2 d\rho' + \sum_{j=1}^{N_g} \oint_{c_j} R_{s,j} [J_i^{\mathbf{g},j}(\rho')]^2 d\rho' \quad (3.52)$$

where N_g is the number of ground planes, which is either one or two.

3.5.3 Remarks on the various methods used in the computation of the resistance matrix

In this section, several remarks on the various methods used to compute the resistance matrix are given. Since power losses are nonlinearly dependent on the current distribution for a multilane case, the resistance matrix becomes dependent on the excitations. Thus, if power losses are modeled with the resistance matrix, the resistance matrix cannot be independent of the excitations used in the computation. For a single-line case, the resistance matrices based on (3.34), (3.38) and attenuation constants are all identical, and they model the exact power loss per unit length regardless of excitations. For a multilane case, the nondiagonal resistance matrix defined by (3.34) is only valid for the case in which the actual current distribution belongs to one of the current excitations used in the computation. Similarly, the conventional approach based on the perturbation on attenuation constants [10] uses the modal power losses; therefore, the resulting resistance matrix is only valid for the modal current. However, the currents on the conductors are arbitrary so any current distribution is as important as the modal current distribution. Hence, the nondiagonal matrices based on (3.34) and the conventional approach are inappropriate for the computation of the resistance matrix for a multiconductor case. The diagonal resistance matrix based on (3.38) is shown to be least affected by the choice of current excitations and, hence, is most suitable for the computation of the resistance matrix.

Now let us discuss the accuracy of the various definitions of the resistance matrix. First, the nondiagonal resistance matrix based on (3.34), which, in fact, is included in the chapter only to demonstrate the nonlinear effect, is symmetric for the modal current excitations (the third row in Table 3.7) and more accurate than the one from [10] since it matches the power losses on each conductor instead of matching the total power loss. Thus, (3.34) with the modal excitations can be used to define the unique resistance matrix, and this definition of the resistance matrix is already more accurate than the conventional approach [10]. The diagonal resistance matrix based on (3.38) also models the total power losses for chosen current excitations; therefore, it is as accurate as the one from the conventional approach. Conclusively, if the excitation is fixed as the conventional approach, the resistance matrices based on (3.34) and (3.38) are as accurate as the one from the conventional approach and *unique*. Although the resistance matrix based on (3.38) is less accurate in terms of modeling of power losses than the one based on (3.34) for a fixed excitation, it is more accurate for an arbitrary current distribution because it varies less for different excitations. Similarly, the resistance matrix obtained from the

conventional approach is also nondiagonal and, hence, is less accurate than the diagonal resistance matrix for an arbitrary current distribution.

3.5.4. Numerical examples

In this section, the diagonal resistance matrix for various geometries are computed. Most examples are extracted from [10] for comparison purposes. The thicknesses of the ground planes are assumed to be infinite for all examples. The method described in Section 3.2 is used to solve all electrostatic problems. As a first example, the resistance value of the cylindrical conductor above a PEC ground plane shown in Fig. 3.10 on p. 55 is computed. The computed value was $0.8459 \Omega/\text{m}$ at a frequency of 100 MHz, whereas the closed-form formula (3.33c) was $0.8426 \Omega/\text{m}$. Forty pulse basis functions were used to solve the electrostatic problem in our approach. As the next example, a single microstrip line is considered. The same geometry used in Section 3.5.1 (see Fig. 3.12) is analyzed with only one line. At a frequency of 1 MHz, the computed resistance value was $2.493 \times 10^{-5} \Omega/\text{m}$ without any ground loss and $2.688 \times 10^{-5} \Omega/\text{m}$ with ground loss. The ground plane is assumed to be of the same material as the microstrip line, both materials having $\sigma = 5.76 \times 10^7 \text{ S/m}$. The resistance value from [10] with ground loss was $2.400 \times 10^{-5} \Omega/\text{m}$ after applying the proper scaling factor. The current distribution on the ground plane is shown in Fig. 3.14. The resistance values were also computed for a wide range of frequencies, and the results are plotted in Fig. 3.15.

For the final example, the four-conductor system shown in Fig. 3.11 on p. 56 is considered, and the results are compared in Table 3.8. The current densities on the top and bottom ground planes with the excitation on the first conductor are shown in Figs. 3.16(a) and (b). The resistance matrix shown in Table 3.8 is actually incorrect since (3.37) for the surface resistivity R_s is no longer valid because the thicknesses of the first and third conductors are smaller than the skin depth δ . To obtain an approximate solution, we have defined the effective depth d_{eff} to be either δ or the half thickness of the conductor, whichever is smaller, and the surface resistivity R_s is redefined as

$$R_s(\rho) = \frac{1}{\sigma d_{eff}(\rho)} \quad (3.53)$$

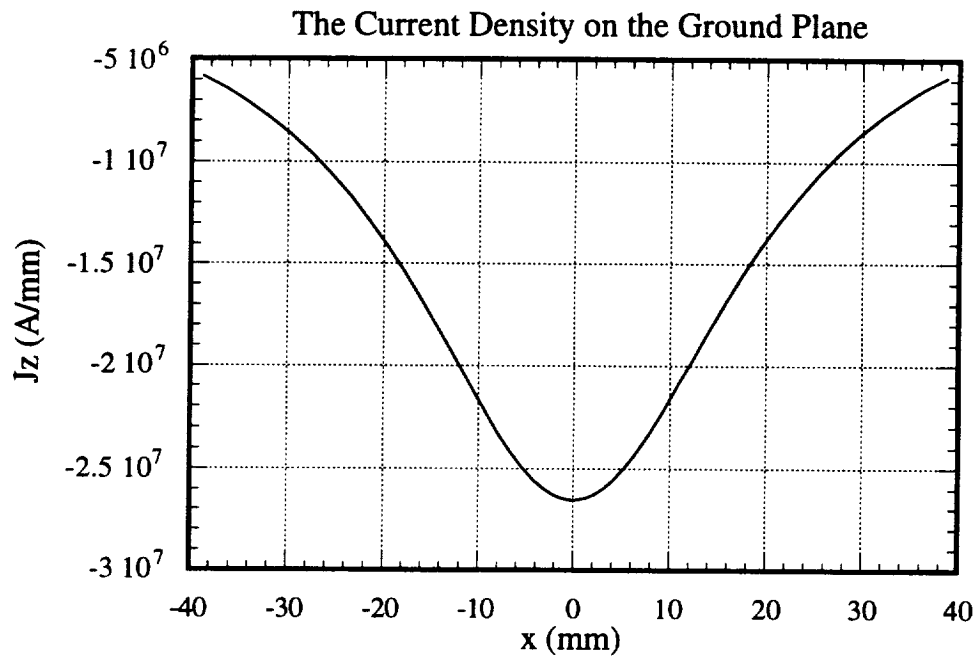


Figure 3.14. The current density on the ground plane for a single microstrip case.

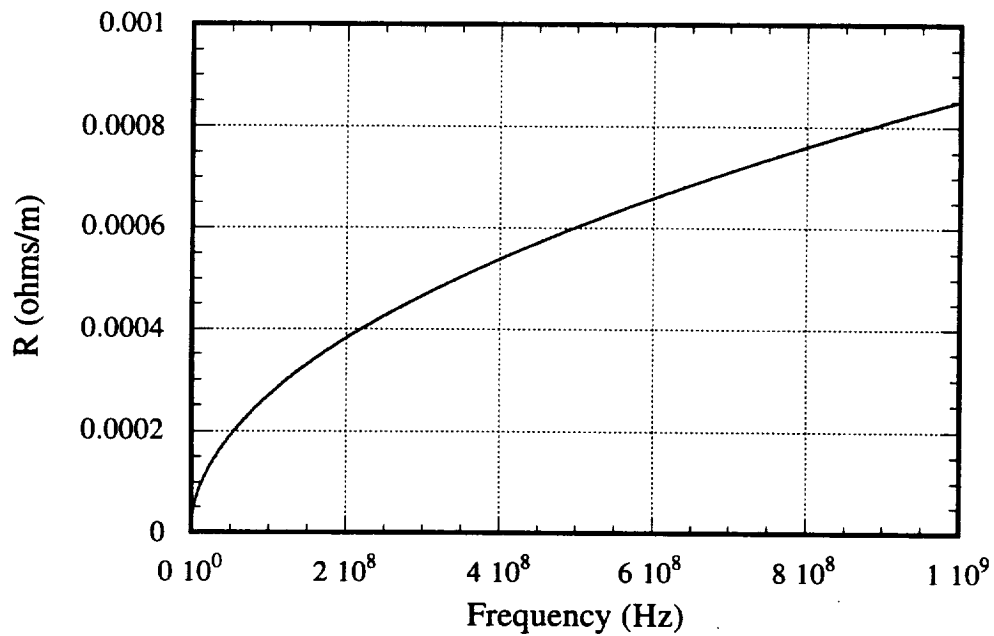


Figure 3.15. The resistance vs. frequency for a single microstrip line with ground losses.

Table 3.8. The resistance matrix for the four-conductor system shown in Fig. 3.11.

i	j	$[R]_{ij}$ ($\mu\Omega/m$)	
		Presented	[10]
1	1	1094	737.5
1	2	0	85.18
1	3	0	44.03
1	4	0	60.33
2	2	763.0	680.1
2	3	0	87.58
2	4	0	140.1
3	3	1015	671.1
3	4	0	160.4
4	4	508.7	690.1

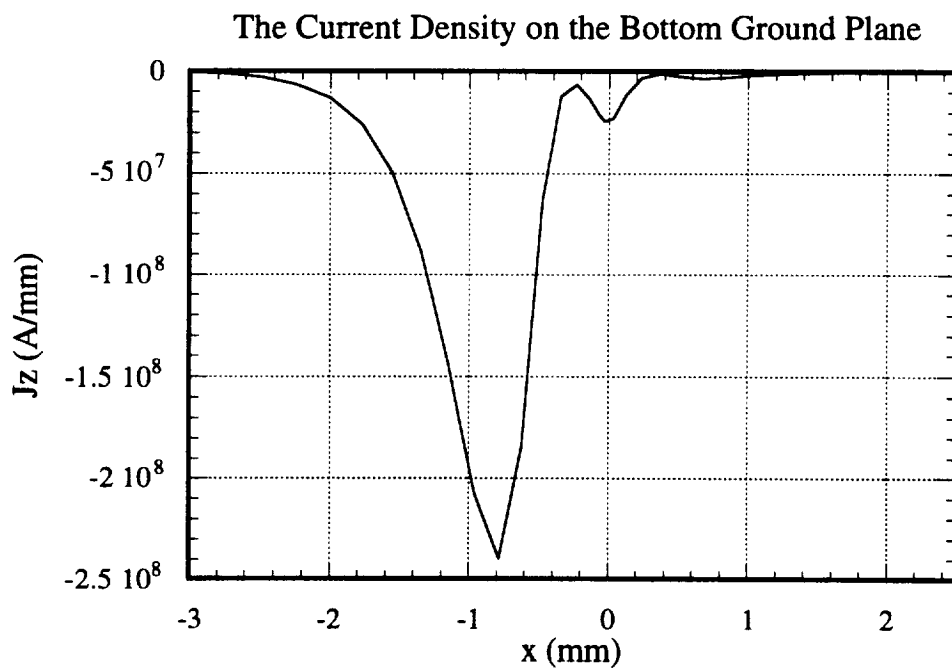
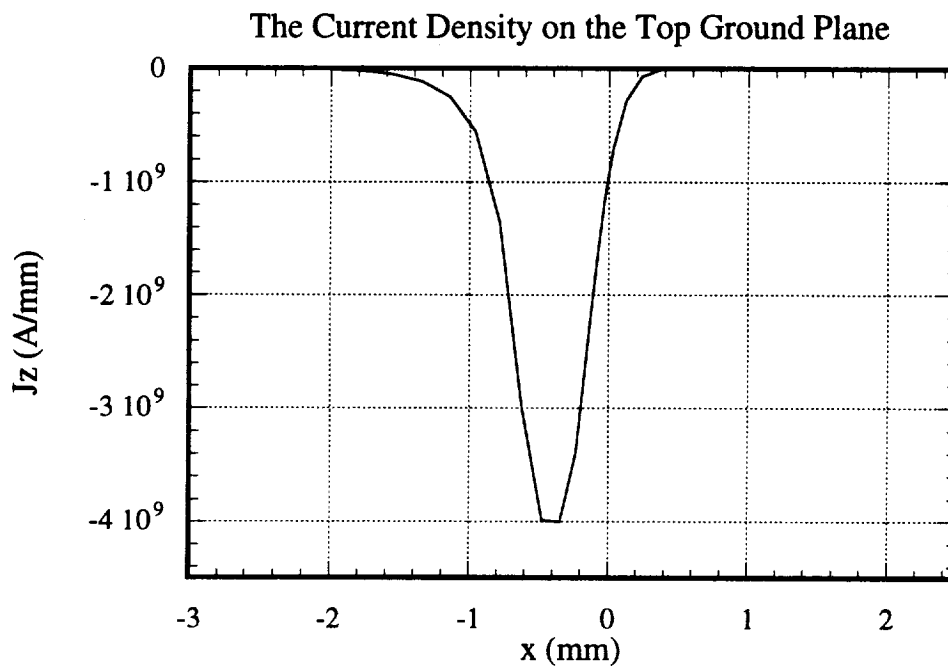


Figure 3.16. The current densities on (a) the top and (b) the bottom ground planes for four-conductor system with the excitation on the first conductor.

The half thickness of the conductor is used since the surface current exists on both sides of the conductor. Note that the effective thickness d_{eff} is a function of ρ since the thickness of a conductor, in general, changes as ρ varies. The resistance matrix \mathbf{R} for the previous case is computed again using the above formula, and the following result shows that the resistance value is substantially increased:

$$\mathbf{R} (\mu\Omega/m) = \begin{bmatrix} 4688 & 0 & 0 & 0 \\ 0 & 836.9 & 0 & 0 \\ 0 & 0 & 2539 & 0 \\ 0 & 0 & 0 & 598.4 \end{bmatrix}$$

3.6. Summary

Accurate and efficient ways to compute the transmission line parameters of a multiconductor system embedded in a multilayered dielectric medium were presented in this chapter. The capacitance matrix was computed based on the closed-form Green's function discussed in the previous chapter; thus, no numerical integrations or nested infinite summations are involved in the computation. The inductance matrix is calculated by solving the equivalent capacitance problem. The solutions (charge distributions) obtained from the computations of the capacitance matrix and the inductance matrix were directly used to compute the resistance and conductance matrices, rather than by using the usual perturbation analysis on the modal power. Hence, no additional electrostatic problem was solved for the computations of the resistance and conductance matrices. The diagonal resistance matrix was proposed in this chapter; this diagonal matrix has been shown to be relatively insensitive to the choice of the current excitations as opposed to the sensitivity of the traditional nondiagonal resistance matrix. Hence, it is more suitable for the computation of the resistance matrix. In addition to losses on signal conductors, those due to imperfectly conducting ground planes were also incorporated into the resistance matrix.

3.7. References

- [1] C. Wei, R. F. Harrington, J. R. Mautz, and T. K. Sarkar, "Multiconductor transmission lines in multilayered dielectric media," *IEEE Trans. Microwave Theory Tech.*, vol. 32, pp. 439-450, April 1984.
- [2] W. T. Weeks, "Calculation of coefficients of capacitance of multiconductor transmission lines in the presence of a dielectric interface," *IEEE Trans. Microwave Theory Tech.*, vol. 18, pp. 35-43, January 1970.

- [3] G. W. Pan, G. Wang, and B. K. Gilbert, "Edge effect enforced boundary element analysis of multilayered transmission lines," *IEEE Trans. Circuits Syst.*, vol. 39, pp. 955-963, November 1992.
- [4] W. Delbore and D. D. Zutter, "Space-domain Green's function approach to the capacitance calculation of multiconductor lines in multilayered dielectrics with improved surface charge modeling," *IEEE Trans. Microwave Theory Tech.*, vol. 37, pp. 1562-1568, October 1989.
- [5] E. Yamashita, "Variational method for the analysis of microstrip-like transmission lines," *IEEE Trans. Microwave Theory Tech.*, vol. 16, pp. 529-535, May 1964.
- [6] H. A. Wheeler, "Transmission line properties of parallel wide strips by a conformal mapping approximation," *IEEE Trans. Microwave Theory Tech.*, vol. 12, pp. 280-289, May 1964.
- [7] J. Svacina, "Analysis of multilayer microstrip lines by a conformal mapping method," *IEEE Trans. Microwave Theory Tech.*, vol. 40, pp. 769-772, April 1992.
- [8] W. E. Matzke, B. Heinemann, and Telschow, "On the calculation of the capacitance coefficients for VLSI multilevel metallization lines by using domain methods," *IEEE Trans. Electron. Devices*, vol. 36, pp. 447-449, February 1989.
- [9] Z-H. Zhu, W. Hong, Y. Chen, Y. Wang, and J. Tao, "Electromagnetic modeling and transient simulation of interconnects in high speed VLSI," *IEEE Multi-Chip Module Conf.*, pp. 93-98, 1995.
- [10] R. F. Harrington and C. Wei, "Losses on multiconductor transmission lines in multilayered dielectric media," *IEEE Trans. Microwave Theory Tech.*, vol. 32, pp. 705-710, July 1984.
- [11] S. Frankel, *Multiconductor Transmission Line Analysis*. Dedham, MA: Artech House, 1977.
- [12] R. A. Pucel, D. J. Masse, and C. P. Hartwig, "Losses in microstrip," *IEEE Trans. Microwave Theory Tech.*, vol. 16, pp. 342-350, June 1968.
- [13] C. H. Chan and R. Mittra, "Analysis of MMIC structures using an efficient iterative approach," *IEEE Trans. Microwave Theory Tech.*, vol. 36, pp. 96-105, January 1988.
- [14] P. H. Harms, C. H. Chan, and R. Mittra, "Modeling of planar transmission line structures for digital circuit applications," *AEU (Archiv fur Elektronik und Ubertragungstechnik)*, Band 43, pp. 245-250, 1989.
- [15] M. Horno, R. L. Mesa, F. Medina, and R. Marques, "Quasi-TEM analysis of multilayered multiconductor coplanar structures with dielectric and magnetic anisotropy including substrate losses," *IEEE Trans. Microwave Theory Tech.*, vol. 38, pp. 1059-1068, August 1990.

- [16] A. R. Djordjević and T. K. Sarkar, "Closed-form formulas for frequency-dependent resistance and inductance per unit length of microstrip and strip transmission lines," *IEEE Trans. Microwave Theory Tech.*, vol. 42, pp. 241-248, February 1994.
- [17] S. Ramo, J. R. Whinnery, and T. Van. Duzer, *Fields and Waves in Communication Electronics*, 2nd ed. New York: Wiley, 1984.
- [18] G. L. Matthaei, K. Kiziloglu, N. Dagi, and S. I. Long, "The nature of the charges, currents, and fields in and about conductors having cross-sectional dimensions of the order of a skin depth," *IEEE Trans. Microwave Theory Tech.*, vol. 38, pp. 1031-1036, August 1990.

CHAPTER 4

COMPUTATION OF THE EQUIVALENT CAPACITANCES OF VARIOUS STRIP DISCONTINUITIES: AN OPEN END, A BEND, AND VARIOUS JUNCTIONS

4.1 Introduction

Quasi-static analysis is often performed to characterize strip discontinuities, such as an open end, a bend, a T junction, and a cross junction, when the dimensions of the discontinuities are much smaller than the wavelength. A brief introduction of the quasi-static approximation was presented in Section 1.2. Under this quasi-static analysis, the dominant effect of strip discontinuities is fringing fields due to the physical irregularities of discontinuity geometries, and the modeling of these fringing fields in terms of an equivalent (excess) capacitance is discussed in this chapter.

Numerous papers have been published to compute the excess capacitances of various microstrip discontinuities, and a summary of popular methods can be found in [1], [2]. The usual approach involves finding the charge distributions in the presence of a discontinuity and in the absence of a discontinuity. Total charges are then obtained from these charge distributions, and the excess capacitance is computed by subtracting these total charges. This approach is referred to as the total charge formulation in this thesis, and it is widely known to be inaccurate due to the numerical error associated with the subtraction of the total charges due to reasons explained in [1]-[3]. Since the discontinuity effects are rather localized, the total excess charge distribution of the discontinuity system is often much smaller than the total charge. Hence, the total charges of the system with and without the discontinuity are nearly equal, and the errors associated with these two total charges are relatively very large compared to the total excess charge, which results in the equivalent capacitance. Moreover, the total charge formulation is also computationally expensive for the following two reasons. First, two problems must be solved for one with a discontinuity and one without a discontinuity. Second, discontinuities are associated with semi-infinite lines, and after truncating these lines to finite lengths, the unknowns associated with the total charge distribution must be placed over the whole surface of the truncated lines although the excess charge is localized around the discontinuities.

The formulation of an integral equation in terms of the excess charge distribution, first proposed by Silvester and Benedek [3], has been applied to analyze various microstrip

discontinuities [3]-[6]. This approach overcomes the previously discussed numerical problems associated with the total charge formulation since the excess charge distribution is directly modeled as an unknown in an integral equation; in other words, the accuracy resulting from solving an integral equation is preserved for the final answer. This approach is referred as the excess charge formulation throughout this thesis. The Green's function for a layered medium is employed in this approach. For N dielectric layers, the expression for this Green's function would consist of an $N-1$ nested infinite series [7]; hence, in practice, this form of the Green's function may not be applied to a multilayered medium¹. Recently, Sarkar et al. [8] solved the discontinuity problems for a multilayered medium using the free-space Green's function, but additional unknown charges (over unknown charges on the surface of a conductor) had to be placed on the dielectric interfaces and the top ground plane to model the polarization charge and the free charge. Although the inclusion of these additional unknowns may be tolerable for 2-D problems, it is computationally too burdensome for 3-D problems.

In this chapter, the closed-form Green's function discussed in Chapter 2 is employed to formulate an integral equation in terms of the excess charge distribution; thus, the presented method requires neither additional unknowns to model dielectric interfaces and the top ground plane nor evaluations of any infinite series except for cases where the top ground plane is present. When the top ground plane is present, using the closed-form Green's function is still numerically advantageous since the nested infinite series in the expression of the usual Green's function become a simple infinite series without nesting. Although it is possible to avoid infinite series even for cases where the top ground plane is present by modeling it as an additional conductor,² it substantially increases the number of unknowns; hence, it is not considered in this chapter.

In Section 4.2, the general description of discontinuity structures is discussed, and the general representation of strip discontinuities, from which most of common discontinuity types can be derived, is presented. In Section 4.3, the closed-form Green's function is employed to formulate an integral equation to determine the excess charge distribution of the generalized discontinuity structure given in Section 4.2; thus, only one

¹See also Section 2.2 for more detailed discussion of this Green's function.

²This approach is used in Chapter 6 for the computation of the equivalent capacitance of a strip crossover.

integral equation is formulated for various types of discontinuities, unlike other approaches given in [3]-[6], in which a different integral equation has been formulated for each discontinuity type. Then, the method of moments is employed to solve the integral equation. The equivalent capacitances of an open end, a step junction, a bend, and a T junction are considered as numerical examples, and the computed capacitances are compared with other published results in Section 4.4.

4.2 General Statement of the Problem

The planar view of the general geometry of a discontinuity considered in this chapter is shown in Fig. 4.1. A discontinuity, in general, consists of an arbitrary number N_t of traces, which are all connected either with or without a junction region. This general geometry represents most of the common strip discontinuities, e.g., an open end, a nonorthogonal bend, and various junctions. Although the present approach can handle conductors with finite thicknesses, the conductor thicknesses are assumed to be infinitely thin in this chapter.

The discontinuity structure is embedded in a layered dielectric medium, which is shown in Fig. 4.2. An arbitrary number of dielectric layers are located on top of a ground plane, and the layered dielectric medium is terminated by an optional ground plane on the other side. Unlike the dielectric medium considered in Chapter 2 (see Fig. 2.1), it is assumed that the bottom ground plane always exists.

Some common strip discontinuities which can be represented with the general discontinuity geometry shown in Fig. 4.1 are depicted in Fig. 4.3 with their equivalent circuit representations. These representations include transmission lines; hence, they assume that there is at least one ground plane. In general, the equivalent inductances should be added in these equivalent circuit representations, and they can be computed using the method described in [7].

4.3 Formulation of an Integral Equation

The integral equation relating the electrostatic potential $\phi(r)$ and the charge density $q(r)$ on the surface of a conductor for 3-D problems is given by

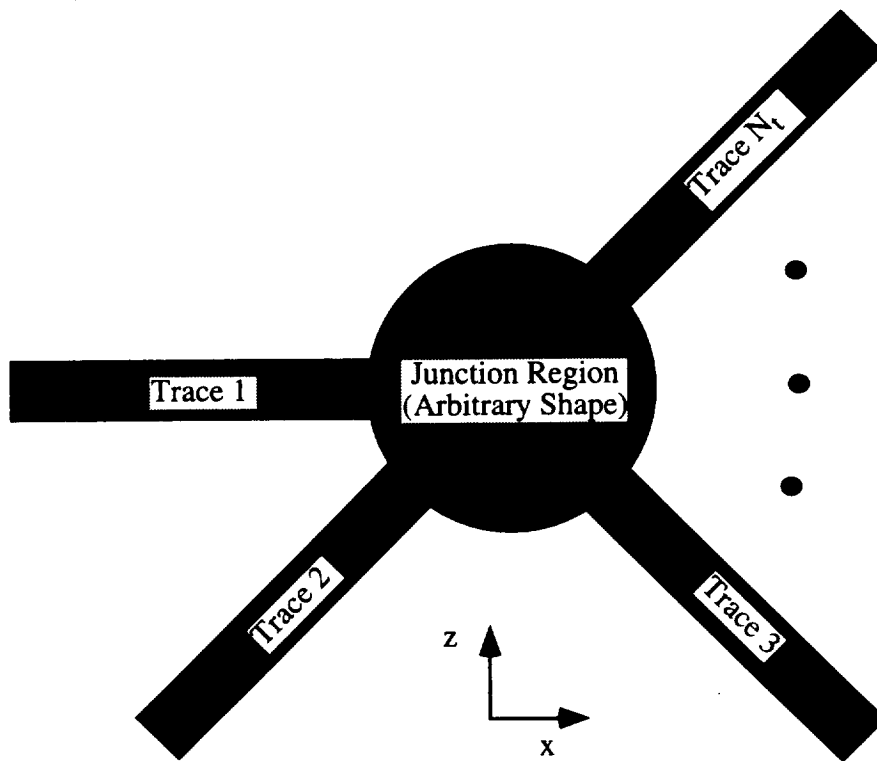


Figure 4.1. General geometry of a strip discontinuity.

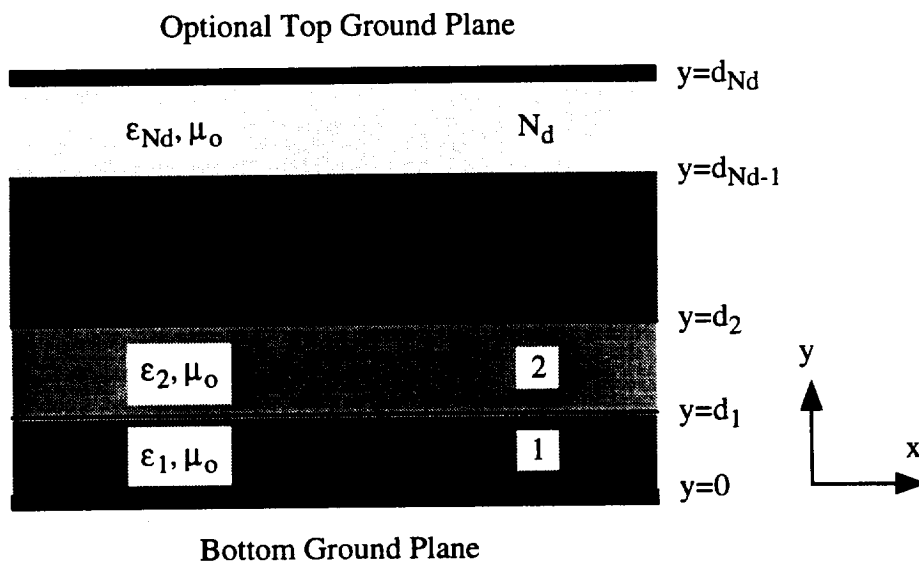
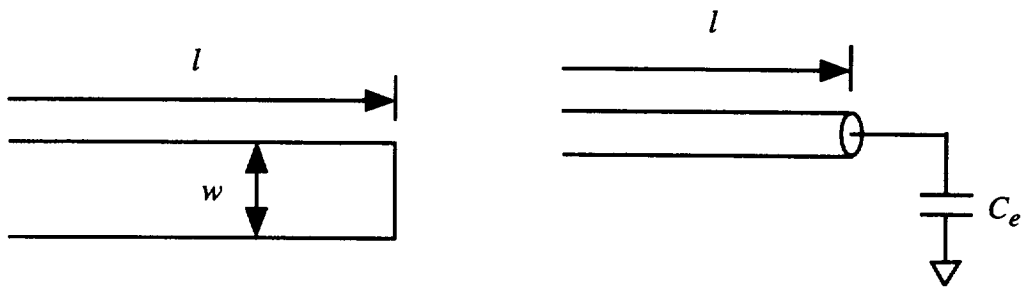
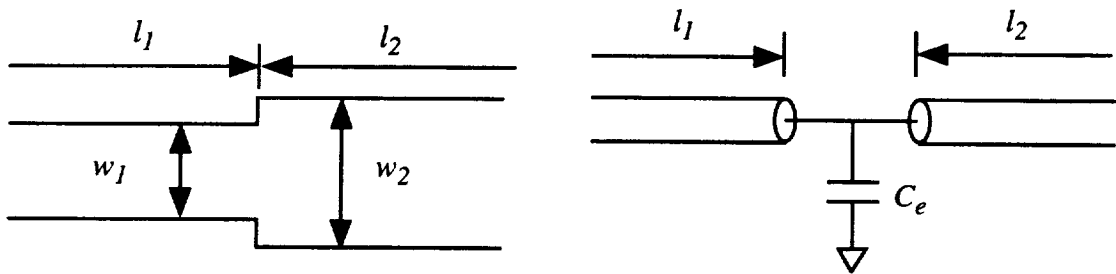


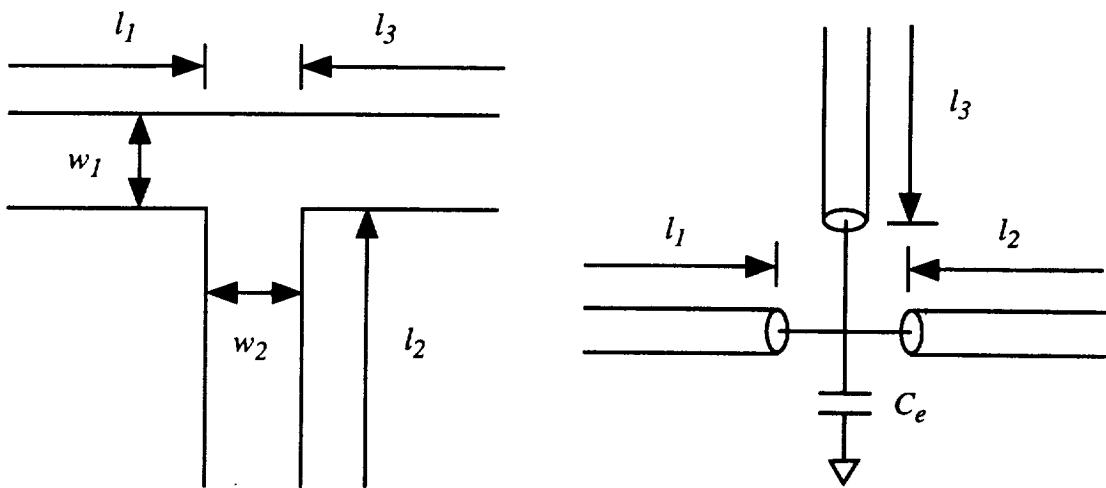
Figure 4.2. Cross-sectional view of a multilayered dielectric medium.



(a) An open end

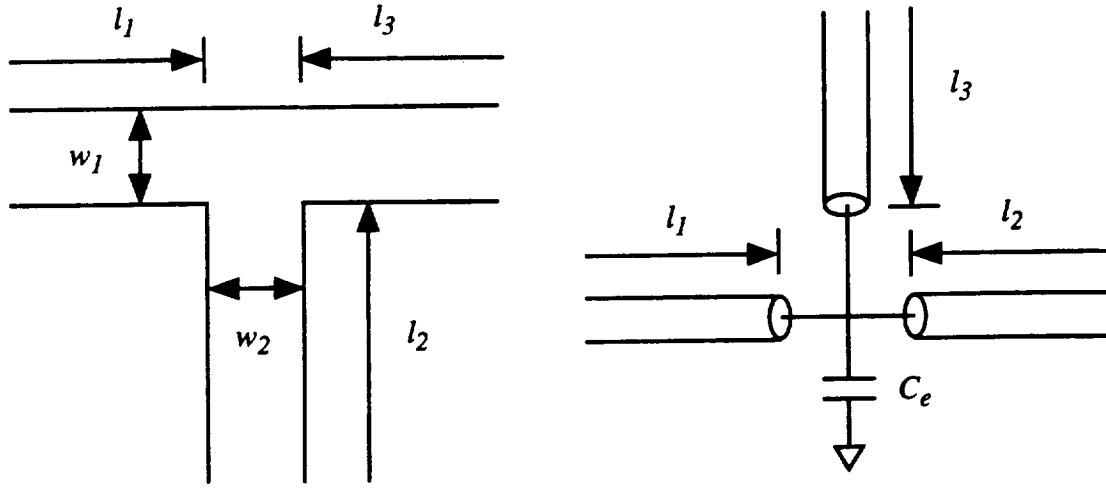


(b) A step junction



(c) A bend

Figure 4.3. Discontinuities and their equivalent circuit representations.



(d) A T junction

Figure 4.3. Continued.

$$\phi(r) = \int_{\Omega} G^{3D}(r|r')q(r')dr' = \langle G^{3D}, q \rangle \quad (4.1)$$

where the Ω 's are the surfaces of conductors: traces and a junction region. $G^{3D}(r|r')$ is the 3-D closed-form Green's function for a layered medium, which accounts for the polarization charges and free charge on ground planes. To simplify the notation the integration is symbolically written as $\langle \cdot, \cdot \rangle$. Now let us rewrite the charge density $q(r)$ in the following manner:

$$q(r) = \begin{cases} q_J(r), & \text{if } r \text{ is on the junction region} \\ q_T^i(r), & \text{if } r \text{ is on the } i\text{th trace} \end{cases} \quad (4.2)$$

and, for each trace, let us decompose the charge densities $q_T^i(r)$ into the uniform charge density $q_T^{unif,i}(r)$ and the excess charge density $q_T^{excess,i}(r)$:

$$q_T^i(r) = q_T^{unif,i}(r) + q_T^{excess,i}(r) \quad (4.3)$$

Here, the uniform charge density $q_T^{unif,i}(r)$ is obtained by solving a 2-D problem, in which it is assumed that only the i th trace is present in the medium and that the i th trace is infinitely long in both directions. A detailed discussion for solving 2-D problems was given in Section 3.2.1. The uniform charge density $q_T^{unif,i}(r)$ exists only on the i th trace,

which is a semi-infinite line; hence, $G^{semi}(r|r_o, \xi)$ should be used to compute the potential due to $q_T^{unif,i}(r)$.

Using (4.2), the integral equation (4.1) can be written as follows:

$$\phi(r) = \langle G^{3D}, q \rangle = \langle G^{3D}, q_J \rangle + \sum_{i=1}^{N_t} \langle G^{3D}, q_T^i \rangle \quad (4.4)$$

Now using (4.3), the above equation is rewritten as

$$\phi(r) - \sum_{i=1}^{N_t} \langle G^{semi}, q_T^{unif,i} \rangle = \langle G^{3D}, q_J \rangle + \sum_{i=1}^{N_t} \langle G^{3D}, q_T^{excess,i} \rangle \quad (4.5)$$

A complete list of expressions of the closed-form Green's functions for a point charge, a line charge, and a semi-infinite line charge with or without a top ground plane is given in Section 2.3. It should be noted that all quantities in the left-hand side of (4.5) are known assuming 2-D problems have been solved a priori.

Now applying the method of collocation with the excitation voltage ϕ_o , the above integral equation yields the following system of linear equations:

$$\begin{bmatrix} \phi_o \\ \cdot \\ \cdot \\ \cdot \\ \phi_o \end{bmatrix} - \begin{bmatrix} V_1 \\ \cdot \\ \cdot \\ \cdot \\ V_{N_t+1} \end{bmatrix} \begin{bmatrix} q_T^{unif,1} \\ \cdot \\ \cdot \\ \cdot \\ q_T^{unif,N_t} \end{bmatrix} = \begin{bmatrix} M_{1,1} & \cdot & \cdot & M_{1,N_t+1} \\ \cdot & \cdot & \cdot & \cdot \\ \cdot & \cdot & \cdot & \cdot \\ \cdot & \cdot & \cdot & \cdot \\ M_{N_t+1,1} & \cdot & \cdot & M_{N_t+1,N_t+1} \end{bmatrix} \begin{bmatrix} q_J \\ q_T^{excess,1} \\ \cdot \\ \cdot \\ q_T^{excess,N_t} \end{bmatrix} \quad (4.6)$$

where

$$[M_{i,j}]_{p,q} = \iint_{S_q} G^{3D}(r_p|r') ds' \quad (4.7a)$$

$$[V_i]_{p,q} = \int_{C_q} G^{semi}(r_p|r', \xi) dl' \quad (4.7b)$$

$$\mathbf{q}_T^{\text{excess},i} = \left[q_{T,1}^{\text{excess},i}, q_{T,2}^{\text{excess},i}, \dots, q_{T,N_{3D,i}}^{\text{excess},i} \right]^T \quad (4.7c)$$

$$\mathbf{q}_J = \left[q_{J,1}, q_{J,2}, \dots, q_{J,N_J} \right]^T \quad (4.7d)$$

$$\mathbf{q}_T^{\text{unif},i} = \left[q_{T,1}^{\text{unif},i}, q_{T,2}^{\text{unif},i}, \dots, q_{T,N_{2D,i}}^{\text{unif},i} \right]^T \quad (4.7e)$$

Here, S_q and C_q denote the source patch and line segment for 3-D and 2-D problems, and r_p is the observation (testing) point, which is the center of a patch or a line segment. $N_{3D,i}$ and N_J are the total numbers of patches to represent $q_T^{\text{excess},i}(r)$ and $q_J(r)$, respectively, whereas $N_{2D,i}$ is the total number of line segments to represent $q_T^{\text{unif},i}(r)$. It is assumed that ϕ_o is also used as the excitation voltage in 2-D problems. The closed-form integration formulas for (4.7a) and (4.7b) were discussed in Section 2.4. Now given the excitation voltage ϕ_o , the excess charge distribution can be determined by solving the above linear system of equations.

Now once (4.6) is solved, the excess (equivalent) capacitance C^e can be obtained by

$$C^e = \left[Q_J + \sum_{i=1}^{N_T} Q_T^{\text{excess},i} \right] / \phi_o \quad (4.8)$$

where

$$Q_J = \sum_{k=1}^{N_J} q_{J,k} \cdot \text{Area}_{J,k} \quad (4.9a)$$

$$Q_T^{\text{excess},i} = \sum_{k=1}^{N_j} q_{T,k}^{\text{excess},i} \cdot \text{Area}_{T,k}^i \quad (4.9b)$$

Here, $\text{Area}_{J,k}$ and $\text{Area}_{T,k}^i$ are the areas of the k th patches used to represent $q_J(r)$ and $q_T^{\text{excess},i}(r)$, respectively.

Throughout the formulation, we have assumed that the junction region exists between traces. The formulation for cases without the junction region, such as an open end

and step junctions, can be easily obtained by following the above procedure; in fact, (4.6) can be used by removing terms corresponding to $q_J(r)$.

4.4 Numerical Examples

A computer program is written based on the method discussed in the previous sections. The program assumes that the shape of the junction region (see Fig. 4.1), if it exists, is polygonal, and it can handle an arbitrary number of dielectric layers as well as traces. Each trace is represented by the center point of the ending side and the angle from the x-axis to the center line of a trace (see Fig. 4.4). Nonuniform meshing is utilized to reduce the number of unknowns.

Excess capacitances for four common strip discontinuities, an open end, a step junction, a bend, and a T junction, shown in Fig. 4.3, are computed using the program. The following parameters are used: 1) an open end: $w = 0.5$ mm; 2) a step junction: $w_1 = 0.1$ mm and $w_2 = 0.2$ mm; 3) a right-angle bend: $w_1 = w_2 = 0.15$ mm; and 4) a T junction: $w_1 = w_2 = w_3 = 0.15$ mm. Three different types of media are considered for each discontinuity with the following parameters (see Fig. 4.5): 1) an open end: $\epsilon_1 = 4.2$, $\epsilon_2 = 2.5$, $y_1 = 1.0$ mm, $y_2 = 1.5$ mm, and $y_3 = 2.0$ mm; 2) a step junction: $\epsilon_1 = 6.0$,

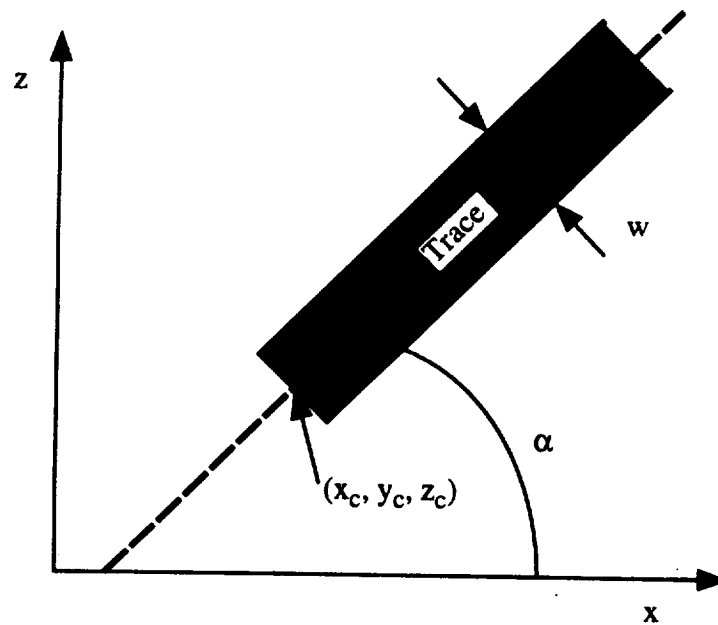


Figure 4.4. Representation used to describe traces.

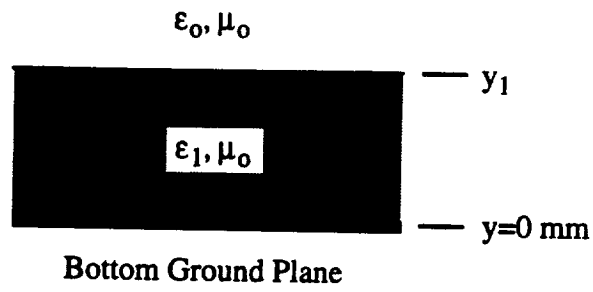
$\epsilon_2 = 4.2$, $y_1 = 0.1$ mm, $y_2 = 0.2$ mm, and $y_3 = 0.3$ mm; 3) a bend: $\epsilon_1 = 2.5$, $\epsilon_2 = 4.2$, $y_1 = 0.15$ mm, $y_2 = 0.3$ mm, and $y_3 = 0.5$ mm; 4) a T junction: $\epsilon_1 = 2.5$, $\epsilon_2 = 4.2$, $y_1 = 0.15$ mm, $y_2 = 0.3$ mm, and $y_3 = 0.5$ mm. All discontinuities are assumed to be embedded at $y = y_1$. To place 3-D unknowns for the excess charge distribution, the length of each trace is truncated at $l = 8w$. The total numbers of unknowns per each trace were 50 for a 2-D problem and 160 for a 3-D problem, whereas 100 unknowns were used for the junction region. The maximum number of exponential functions used to approximate each coefficient function $K_i^\pm(\gamma, m, n)$ was 5.

The computed results are shown in Table 4.1 with the comparison data for the microstrip case (Fig. 4.5(a)). A good agreement was found overall as shown in the table. It is interesting to note that for some cases the value of an excess capacitance turns out to be negative. Although a physical capacitance must be positive, an excess (equivalent) capacitance is hypothetical and can be negative. The excess charge distribution is plotted for the microstrip case in Figs. 4.6, 4.7, 4.8, and 4.9. The excess capacitance of an open end is also computed as a function of a trace width and compared in Fig. 4.10 with the closed-form formula from [2].

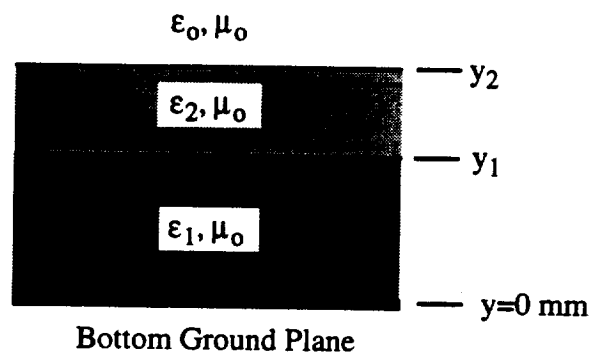
Since the number of unknowns can be quite large for 3-D problems, (4.6) is solved using the iterative methods, such as the Generalized Conjugate Residue (GCR) routine or the Generalized Minimum Residual (GMRES) routine instead of the LU factorization. The comparison of the CPU time used in the above computation for the microstrip case is given in Table 4.2. The CPU time is measured using an Alpha workstation, and the iteration is performed until the maximum relative error is smaller than 0.7%. The gain in the computer time was quite noticeable for the iterative approaches as the number of unknowns increases. Since (4.6) is diagonally dominant, both iterative approaches converged quickly as shown in Table 4.2. In general, the GCR routine performed better than the other approaches; furthermore, it requires less computer memory than for the GMRES routine.

4.5 Summary

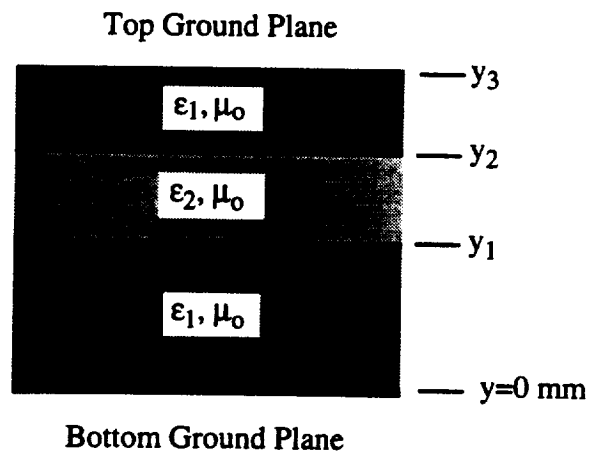
An efficient method to compute excess capacitances of strip discontinuities embedded in a multilayered dielectric medium was discussed in this chapter using the excess charge formulation in conjunction with the closed-form Green's functions; thus, the



(a) Medium 1



(b) Medium 2



(c) Medium 3

Figure 4.5. Three media considered for numerical examples.

Table 4.1. The numerical results (units are in femtofarads).

	Medium 1		Medium 2	Medium 3
	Computation	Others	Computation	Computation
Open End	17.33	17.0 [1]	23.52	19.62
Step Junction	1.120	1.05 [1], 0.74 [8]	1.352	0.609
Bend	6.210	6.75 [1], 5.8 [8]	7.006	9.184
T Junction	1.385	1.9 [8]	-4.917	-0.818

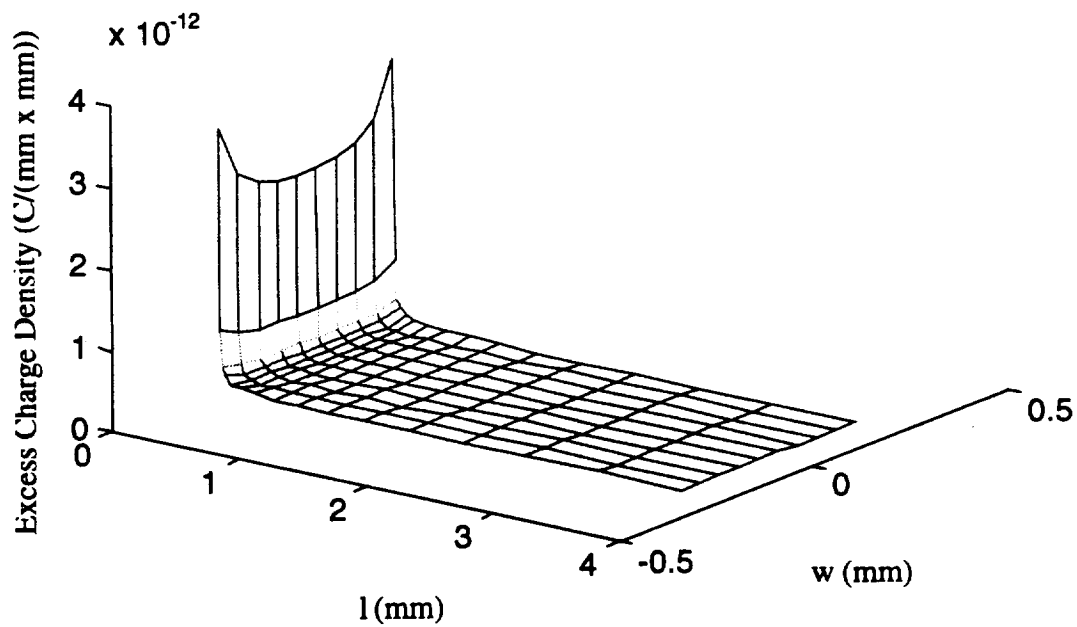
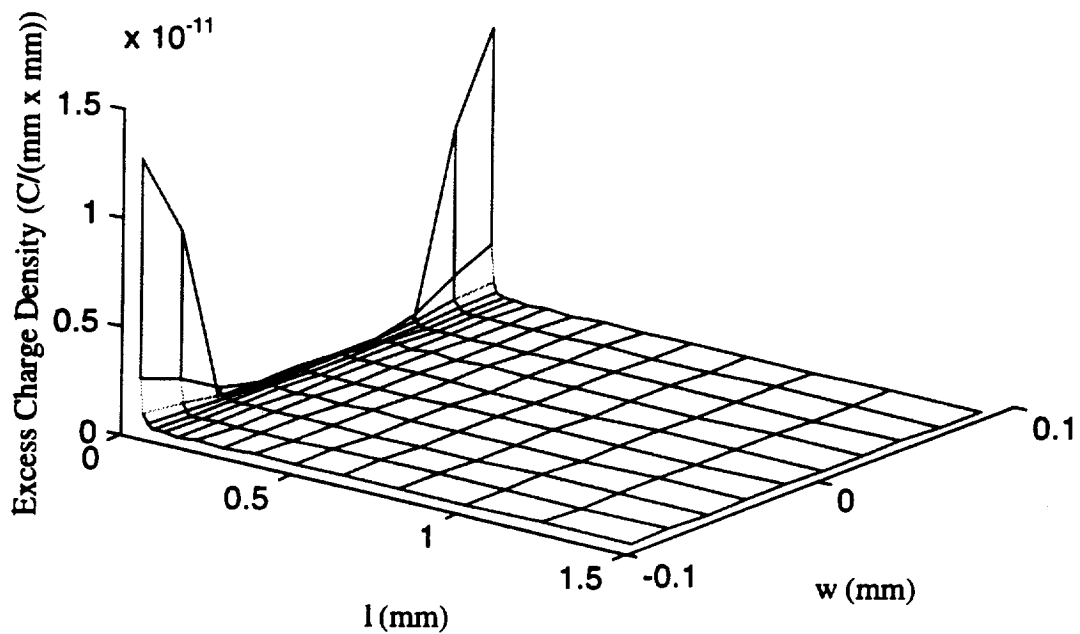
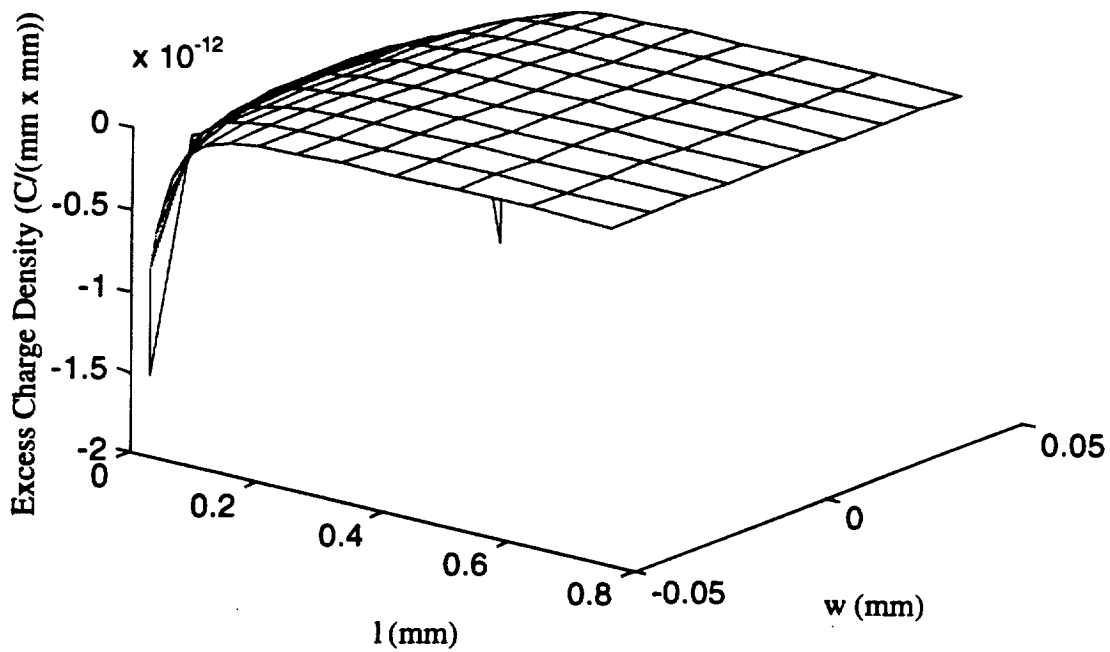


Figure 4.6. The excess charge distribution for the open end case.



(a)



(b)

Figure 4.7. The excess charge distribution on (a) the wider trace and (b) the narrow trace for the step junction case.

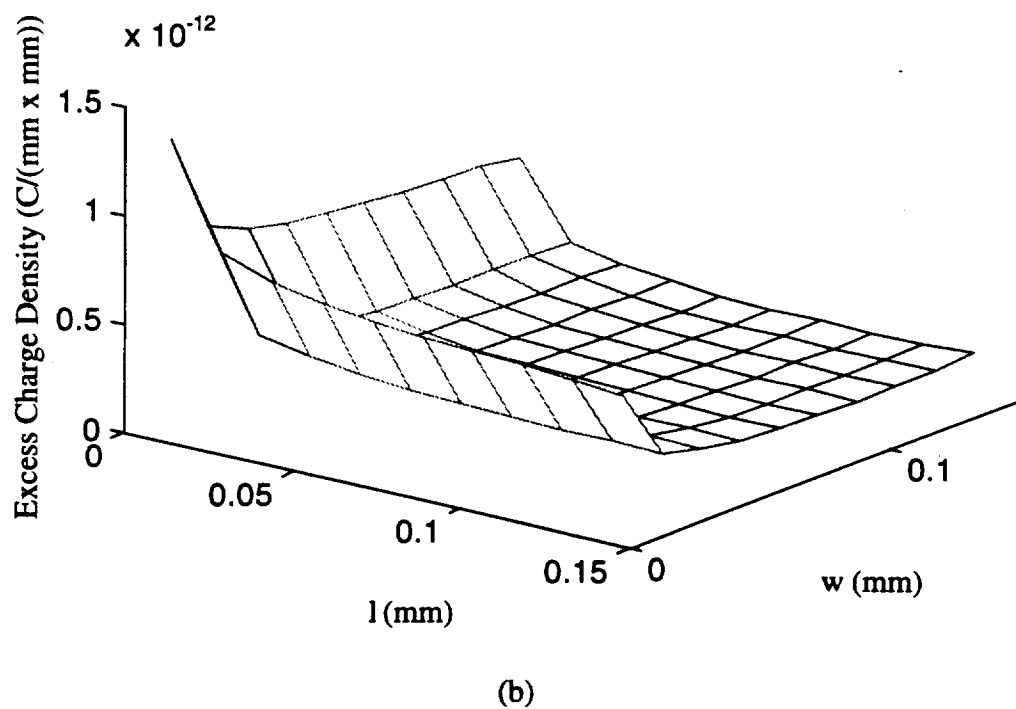
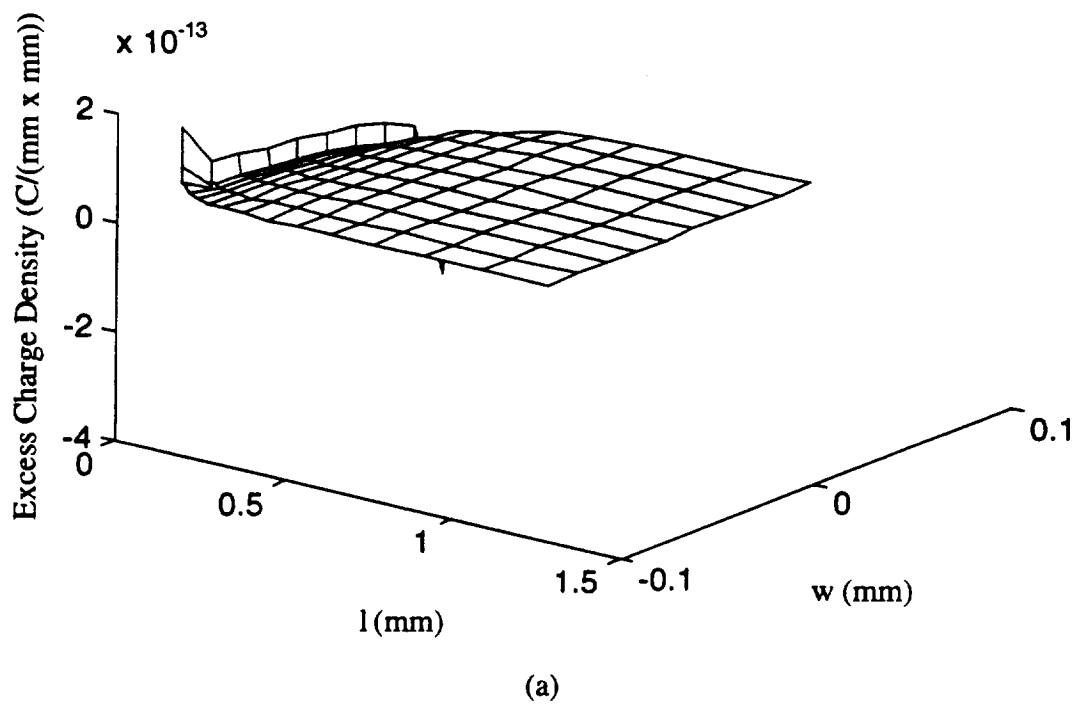


Figure 4.8. The excess charge distribution on (a) the first trace or the second trace and (b) the junction region for the bend case.

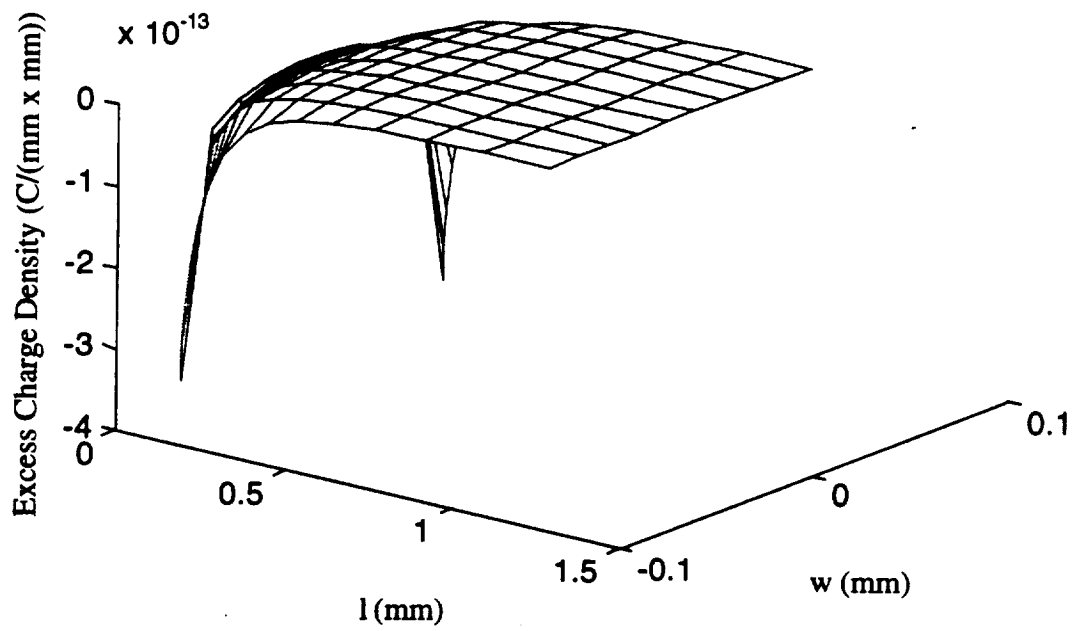
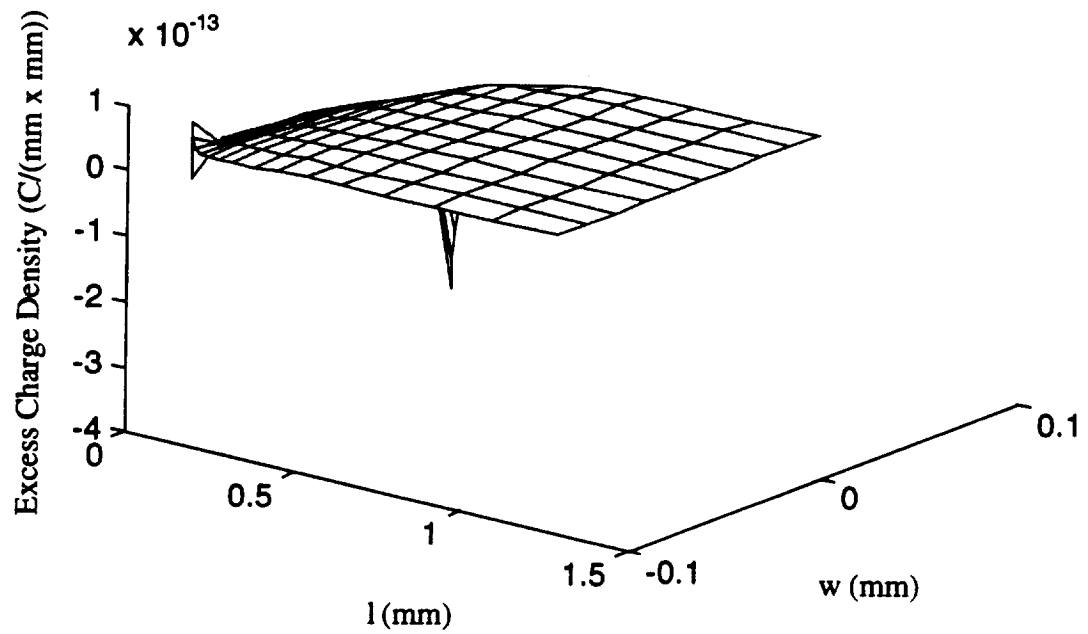
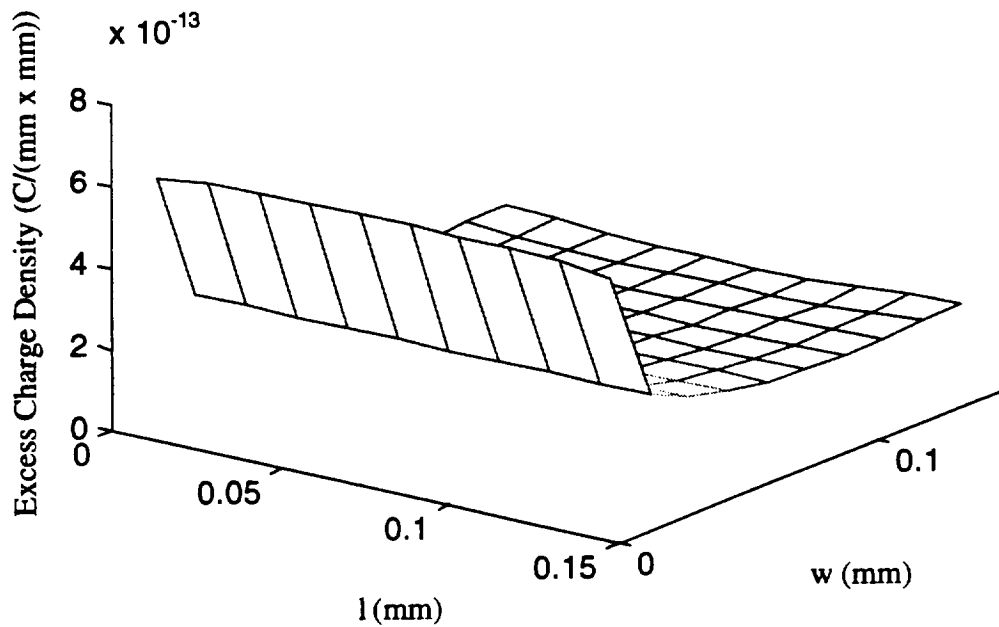


Figure 4.9. The excess charge distribution on (a) the side traces, (b) the center trace, and (c) the junction region for the T junction case.



(c)

Figure 4.9. Continued.

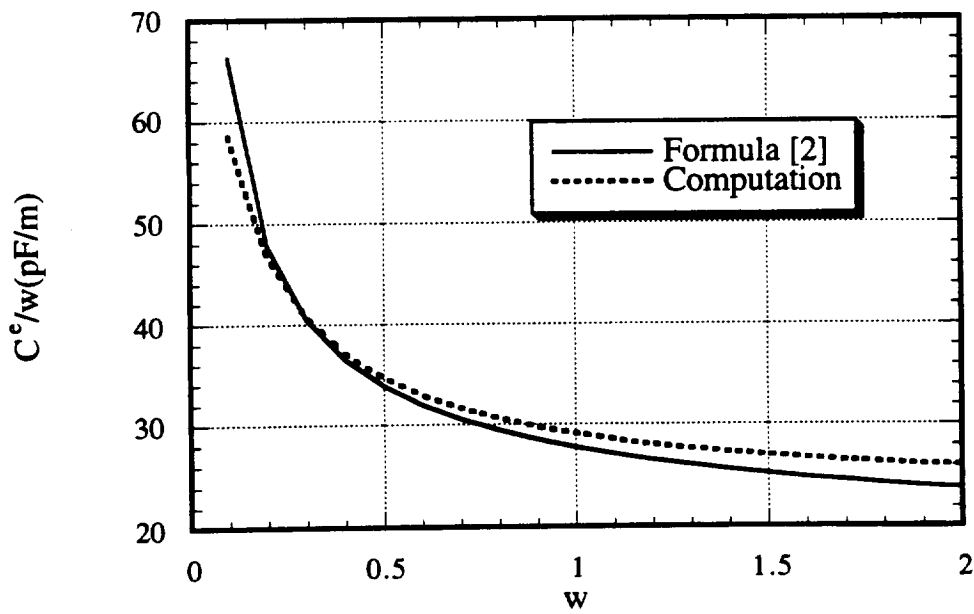


Figure 4.10. C^e for an open end as a function of a trace width.

C-2.

Table 4.2. The CPU time used in the computations.

	GCR		GMRES		LU
	Time (sec)	Iterations	Time (sec)	Iterations	Time (sec)
Open End	12.42	17	12.54	19	12.71
Step Junction	73.40	17	73.49	20	76.37
Bend	88.39	10	8.67	15	95.81
T Junction	116.73	9	167.54	16	187.16

presented method is accurate and numerically efficient. Unlike other approaches, only one integral equation was employed in this chapter to handle various strip discontinuities instead of formulating a different integral equation for each discontinuity type. The numerical results for the microstrip case agreed well with other published results.

4.6 References

- [1] K. C. Gupta, R. Gary, and I. J. Bahl, *Microstrip Lines and Slotlines*. Norwood, MA: Artech House, 1979.
- [2] T. C. Edwards, *Foundations for Microstrip Circuit Design*, 2nd ed. New York, NY: Wiley, 1992.
- [3] P. Silvester and P. B. Benedek, "Equivalent capacitances of microstrip open circuits," *IEEE Trans. Microwave Theory Tech.*, vol. 20, pp. 511-516, August 1972.
- [4] P. Benedek and P. Silvester, "Equivalent capacitances for microstrip gaps and steps," *IEEE Trans. Microwave Theory Tech.*, vol. 20, pp. 729-733, November 1972.
- [5] P. Silvester and P. B. Benedek, "Microstrip discontinuity capacitances for right-angle bends, T junctions, and crossings," *IEEE Trans. Microwave Theory Tech.*, vol. 21, pp. 341-346, May 1973.

- [6] P. Silvester and P. B. Benedek, "Correction to 'Microstrip discontinuity capacitances for right-angle bends, T junctions, and crossings'," *IEEE Trans. Microwave Theory Tech.* (letter), vol. 23, p. 456, May 1975.
- [7] C. Wei, R. F. Harrington, J. R. Mautz, and T. K. Sarkar, "Multiconductor transmission lines in multilayered dielectric media," *IEEE Trans. Microwave Theory Tech.*, vol. 32, pp. 439-450, April 1984.
- [8] T. K. Sarkar, Z. A. Maricevic, J. B. Zhang, and A. R. Djordjevic, "Evaluation of excess inductance and capacitance of microstrip junctions," *IEEE Trans. Microwave Theory Tech.*, vol. 42, pp. 1095-1097, June 1994.

CHAPTER 5

COMPUTATION OF THE EQUIVALENT CAPACITANCE OF A VIA IN A MULTILAYERED BOARD

5.1 Introduction

Although a via is one of the most common discontinuities encountered in high-speed integrated circuits, it has not received as much attention as some of the other discontinuities, e.g., open-end terminations, bends, and junctions. This is due mainly to the nonplanar and complex 3-D geometry of the via, which has often been simplified in the works published previously [1]-[3]. For instance, a via penetrating through a single reference (ground) plane with two wire traces has been considered in [1], and without any traces in [2], while a via above a reference plane with two wire traces but without a through-hole reference plane between these traces has been investigated in [3]. A novel equivalent network model, which accounts for the frequency dependence, has been proposed in [4] and has also been applied to the problem of coupling between two adjacent vias in [5]. In [1] and [3], an integral equation has been formulated in terms of the excess charge distribution to compute the equivalent (excess) capacitance. In this chapter, this excess charge formulation is further generalized for vias with more complex geometries than has been analyzed hitherto and is applied in conjunction with the closed-form Green's function to analyze vias embedded in multilayered dielectric media.

The general description of a via structure is discussed in Section 5.2. An integral equation is formulated using the closed-form Green's functions in Section 5.3 to determine the excess charge distribution of a via, and the method of moments (MoM) is subsequently employed to determine the unknown charge distribution. A detailed discussion of the closed-form Green's functions and the corresponding expressions can be found in Chapter 2. Unlike the strip discontinuities considered in the previous chapter, the conductor traces associated with a via can be located at different vertical locations and a via often goes through several ground planes; hence, the formulation of an integral equation is slightly more complicated than the one given in the previous chapter. Although two different integral equations are used for a via with and without a through-hole ground plane in the other published methods [1], [3], only one integral equation is formulated to handle both cases in this chapter. In Section 5.4, several numerical examples are presented to verify the proposed method.

5.2 General Statement of the Problem

To illustrate the geometries of vias considered in this chapter, a via comprised of three traces and one reference ground plane is shown in Fig. 5.1. In general, a via can pass through N_g reference (ground) planes and N_t traces, and N_p pads can be attached to the via where N_g , N_t , and N_p are all arbitrary. The vias are embedded in a multilayered medium consisting of N_d (arbitrary) dielectric layers, which can be backed by two optional reference planes as shown in Fig. 5.2. To distinguish between these optional reference planes and those associated with the via, we will reserve the term “reference plane” to designate an optional top or bottom reference plane, and use the term “reference conductor” to denote other reference planes. It is evident that the reference conductors must have perforations to avoid any contact with the vias; however, the two optional reference planes are assumed to be solid. To simplify the numerical computation, we assume that all of the conductors are infinitely thin except a via hole, which is assumed to be filled with a conducting material, and that the shapes of all the pads and perforations in the reference conductors are circular.

Two quasi-static equivalent circuit representations of the via shown in Fig. 5.1 are given in Figs. 5.3(a) and 5.3(b). These representations assume that there is at least one reference conductor or one reference plane. The two circuits are equivalent in the sense that one can be obtained from the other; however, the equivalent circuit shown in Fig. 5.3(b) is preferable because equivalent inductances, in general, are computed from terminal (trace) to terminal (trace), and these inductances directly correspond to the ones shown in Fig. 5.3(b)¹. This chapter will only address the problem of computing the total equivalent capacitance C^e . The method to compute the equivalent inductance of a via can be found in [6].

5.3 Formulation of an Integral Equation

An impressed potential on the conductors results in free charge accumulation on the surfaces of conductors, and the electrostatic potential $\phi(r)$ at any point except inside the conductors is then related to this surface charge density $q(r)$ via the following integral equation:

¹Note that for two-terminal (two-trace) case this is irrelevant since L_{e1} and L_{e2} are equal to $L_{e12}/2$.

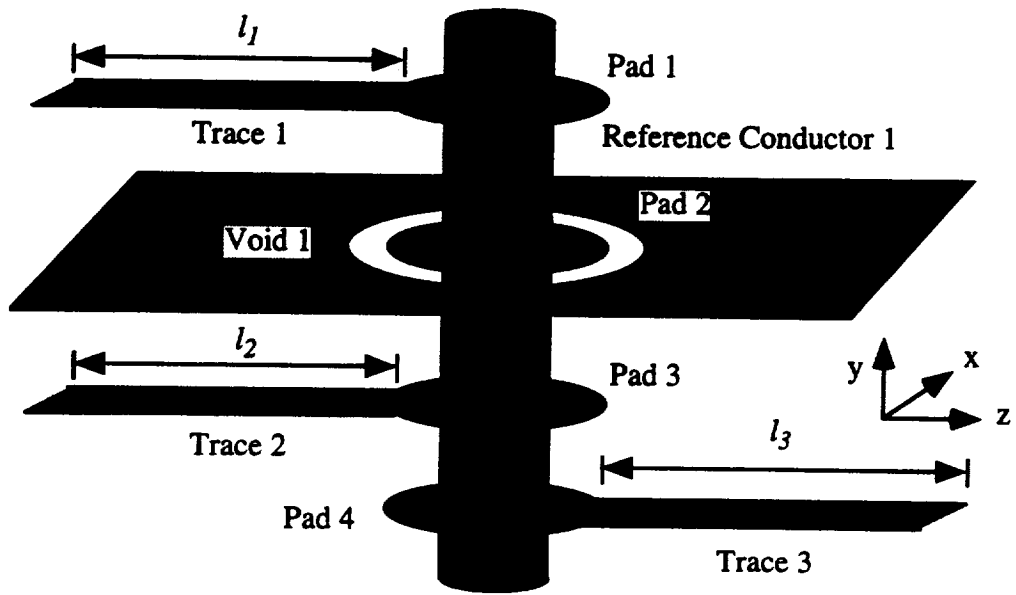


Figure 5.1. The geometry of a via with three traces.

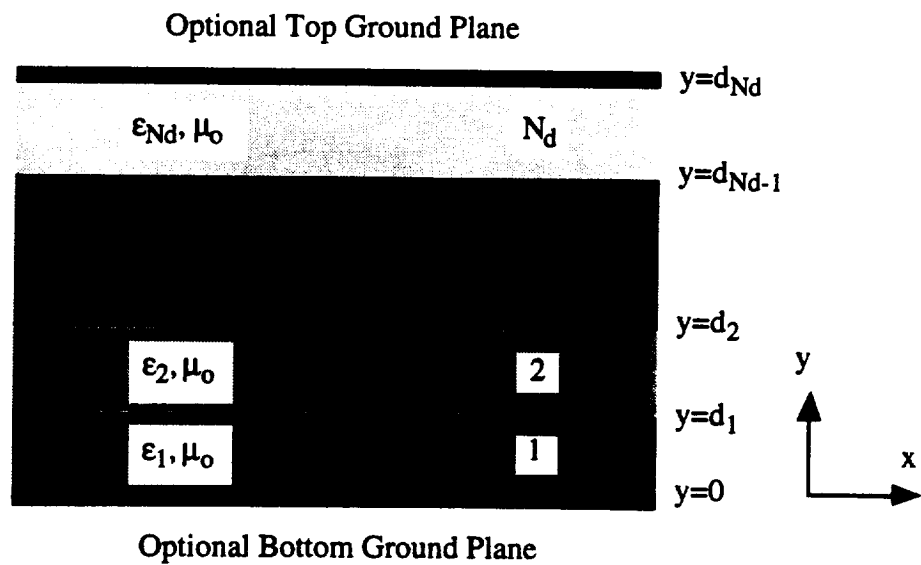


Figure 5.2. Cross-sectional view of a multilayered dielectric medium.

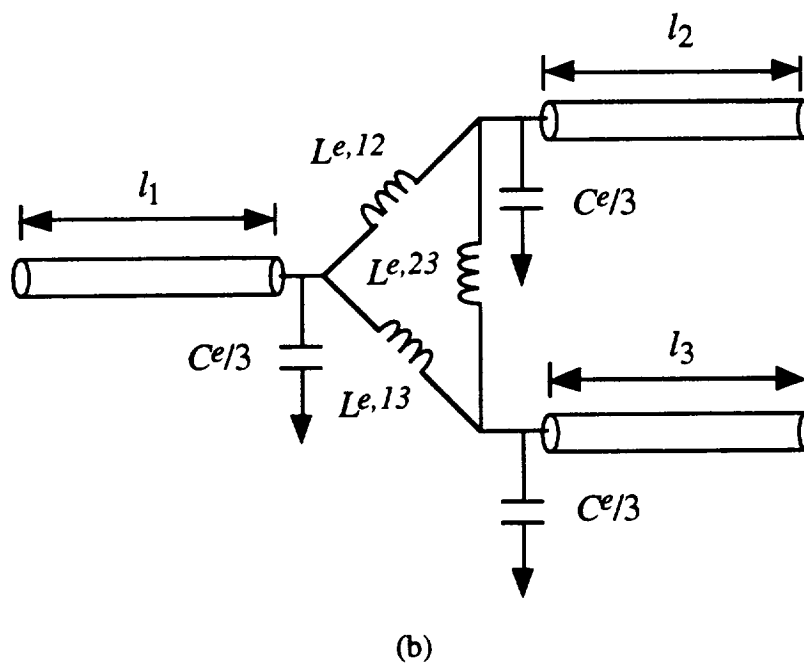
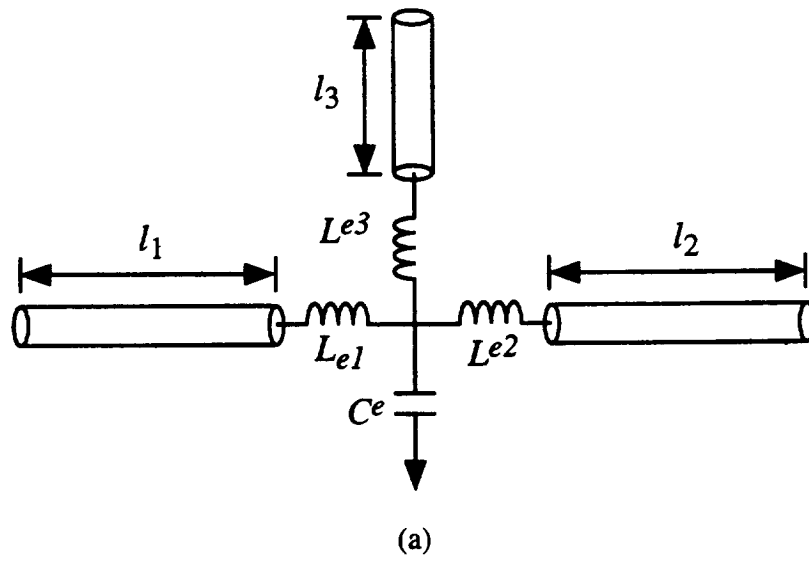


Figure 5.3. Two equivalent circuit representations of the via shown in Fig. 5.1.

$$\phi(r) = \int_{\Omega} G^{3D}(r|r')q(r')dr' = \langle G^{3D}, q \rangle \quad (5.1)$$

where Ω denotes the surfaces of all conductors, including the via and reference conductors. $G^{3D}(r|r')$ is the 3-D closed-form Green's function for a multilayered medium, and it accounts for polarization charges on dielectric interfaces and free charges on the surfaces of reference planes. The integration is symbolically written as $\langle \cdot, \cdot \rangle$ to simplify the notation. Next, we represent the charge density $q(r)$ as follows:

$$q(r) = q_v(r) + \sum_{i=1}^{N_p} q_p^i(r) + \sum_{i=1}^{N_t} q_t^i(r) + \sum_{i=1}^{N_g} q_g^i(r) \quad (5.2)$$

where $q_v(r)$ is the charge density on the surface of a via hole, and $q_p^i(r)$, $q_t^i(r)$, and $q_g^i(r)$ are the charge densities on the i th pad, trace, and reference conductor, respectively. Equation (5.1) can be rewritten as

$$\phi(r) = \langle G^{3D}, q_v \rangle + \sum_{i=1}^{N_p} \langle G^{3D}, q_p^i \rangle + \sum_{i=1}^{N_t} \langle G^{3D}, q_t^i \rangle + \sum_{i=1}^{N_g} \langle G^{3D}, q_g^i \rangle \quad (5.3)$$

Next, the charge density $q_t^i(r)$ is decomposed into the uniform charge density $q_t^{unif,i}(r)$ and the excess charge density $q_t^{excess,i}(r)$:

$$q_t^i(r) = q_t^{unif,i}(r) + q_t^{excess,i}(r) \quad (5.4)$$

Here, $q_t^{unif,i}(r)$ is the uniform charge density on the i th trace under the assumptions that it is infinite in both directions, no other traces are present, and the reference conductors have no perforations; this charge density is computed by solving an appropriate 2-D problem. Since the reference conductors become uniform planes without any perforations for this 2-D problem, the potential distribution on the region above the reference conductor is not affected by the region below it and vice versa. To solve for $q_t^{unif,i}(r)$, it is then expedient to introduce a new medium surrounding the i th trace. As a consequence, the medium employed in the 2-D problem is generally different from that of the 3-D via problem, and could, in fact, be different for each trace. Once the appropriate medium has been chosen, $q_t^{unif,i}(r)$ can be obtained by using the method described in Section 3.2. The resulting

$q_t^{unif,i}(r)$ yields the capacitance per unit length for the i th transmission line in the equivalent circuit representation shown in Fig. 5.3.

In the process of determining $q_t^{unif,i}(r)$, the 2-D closed-form Green's function $G^{2D,i}(\rho|\rho_o)$ is used to formulate an integral equation for a 2-D problem in Section 2.2. However, in the integral equation (5.3) for computing the equivalent capacitance problem, the uniform charge density $q_t^{unif,i}(r)$ resides on the i th trace, which is only a semi-infinite line. It is therefore necessary to employ $G^{semi,i}(r|r_o, \xi)$ to compute the potential due to $q_t^{unif,i}(r)$. Using (5.4), (5.3) can be rewritten as

$$\begin{aligned} \phi(r) - \sum_{i=1}^{N_t} \langle G^{semi,i}, q_t^{unif,i} \rangle = \\ \langle G^{3D}, q_v \rangle + \sum_{i=1}^{N_p} \langle G^{3D}, q_p^i \rangle + \sum_{i=1}^{N_t} \langle G^{3D}, q_t^{excess,i} \rangle + \sum_{i=1}^{N_g} \langle G^{3D}, q_g^i \rangle \end{aligned} \quad (5.5)$$

Next, if we set the via potential to be ϕ_o with respect to the reference conductors and planes, $\phi(r)$ becomes ϕ_o on the surfaces of the via hole, pads, and traces, and is equal to 0 on the surfaces of reference conductors. Hence, once $q_t^{unif,i}(r)$ has been determined, all of the quantities associated with the left-hand side of the above equation can be considered to be known at the surface of the conductors.

The integral equation (5.5) can now be solved by using the method of moments. In this method, the surfaces of the conductors, with the exclusion of the reference planes, are first discretized with polygonal patches. Next, the unknown charge distributions, $q_v(r)$, $q_p^i(r)$, $q_t^{excess,i}(r)$, and $q_g^i(r)$, are expanded with pulse-type basis functions over these patches. For instance, we wrote $q_v(r)$ as

$$q_v(r) = \sum_{j=1}^{N_v} q_{v,j} P_j(r) \quad (5.6)$$

where $P_j(r)$ is 1 if r is in the j th patch used to discretize the via hole and, 0, otherwise. Evaluating (5.5) at the centers of all the patches results in a system of linear equations, which yields the unknown charge distribution similar to (4.6) in Chapter 4. The various integrations appearing in (5.5) can be evaluated analytically for pulse-type basis functions using closed-form formulas given in Sections 2.3 and 2.4.

Once the unknown charge distributions have been determined, the equivalent (excess) capacitance C_e can be obtained by using the following expression which involves the integrals of these charge distributions:

$$C_e \phi_0 = \int_{\Omega_v} q_v(r') dr' + \sum_{i=1}^{N_p} \int_{\Omega_{p,i}} q_p^i(r') dr' + \sum_{i=1}^{N_t} \int_{\Omega_{t,i}} q_t^{excess,i}(r') dr' \quad (5.7)$$

where Ω_v is the surface of a via hole, and $\Omega_{p,i}$ and $\Omega_{t,i}$ are the surfaces of the i th pad and trace, respectively.

5.4 Numerical Examples

First, two numerical examples are considered to illustrate the application of the method presented above to the computation of the equivalent capacitances of two via structures, one with a reference plane and the other with a reference conductor. The detailed geometries of the two via structures are shown in Figs. 5.4 and 5.5. The computed excess capacitances for Fig. 5.4 with 1) $\epsilon_1 = \epsilon_2 = \epsilon_0$ and 2) $\epsilon_1 = 4\epsilon_0$ and $\epsilon_2 = \epsilon_0$; for Fig. 5.5 with 3) $\epsilon_1 = \epsilon_2 = 4\epsilon_0$ and 4) $\epsilon_1 = 4.5\epsilon_0$ and $\epsilon_2 = 5.4\epsilon_0$ are listed in Table 5.1 along with data obtained from [1] and [3]. In [1] and [3], the strips were replaced by the equivalent wires of radii which are one-fourth of the widths of the strips. In our computation, the lengths of all traces have been truncated to $2.5h$, whereas the width of the reference conductor has been truncated to $1.5l$, with h and l being the height of a via hole and the length of the traces. The truncation of traces and reference conductors is valid since the excess charge distribution decays rapidly as we move away from the center of a via. A total of 263 and 687 unknowns were used for the vias shown in Figs. 5.4 and 5.5, respectively. As shown in Table 5.1, the data for the via shown in Fig. 5.4 agree well with the published results. However, the data for the via shown in Fig. 5.5 are considerably different from the results reported elsewhere. Unfortunately, no experimental result for this structure is available to establish the relative accuracy of these results associated with Fig. 5.5.

Table 5.1. Equivalent capacitances for vias shown in Figs. 5.4 and 5.5. Units are in picofarads.

	Fig. 5.4		Fig. 5.5	
	$\epsilon_1=\epsilon_2=\epsilon_0$	$\epsilon_1=4\epsilon_0, \epsilon_2=\epsilon_0$	$\epsilon_1=\epsilon_2=4\epsilon_0$	$\epsilon_1=4.5\epsilon_0, \epsilon_2=5.4\epsilon_0$
Computed Result	0.3841	1.233	9.952	12.31
Others	0.3701 [3]	1.28 [3]	6.35 [1]	7.85 [1]

The equivalent capacitance of the via shown in Fig. 5.6 is obtained from the experiment based on Hewlett Packard Application Note #67 using a 500 ps rise-time input signal; the resulting capacitance value was 0.504 pF. To apply the presented method to this via, only that portion between the ground planes is modeled in the computation, and it is assumed the two ground planes are uniform. The total of 382 unknowns is used in the computation and the computed excess capacitance value was 0.395 pF.

The comparisons of the CPU time at the Alpha workstation for various matrix solution techniques are given in Table 5.2. Again, the GCR routine performed best for all examples as in the previous chapter.

5.5 Summary

A method to compute the equivalent capacitance of a via, which is based on an integral equation formulated in terms of the excess charge formulation, has been presented in this chapter. The method is applicable to via geometries with or without through-hole reference conductors. The closed-form Green's function was employed to circumvent the time-consuming evaluation of a nested infinite series, required in the evaluation in [3].

Additional computational savings can be achieved via the use of the Fast Multipole Method (FMM) [7], an algorithm to speed up the computation time in 3-D capacitance calculations, in conjunction with the closed-form Green's function for a multilayered

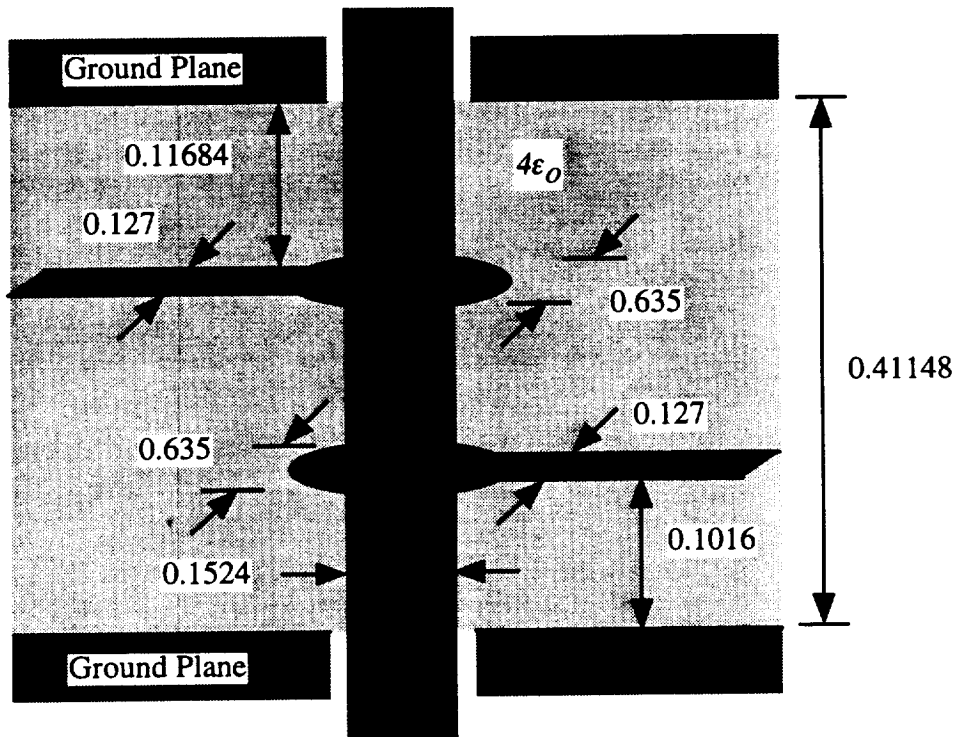


Figure 5.6. A two-trace via used to obtain the experimental data. Units are in millimeters.

Table 5.2. The CPU time used in the computations.

	GCR		GMRES		LU
	Time (sec)	Iterations	Time (sec)	Iterations	Time (sec)
Fig. 5.4	13.18	28	14.14	52	17.12
Fig. 5.5	81.22	35	120.08	50	161.93
Fig. 5.6	167.46	12	167.52	17	171.76

medium. In the following chapter, such an implementation of the multipole method with the closed-form Green's function is demonstrated for the computation of the equivalent capacitance of a strip crossover.

5.6 References

- [1] T. Wang, R. F. Harrington, and J. R. Mautz, "Quasi-static analysis of a microstrip via through a hole in a ground plane," *IEEE Trans. Microwave Theory Tech.*, vol. 36, pp. 1008-1013, June 1988.
- [2] P. Kok and D. D. Zutter, "Capacitance of a circular symmetric model of a via hole including finite ground plane thickness," *IEEE Trans. Microwave Theory Tech.*, vol. 39, pp. 1229-1234, July 1991.
- [3] T. Wang, J. R. Mautz, and R. F. Harrington, "The excess capacitance of a microstrip via in a dielectric substrate," *IEEE Trans. Computed-Aided Design.*, vol. 9, pp. 48-56, January 1990.
- [4] Q. Gu, Y. E. Yang, and M. A. Tassoudji, "Modeling and analysis of vias in multilayered integrated circuits," *IEEE Trans. Microwave Theory Tech.*, vol. 41, pp. 206-214, February 1993.
- [5] Q. Gu, M. A. Tassoudji, S. Y. Poh, R. T. Shin, and J. A. Kong, "Coupled noise analysis for adjacent vias in multilayered digital circuits," *IEEE Trans. Circuit Syst.*, vol. 41, pp. 796-804, December 1994.
- [6] A. R. Djordjevic and T. K. Sarkar, "Computation of inductance of simple vias between two striplines above a ground plane," *IEEE Trans. Microwave Theory Tech.*, vol. 33, pp. 265-269, March 1985.
- [7] K. Nabors, S. Kim, and J. White, "Fast capacitance extraction of general three-dimensional structures," *IEEE Trans. Microwave Theory Tech.*, vol. 40, pp. 1496-1506, July 1992.

CHAPTER 6

COMPUTATION OF THE EQUIVALENT CAPACITANCE OF A STRIP CROSSOVER IN A MULTILAYERED MEDIUM

6.1 Introduction

In Chapters 4 and 5, the equivalent capacitances of various junction discontinuities and a via have been considered based on the quasi-static approximation. In this chapter, the equivalent capacitance of yet another common discontinuity, a strip crossover, is considered. Like the methods presented in the two previous chapters, the method discussed in this chapter is also based on the quasi-static approximation and utilizes a closed-form Green's function.

To compute the equivalent capacitance for orthogonally crossing strips without a top ground plane, an iterative spectral-domain approach is used in [1], a spatial Green's function with the infinite series expansion is used in [2], and a spatial Green's function based on the complex images is used in [3]. A crossover embedded in lossy multilayered media is also considered in [4]. The full-wave analysis of a strip crossover appears in [5]-[7]. In this chapter, the closed-form Green's function is applied to a crossover of an arbitrary crossing angle and an additional top ground plane.

The Fast Multipole Method (FMM) [8]-[12] is a class of algorithms used for the rapid evaluation of potentials in large systems. The techniques in [8]-[11] have been applied to compute the capacitance of conducting structures in a homogeneous medium [10] and in the presence of finite-sized dielectrics [14]. Anderson's fast-multipole method [12], which is equivalent in complexity and accuracy to the methods described in [8]-[11], has been applied in conjunction with the closed-form Green's function for computing the capacitance matrices of conducting structures that reside in a layered dielectric medium [15]. In this chapter, the possible usage of the FMM to accelerate the MoM computation of the equivalent capacitance calculation is demonstrated. Numerical experiments show that a substantial amount of computer time is saved without a loss of accuracy.

6.2 General Statement of the Problem

Consider two strips crossing at an angle α as shown in Fig. 6.1(a). The bottom and top strips are denoted by Conductors 1 and 2, respectively. Although this chapter will focus on strips, the proposed method is applicable to conductors of arbitrary cross section. The strips are embedded in a multilayered dielectric medium depicted in Fig. 6.1(b). An arbitrary number N_d of dielectric layers are located on top of a ground plane, and the multilayered dielectric medium is terminated by an optional ground plane on the other side. The dielectric medium is assumed to be uniform and of infinite extent along the x - and y -directions.

When compared to bends or junctions, the discontinuity effect associated with a strip crossover is less localized due to the absence of the nonuniformity of conductor geometries. As a consequence, an equivalent circuit with distributed parameters may be needed to accurately model the crossover. Although the required parameters can be obtained by using the proposed method, a circuit with distributed parameters is not convenient to simulate in practice. Only the simple lumped equivalent circuit shown in Fig. 6.2 will be used in this chapter. Unlike the discontinuities considered in the previous chapters, a crossover consists of two electrically isolated conductors; hence, the equivalent circuit representation of a crossover consists of three capacitances, and a coupled integral equation has to be solved to determine these capacitances. In general, an equivalent inductance should be incorporated into the equivalent circuit to model current coupling for nonorthogonal crossovers; however, this chapter only concentrates on the computation of an equivalent capacitance.

The remainder of this chapter is organized as follows. In Section 6.3, a coupled integral equation in terms of excess charge densities is formulated using a closed-form static Green's function described in Chapter 2. Then, the Fast Multipole Method is introduced in Section 6.4, and it is demonstrated how it can be used to accelerate the MoM solution of the integral equation. Finally, various numerical examples are presented in Section 6.5.

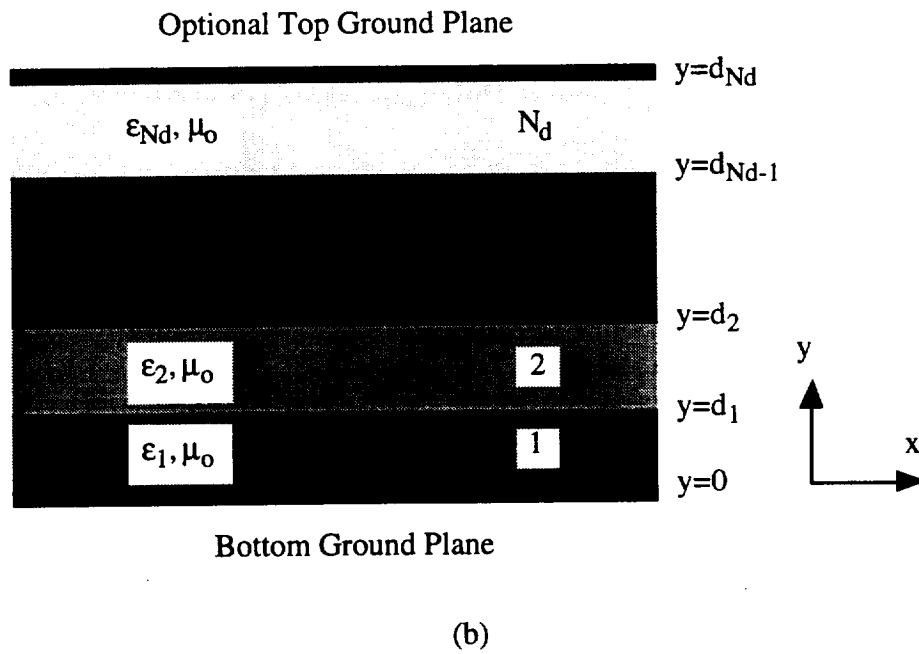
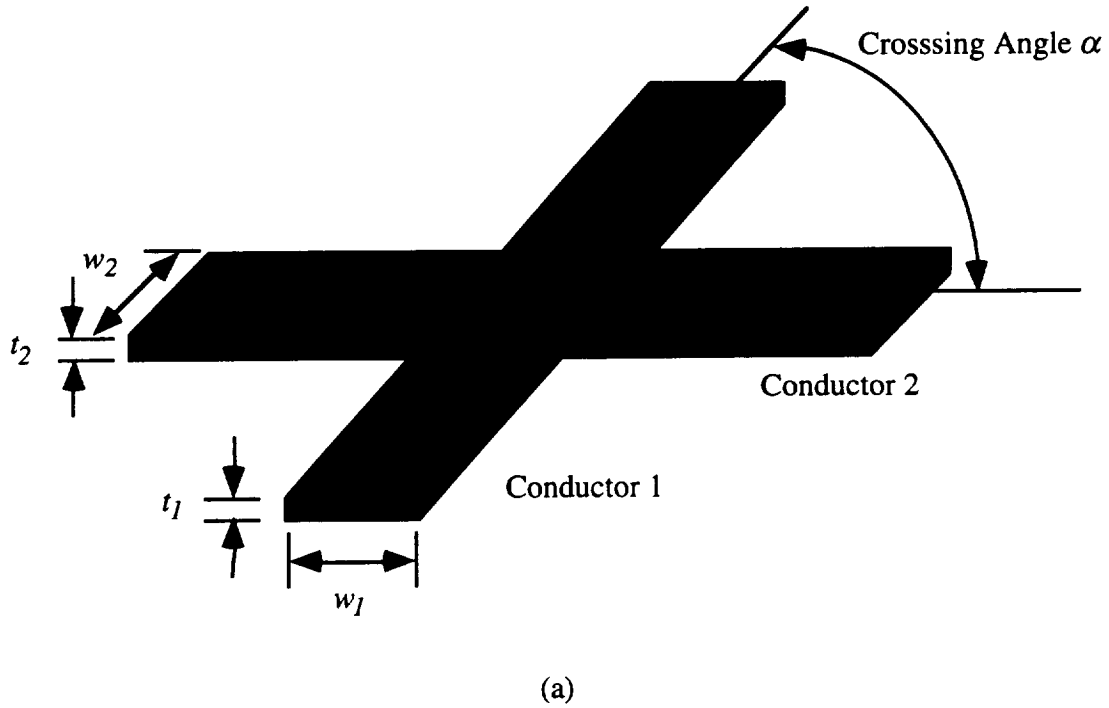


Figure 6.1. Geometries of (a) a strip crossover and (b) a multilayered dielectric medium.

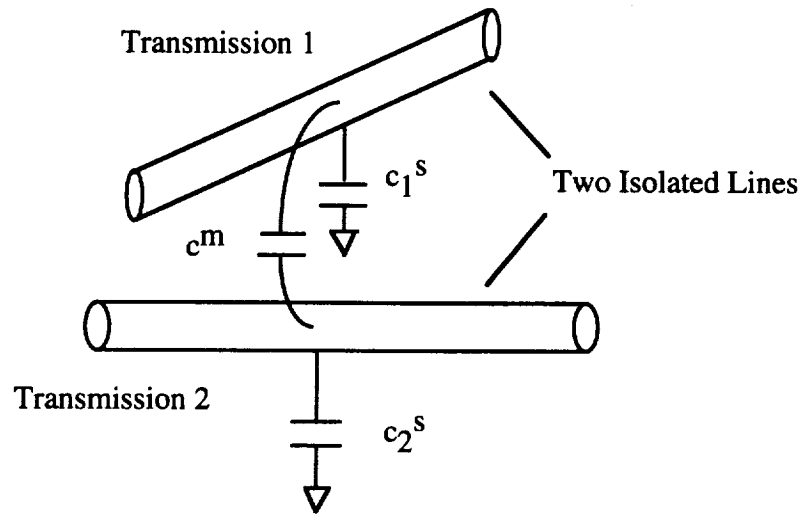


Figure 6.2. Equivalent circuit representation of a strip crossover.

6.3 Formulation of an Integral Equation

Let us first assume that the strip crossover depicted in Fig. 6.1(a) is embedded in a multilayered dielectric medium with both top and bottom ground planes. An impressed electrostatic potential on conductors results in charge accumulation on the surfaces of conductors. The electrostatic potential $\Psi(r)$ at any point is related to this accumulated surface charge density $q(r)$ through the following integral equation:

$$\Psi(r) = \int_{\Omega} G^{3D}(r, r') q(r') dr' = \langle G^{3D}, q \rangle \quad (6.1)$$

where G^{3D} is the 3-D Green's function for the multilayered medium, and Ω denotes the surface of the conductors. The integration is again symbolically written as $\langle \cdot, \cdot \rangle$ to simplify the notation.

As noted in Chapter 2, the spectral-domain Green's function for a layered medium with both top and bottom ground planes cannot be approximated with a finite number of exponential functions owing to the existence of a pole; therefore, both 2-D and 3-D Green's functions in the space domain cannot be represented by a finite number of weighted images. Although the exact closed-form expression (without weighted images) can still be found for the 2-D space-domain Green's function (see Appendix B), such a closed-form expression cannot be found for the 3-D space-domain Green's function; the expression of

the 3-D Green's function consists of slowly converging infinite series due to the infinite number of image charges. To avoid the use of this 3-D Green's function, the top ground plane is truncated and modeled as an additional conductor; hence, G^{3D} used in this chapter refers to the 3-D Green's function for a multilayered dielectric medium with only the bottom ground plane. This approach results in a large number of unknowns due to modeling the top ground plane. It may therefore be computationally inefficient to use this approach as compared to using the Green's function with an infinite series expansion. However, when a multipole-accelerated algorithm is applied, it is expected that the proposed approach will result in better computational efficiency in terms of memory usage and CPU time than that due to the use of the Green's function with an infinite series expansion. This is primary because of the small number of images required in the closed-form Green's function.

Now let us represent the surface charge density $q(r)$ as follows:

$$q(r) = q_{c1}(r) + q_{c2}(r) + q_{Tplane}(r) \quad (6.2)$$

where $q_{c1}(r)$, $q_{c2}(r)$, and $q_{Tplane}(r)$ are the surface charge densities on Conductor 1, Conductor 2, and the top ground plane, respectively. The Green's function G^{3D} account for the charge density on the bottom ground plane and the polarization charge densities on the dielectric interfaces. By exciting Conductor 1 to a voltage ϕ_o with respect to Conductor 2 and ground planes, (6.1) becomes

$$\phi_o = \langle G^{3D}, q_{c1}^1 \rangle + \langle G^{3D}, q_{c2}^1 \rangle + \langle G^{3D}, q_{Tplane}^1 \rangle \quad \text{for } r \text{ on Conductor 1} \quad (6.3a)$$

$$0 = \langle G^{3D}, q_{c1}^1 \rangle + \langle G^{3D}, q_{c2}^1 \rangle + \langle G^{3D}, q_{Tplane}^1 \rangle$$

$$\text{for } r \text{ on Conductor 2 and top plane} \quad (6.3b)$$

The superscript 1 in q_{c1}^1 , q_{c2}^1 , q_{Tplane}^1 denotes the charge densities due to the excitation of ϕ_o on Conductor 1 with respect to Conductor 2 and the ground planes. Now let

$$q_{c1}^1(r) = q_{c1}^{1,unif}(r) + q_{c1}^{1,excess}(r) \quad (6.4a)$$

$$q_{c2}^1(r) = q_{c2}^{1,excess}(r) \quad (6.4b)$$

where $q_{c1}^{1,unif}(r)$ is the uniform charge density obtained by solving the 2-D problem for isolated Conductor 1, i.e., without Conductor 2 but with the top ground plane. This problem is solved using the 2-D Green's function G^{2D} with the excitation voltage set to ϕ_o . A detailed discussion of this procedure is given in Section 3.2. Equation (6.3) can then be written as

$$\phi_o = \langle G^{2D}, q_{c1}^{1,unif} \rangle + \langle G^{3D}, q_{c1}^{1,excess} \rangle + \langle G^{3D}, q_{c2}^{1,excess} \rangle + \langle G^{3D}, q_{Tplane}^{1,excess} \rangle \quad (6.5a)$$

$$0 = \langle G^{2D}, q_{c1}^{1,unif} \rangle + \langle G^{3D}, q_{c1}^{1,excess} \rangle + \langle G^{3D}, q_{c2}^{1,excess} \rangle + \langle G^{3D}, q_{Tplane}^{1,excess} \rangle \quad (6.5b)$$

Here, G^{2D} is the 2-D Green's function for a layered medium with both top and bottom ground planes, and G^{3D} is the 3-D Green's function for a layered medium with only a bottom ground plane.¹ In (6.3) and (6.5), $q_{Tplane}^{1,excess}$ and $q_{Tplane}^{1,excess}$ represent two different charge distributions on the top ground plane: $q_{Tplane}^{1,excess}$ is the induced total charge distribution due to the total charge distributions on the strips, whereas $q_{Tplane}^{1,excess}$ is the induced charge distribution due only to the excess charge distributions on the strips. The induced charge distribution on the top ground plane from the uniform charge distribution on the strips is embedded in G^{2D} in (6.5). Since both the excess charge distributions on the strips and the induced partial charge distribution on the top ground plane from these excess charge distributions are all localized around the cross-over region, the strips and a top ground plane can be safely truncated when modeling the excess charge density $q_{Tplane}^{1,excess}$.

Noting that $\langle G^{2D}, q_{c1}^{1,unif} \rangle$ is equal to ϕ_o on Conductors 1 and 0 on the top ground plane, (6.5) becomes

$$0 = \langle G^{3D}, q_{c1}^{1,excess} \rangle + \langle G^{3D}, q_{c2}^{1,excess} \rangle + \langle G^{3D}, q_{Tplane}^{1,excess} \rangle$$

for r on Conductor 1 and top plane (6.6a)

$$-\langle G^{2D}, q_{c1}^{1,unif} \rangle = \langle G^{3D}, q_{c1}^{1,excess} \rangle + \langle G^{3D}, q_{c2}^{1,excess} \rangle + \langle G^{3D}, q_{Tplane}^{1,excess} \rangle$$

for r on Conductor 2 (6.6b)

¹When the top ground plane is not present, both G^{2D} and G^{3D} are the Green's functions for the same medium, and the exponential approximation can be performed only once in the spectral domain to obtain expressions for both G^{2D} and G^{3D} .

Following a similar procedure, but exciting Conductor 2 to a potential ϕ_o with respect to the other conductors instead of Conductor 1, leads to

$$-\langle G^{2D}, q_{c2}^{2,unif} \rangle = \langle G^{3D}, q_{c1}^{2,excess} \rangle + \langle G^{3D}, q_{c2}^{2,excess} \rangle + \langle G^{3D}, q_{Tplane}^{2,excess} \rangle$$

for r on Conductor 1 (6.7a)

$$0 = \langle G^{3D}, q_{c1}^{2,excess} \rangle + \langle G^{3D}, q_{c2}^{2,excess} \rangle + \langle G^{3D}, q_{Tplane}^{2,excess} \rangle$$

for r on Conductor 2 and top plane (6.7b)

The superscript 2 in $q_{c1}^{2,excess}$, $q_{c2}^{2,excess}$, $q_{Tplane}^{2,excess}$ denotes the excess charge densities as a result of the excitation of Conductor 2.

The method of collocation, which is based on the pulse-type basis functions and the delta testing function, is used to solve the above coupled integral equations, (6.6) and (6.7), and the resulting linear system of equations is

$$\begin{bmatrix} 0 & V_{21} \\ V_{12} & 0 \\ 0 & 0 \end{bmatrix} \begin{bmatrix} q_1^{1,unif} & 0 \\ 0 & q_2^{2,unif} \end{bmatrix} = \begin{bmatrix} M_{11} & M_{12} & M_{13} \\ M_{21} & M_{22} & M_{23} \\ M_{31} & M_{32} & M_{33} \end{bmatrix} \begin{bmatrix} q_1^{1,excess} & q_1^{2,excess} \\ q_2^{1,excess} & q_2^{2,excess} \\ q_{Tplane}^{1,excess} & q_{Tplane}^{2,excess} \end{bmatrix} \quad (6.8)$$

where

$$[M_{ij}]_{pq} = \iint_{S_q} G^{3D}(r_p, r') ds' \quad (6.9a)$$

$$[V_{ij}]_{pq} = \int_{C_q} G^{2D}(\rho_p, \rho') dl \quad (6.9b)$$

$$\mathbf{q}_j^{i,excess} = [q_{j,1}^{i,excess}, q_{j,2}^{i,excess}, \dots, q_{j,N_j}^{i,excess}]^T \quad (6.9c)$$

$$\mathbf{q}_{Tplane}^{i,excess} = [q_{Tplane,1}^{i,excess}, q_{Tplane,2}^{i,excess}, \dots, q_{Tplane,N_{Tplane}}^{i,excess}]^T \quad (6.9d)$$

$$\mathbf{q}_i^{i,unif} = [q_{i,1}^{2D}, q_{i,2}^{2D}, \dots, q_{i,N_i}^{2D}]^T \quad (6.9e)$$

Here, S_q and C_q denote the source patch and line segment for 3-D and 2-D problems, respectively. N_j is the total number of patches used to represent $q_j^{i,excess}(r)$, and N_i^{2D} is the total number of line segments used to represent $q_{ci}^{i,unif}(r)$. N_{Tplane} is the total number of patches to represent $q_{Tplane}^{i,excess}(r)$. It should be emphasized that all quantities appearing in the left-hand side of (6.8) are known assuming that $q_i^{i,unif}$ is precomputed by solving the 2-D problem for isolated Conductor i .

The equation corresponding to (6.8) for a case without the top ground plane can be simply expressed as

$$\begin{bmatrix} 0 & \mathbf{V}_{21} \\ \mathbf{V}_{12} & 0 \end{bmatrix} \begin{bmatrix} \mathbf{q}_1^{1,unif} & 0 \\ 0 & \mathbf{q}_2^{2,unif} \end{bmatrix} = \begin{bmatrix} \mathbf{M}_{11} & \mathbf{M}_{12} \\ \mathbf{M}_{21} & \mathbf{M}_{22} \end{bmatrix} \begin{bmatrix} \mathbf{q}_1^{1,excess} & \mathbf{q}_1^{2,excess} \\ \mathbf{q}_2^{1,excess} & \mathbf{q}_2^{2,excess} \end{bmatrix} \quad (6.10)$$

Once (6.8) or (6.9) is solved, the equivalent capacitance can be obtained by

$$\begin{bmatrix} C_1^{1,excess} & C_1^{2,excess} \\ C_2^{1,excess} & C_2^{2,excess} \end{bmatrix} = \begin{bmatrix} Q_1^{1,excess} & Q_1^{2,excess} \\ Q_2^{1,excess} & Q_2^{2,excess} \end{bmatrix} \quad (6.11a)$$

$$C^m = -C_2^{1,excess} = -C_1^{2,excess} \quad (6.11b)$$

$$C_i^s = C_i^{i,excess} - C^m \quad (6.11c)$$

where

$$Q_j^{i,excess} = \sum_{k=1}^{N_j} q_{j,k}^{i,excess} \cdot Area_{j,k} \quad (6.11d)$$

and $Area_{j,k}$ is the area of the k th patch in conductor j . In the above formulas, it is assumed that (6.8) or (6.10) is solved with ϕ_o set to 1.

It should be noted that the difference between the integral equations for the general 3-D capacitance computation and the equivalent excess capacitance lies only in the left side of (6.8) or (6.10), i.e., in the excitation vectors. This fact allows the Fast Multipole

²The later equality is due to the reciprocity; however, $C_1^{1,excess}$ and $C_1^{2,excess}$, in general, are slightly different due to the numerical side effect, and the average scheme should be used to compute C^m .

Method (FMM) in [15] to be employed in solving (6.8) and (6.10), as shown in the following section.

6.4 The Fast Multipole Method (FMM)

The solution of (6.8) can be obtained through solutions of the equation having the form

$$\mathbf{V} = \mathbf{M}\mathbf{I} \quad (6.12a)$$

where

$$\mathbf{V} = \begin{bmatrix} 0 \\ \mathbf{V}_{12} \mathbf{q}_1^{1,\text{unif}} \\ 0 \end{bmatrix} \quad (6.12b)$$

and

$$\mathbf{I} = \begin{bmatrix} \mathbf{q}_1^{1,\text{excess}} \\ \mathbf{q}_2^{1,\text{excess}} \\ \mathbf{q}_{\text{Tplane}}^{1,\text{excess}} \end{bmatrix} \quad (6.12c)$$

or

$$\mathbf{V} = \begin{bmatrix} \mathbf{V}_{21} \mathbf{q}_2^{2,\text{unif}} \\ 0 \\ 0 \end{bmatrix} \quad (6.12d)$$

and

$$\mathbf{I} = \begin{bmatrix} \mathbf{q}_1^{2,\text{excess}} \\ \mathbf{q}_2^{2,\text{excess}} \\ \mathbf{q}_{\text{Tplane}}^{2,\text{excess}} \end{bmatrix} \quad (6.12e)$$

and

$$\mathbf{M} = \begin{bmatrix} \mathbf{M}_{11} & \mathbf{M}_{12} & \mathbf{M}_{13} \\ \mathbf{M}_{21} & \mathbf{M}_{22} & \mathbf{M}_{23} \\ \mathbf{M}_{31} & \mathbf{M}_{32} & \mathbf{M}_{33} \end{bmatrix} \quad (6.12f)$$

In a similar manner, the solution of (6.10) can also be obtained.

Equations (6.8) and (6.10) can be solved either directly by LU decomposition, or by iterative techniques such as the Generalized Conjugate Gradient (GCR) or the Generalized Minimum Residual (GMRES). If the MoM matrix, represented by \mathbf{M} in (6.12a), has dimensions $N \times N$, then a direct method, for example LU decomposition, would require $O(N^3)$ operations. If an iterative technique is used to solve the MoM system, the cost would be $O(pN^2)$, where p is the number of iterations since a matrix-vector product is required in each iteration. This product has the form $\mathbf{M}\mathbf{I}_q$ where \mathbf{I}_q is a vector of trial charge coefficients in the q th iteration. The FMM can be invoked to compute this product in an extremely efficient manner, requiring only $O(M)$ operations per iteration, as demonstrated in [12]. This results in an overall complexity for the FMM-based iterative technique of $O(pM)$, where p is the number of iterations [13], [14].

The approach followed here, and explained in detail in [15], is to use Anderson's FMM technique, which is based on the use of Poisson's formula to represent the solution of Laplace's equation. The images resulting from the use of the closed-form approximation to the 3-D Green's function G^{3D} has to be accounted for in the FMM. To facilitate the required computation, the entire multiconductor structure and all image patches are enclosed in a large cubical volume (called the parent cube), which is recursively partitioned into eight smaller cubes (termed the child cubes). At the n th level, the problem space has been hierarchically partitioned into 2^{3n} cubes. For each cube at every level, an "outer sphere" approximation is constructed [12], [15]. This approximation permits the computation of the potential at any point outside the sphere, given the potential on its surface due to all enclosed sources. These approximations are constructed in a hierarchical manner to efficiently aggregate source points. Observation points are aggregated in a manner similar to that employed to aggregate source points, by using "inner sphere" approximations that facilitate the computation of the potential at any point inside a sphere, given the potential on its surface from all sources outside it. The surfaces of the conductors are divided into genuine patches, while the images produced by the Green's function lead to the presence of image patches. The observation points correspond only to the centers of the genuine

patches, whereas both genuine and image patches comprise the sources: the potential boundary conditions are enforced only on the conductor surfaces. The overall FMM-based technique for evaluating the matrix-vector product requires an initial potential evaluation due to every source, construction of outer and inner sphere approximations, and a final potential at evaluation at every observation point. Note that given a charge distribution, the FMM obtains the potential values without ever generating the matrix \mathbf{M} .

At present, our FMM implementation works for the case of a single dielectric layer backed by a ground plane, with free space on top. Finite ground planes can be modeled. The extension to an arbitrary number of layers is relatively straightforward and is currently under implementation.

6.5 Numerical Examples

In this section, the usefulness of the above algorithms in the evaluation of the excess capacitance for various representative geometries is demonstrated. It is assumed that all strips considered in this section have negligible thicknesses. Since the excess charges are localized around the discontinuity, the lengths of all strips are truncated to the finite length of l using the following formula:

$$l = 20 (h_2 - h_1) \frac{90^\circ}{\alpha} \quad (6.13)$$

where h_1 and h_2 are the heights of Conductors 1 and 2 from the bottom ground plane, and α is the crossing angle in degrees. The length of a top ground plane l_g , if it exists, is taken to be $2l$. Nonuniform meshing is utilized to discretize both conductors and the top ground plane. Unless otherwise specified, the total numbers of basis functions for 2-D and 3-D problems are 16 and 160 for each strip, respectively, and 625 basis functions are used to model the top ground plane. A maximum of five exponential functions were used to approximate each coefficient function of the Green's function, and the Generalized Conjugate Gradient (GCR) is used to solve the linear system of equations. The CPU time is measured on the Alpha workstation.

As a first example, consider the strip geometry depicted in Fig. 6.3. The width of both strips is 0.16 mm. The equivalent capacitance is computed over a wide range of crossing angles, and the results are shown in Fig. 6.4. The excess charge distribution is plotted in

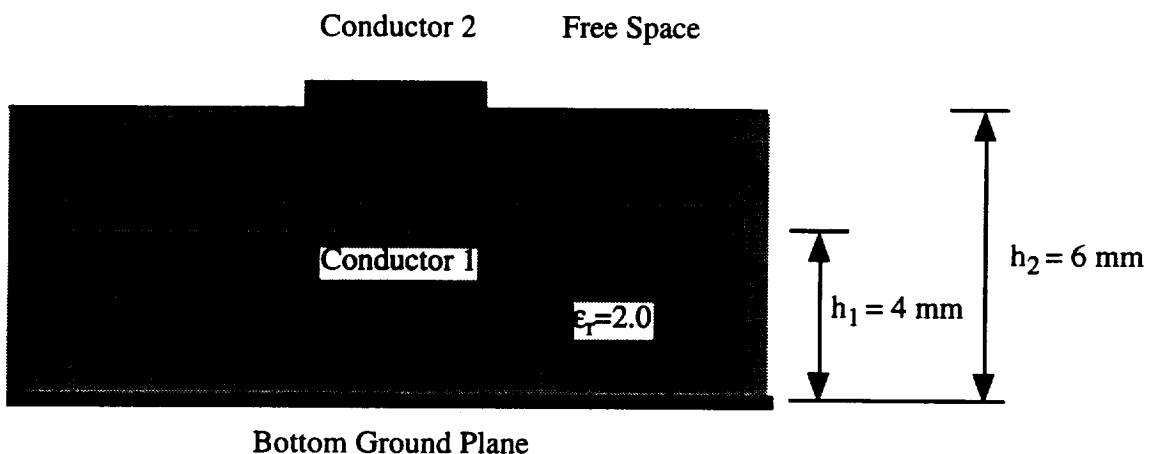


Figure 6.3. Example 1: a microstrip crossover.

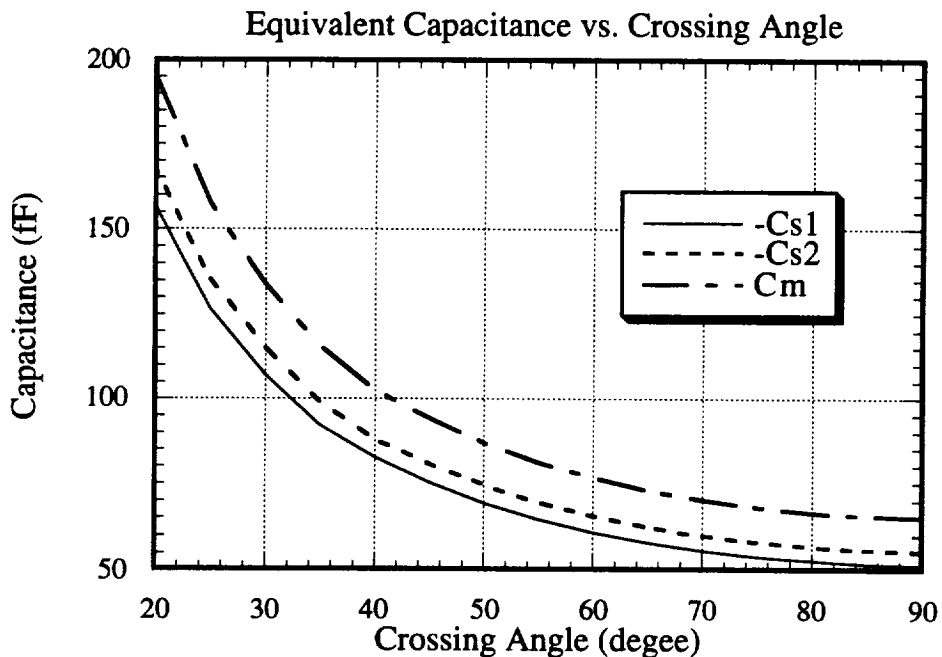


Figure 6.4. Variation of the equivalent capacitance as a function of the crossing angle α .

Fig. 6.5. Table 6.1 shows the comparison data for the orthogonal crossing case. The difference between data in the first and second columns is due to the difference in meshing size and the order of approximation used to obtain the closed-form Green's function. A total of 11.36 sec of CPU time is used to compute the orthogonal case.

Next, consider the crossover structure with a top ground plane shown in Fig. 6.6. The width of the strips is again 1 mm. Figure 6.7 shows the variation of the values of the equivalent capacitance over the height of a top ground plane h_3 . The comparison of the result for $h_3 = 50$ with that for the case without a top ground plane is shown in Table 6.2. A total of 55.11 sec of CPU time is used for the case with a top ground plane.

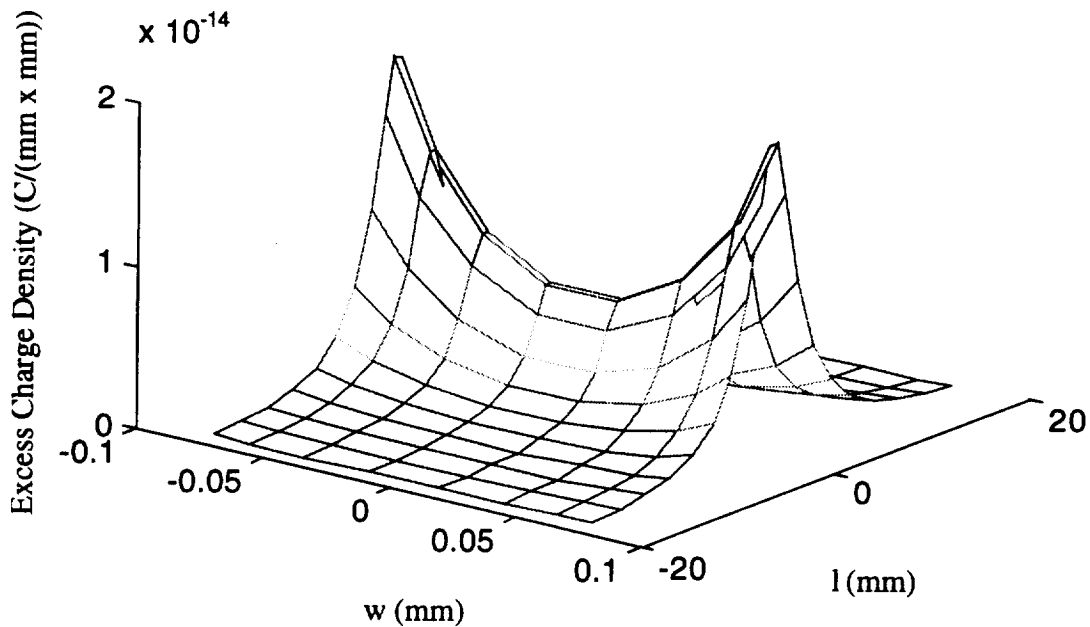
Equation (6.1) is also solved directly for the total charge distribution³ instead of formulating the integral equation in terms of the excess charge distribution, which is the conventional way to find 3-D capacitance matrices. Then, the following formula is used to compute the excess (equivalent) capacitance matrix:

$$\begin{bmatrix} C_1^{1,excess} & C_1^{2,excess} \\ C_2^{1,excess} & C_2^{2,excess} \end{bmatrix} = \begin{bmatrix} Q_1^{1,total} - l * Q_1^{1,uniform} & Q_1^{2,total} \\ Q_2^{1,total} & Q_2^{2,total} - l * Q_2^{2,uniform} \end{bmatrix} \quad (6.14)$$

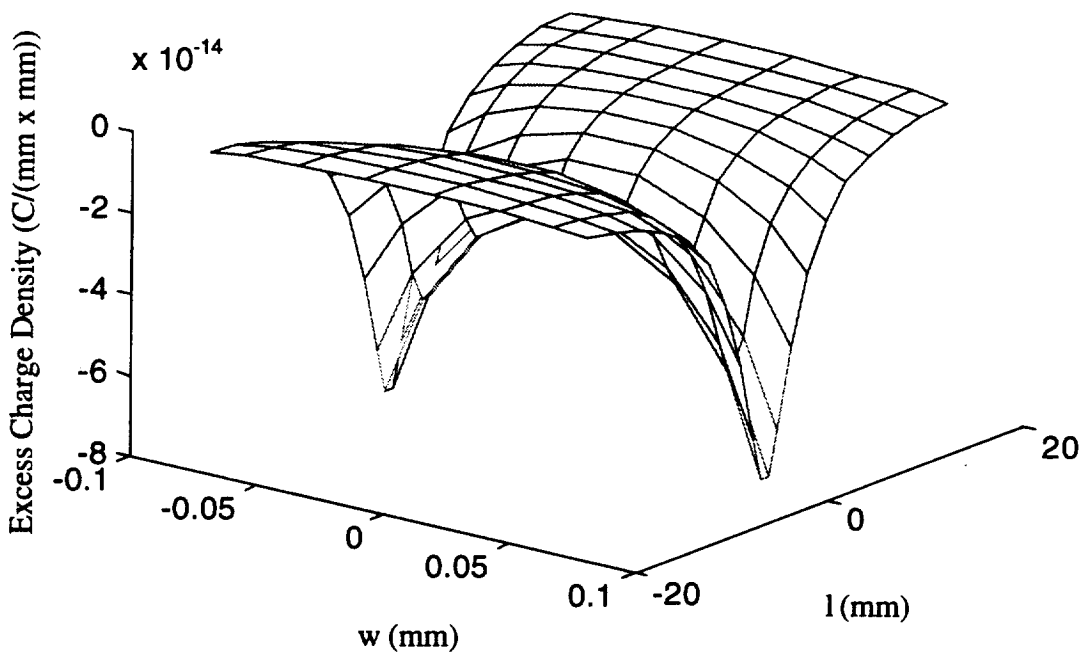
where $Q_j^{i,total}$ is the sum of the total charge distribution on Conductor j with the excitation on Conductor i , and $Q_i^{i,uniform}$ is the sum of the uniform charge distribution on Conductor i . As mentioned in Section 4.1, the major drawback of this approach is that since the excess charge due to the crossover is much smaller than the total charge, the final accuracy in terms of the excess charge is much worse than the accuracy obtained for solving the total charge. Table 6.2 demonstrates this fact.

For the final example, the crossover shown in Fig. 6.3 with $h_1 = 2.5$ mm, $h_2 = 5$ mm, $w_1 = w_2 = 1$ mm and $\epsilon_r = 5$ is considered to demonstrate the application of the Fast Multipole Method (FMM) described in [9], [12]. The FMM is used with the Generalized Minimum Residual (GMRES) routine, as in [12]. The comparison, in terms of the CPU time, with the LU factorization, the Generalized Conjugate Residue (GCR) routine, and the

³The term total charge denotes the sum of uniform and excess charges.

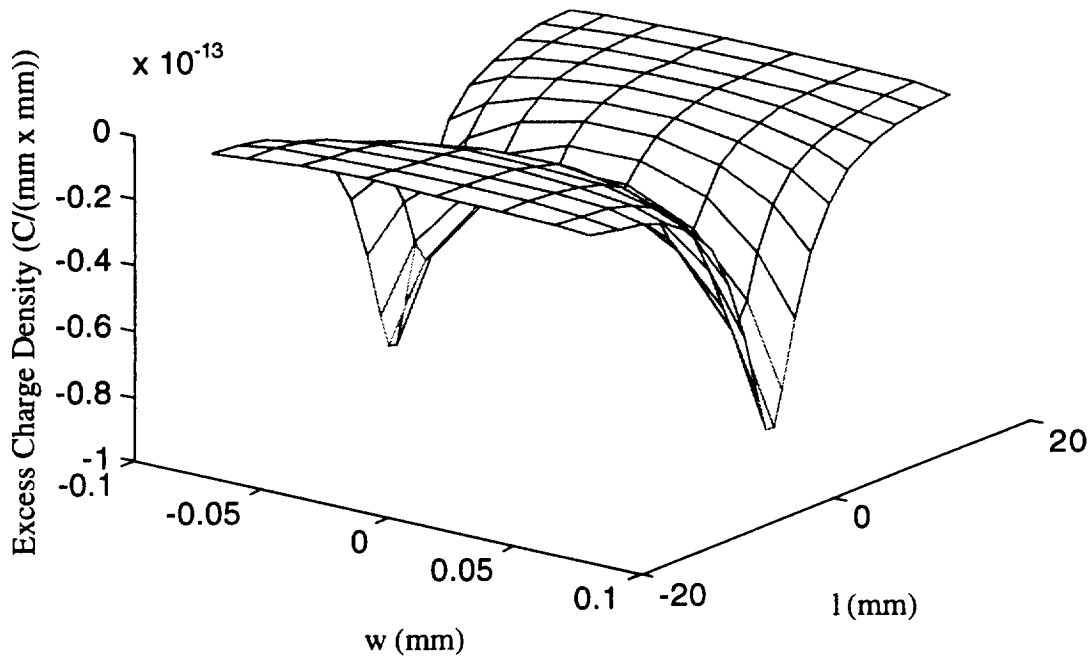


(a)

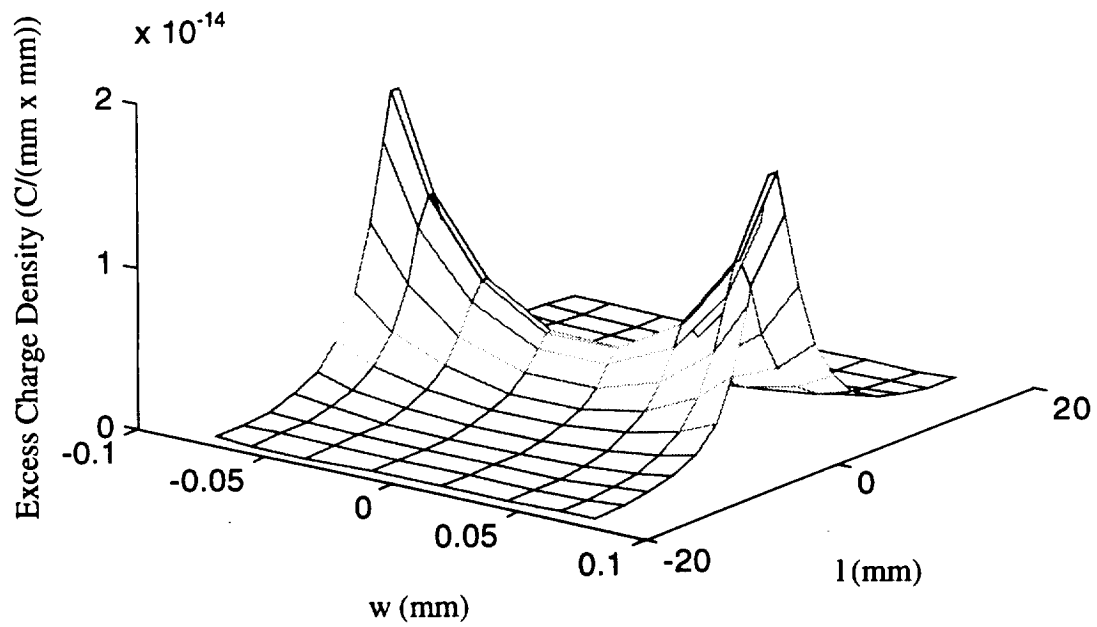


(b)

Figure 6.5. Plots of the excessive charge distributions for (a) q_{11}^{ex} , (b) q_{21}^{ex} , (c) q_{12}^{ex} , and (d) q_{22}^{ex} for Example 1 for the orthogonal crossing case.



(c)



(d)

Figure 6.5. Continued.

Table 6.1. Comparison data for the orthogonal case of Example 1.

	Computation	Data from [2] ⁴	Data from [3]
C^m	64.81 fF	65.12 fF	65.16 fF
C_1^s	-51.30 fF	-51.42 fF	-51.58 fF
C_2^s	-55.10 fF	-55.08 fF	-54.92 fF

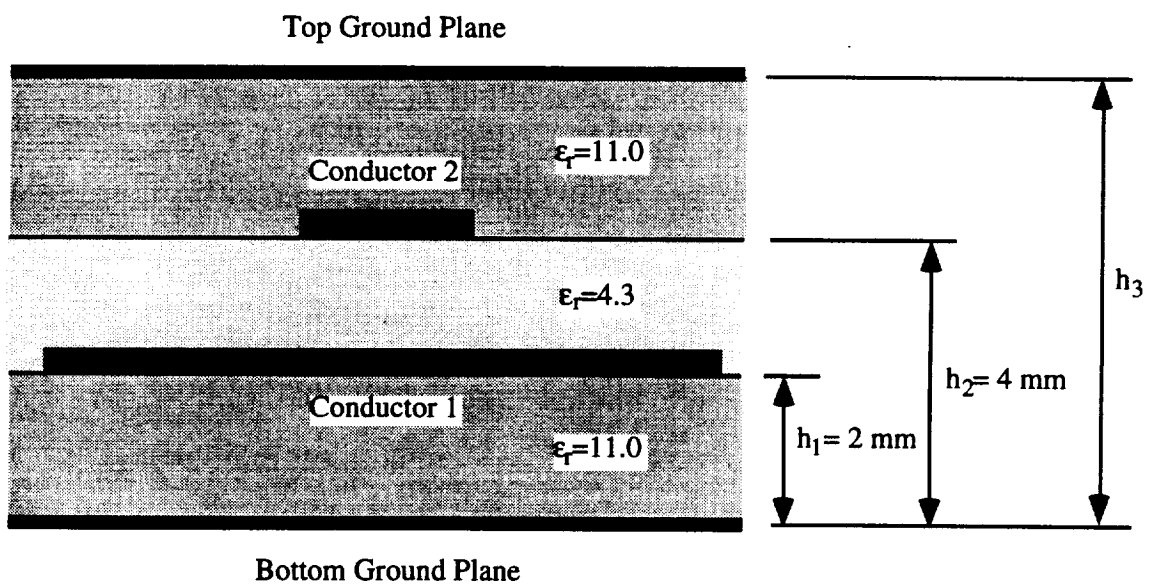


Figure 6.6. Example 2: a strip crossover with a top ground plane (orthogonal crossing case).

⁴The entries in Table 2 in [2] contained errors, and the corrected data were obtained from the authors and given in Table 6.1.

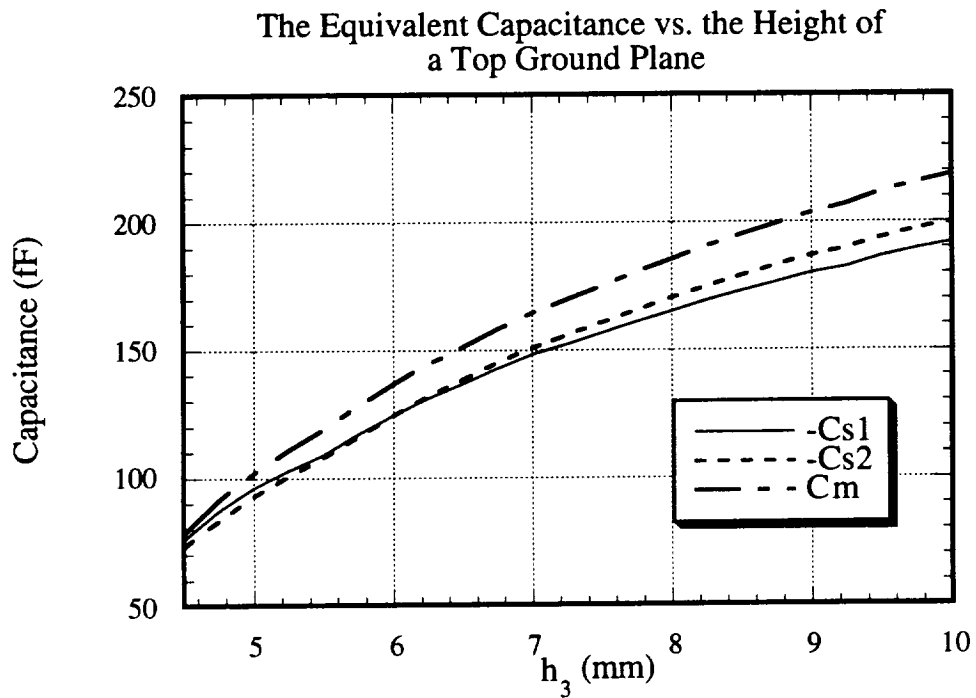


Figure 6.7. Variation of the equivalent capacitance as a function of the height of a top ground plane.

Table 6.2. Comparison data for the orthogonal case of Example 1.

	Without Top Ground		With Top Ground ($h_3 = 50$)
	The Excess Charge Formulation	The Total Charge Formulation	The Excess Charge Formulation
C^m	332.75 fF	309.87 fF	329.46 fF
C_1^s	-291.23 fF	-139.40 fF	-286.20 fF
C_2^s	-298.24 fF	37.11 fF	-296.65 fF

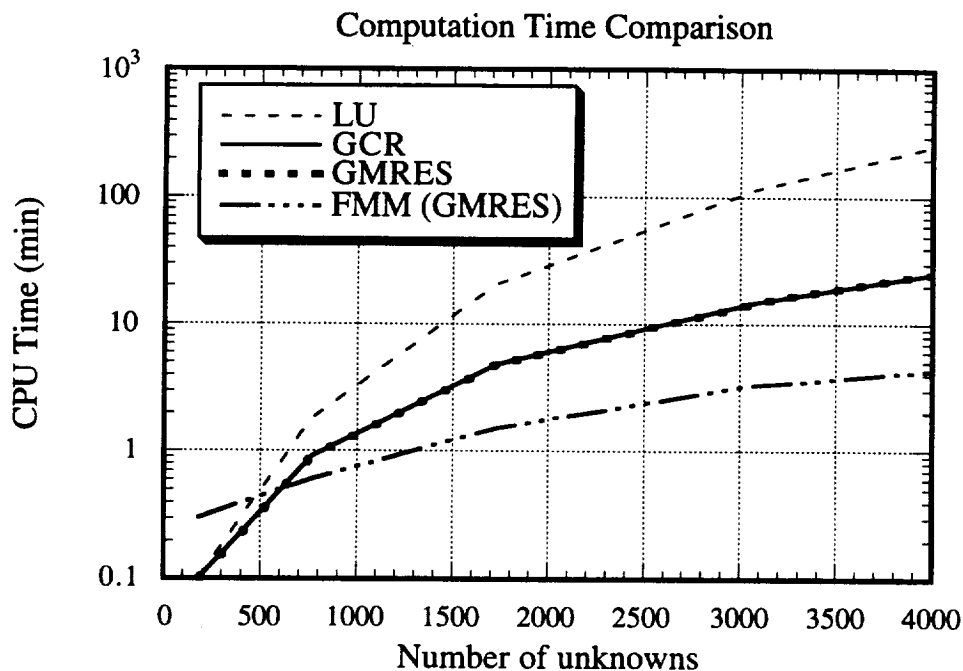


Figure 6.8. Comparison of CPU time used for the LU factorization, GCR, GMRES, and FMM.

Generalized Minimum Residual (GMRES) routine, is given in Fig. 6.8. The result from LU factorization was $C^m = 518.06$ fF, $C_1^s = -415.88$ fF, and $C_2^s = -460.98$ fF. The FMM gave $C^m = 517.0$ fF, $C_1^s = -414.4$ fF, and $C_2^s = -460.1$ fF. Although this particular numerical example can be solved without the FMM, in general, the number of unknowns can be quite large when modeling the thicknesses of the strips and the top ground plane, and the usage of FMM for such cases will significantly improve the computation speed as indicated by Fig. 6.8.

6.6 Summary

The computation of equivalent capacitances of a strip crossover is considered in this chapter. Strips crossing at an arbitrary angle with both top and bottom ground planes are considered for the first time in this chapter. The presented method is based on a static integral equation in conjunction with a closed-form Green's function, and does not involve numerical integrations or infinite summations in the evaluation of the MoM matrix. The application of the Fast Multipole Method to accelerate the computation is also discussed.

6.7 References

- [1] C. H. Chan and R. Mittra, "Analysis of MMIC structures using an efficient iterative approach," *IEEE Trans. Microwave Theory Tech.*, vol. 6, pp. 96-105, January 1988.
- [2] S. Papatheodorou, R. F. Harrington, and J. R. Mautz, "The equivalent circuit of a microstrip crossover in a dielectric substrate," *IEEE Trans. Microwave Theory Tech.*, vol. 38, pp. 135-140, February 1990.
- [3] J. F. Carpentier, P. Pribetich, and P. Kennis, "Quasi-static analysis of skewed transmission lines for MMIC applications," *IEE Proc.-Microw. Antennas Propag.*, vol. 141, pp. 246-252, March 1994.
- [4] J. Martel, R. R. Boix and M. Horno, "Analysis of a microstrip crossover embedded in a multilayered anisotropic and lossy media," *IEEE Trans. Microwave Theory Tech.*, vol. 42, pp. 424-432, March 1994.
- [5] T. Uwano, R. Sorrentino, and T. Itoh, "Characterization of strip line crossing by transverse resonance analysis," *IEEE Trans. Microwave Theory Tech.*, vol. 35, pp. 1369-1372, December 1987.
- [6] E. Pillai and W. Wiesbeck, "Derivation of equivalent circuits for multilayer printed circuit board discontinuities using full wave models," *IEEE Trans. Microwave Theory Tech.*, vol. 42, pp. 1771-1783, September 1994.
- [7] S. Papatheodorou, R. F. Harrington, and J. R. Mautz, "Full-wave analysis of a strip crossover," *IEEE Trans. Microwave Theory Tech.*, vol. 38, pp. 1439-1448, October 1990.
- [8] L. Greengard and V. Rokhlin, "A fast algorithm for particle simulations," *J. Comp. Phys.*, vol. 73, pp. 325-348, 1987.
- [9] L. Greengard, *The Rapid Evaluation of Potential Fields in Particle Systems*. Cambridge, MA : MIT Press, 1988.
- [10] V. Rokhlin, "Rapid solution of integral equations of classical potential theory," *J. Comp. Phys.*, vol. 60, pp. 187-207, September 1985.
- [11] J. Carrier, L. Greengard, and V. Rokhlin, "A fast adaptive multipole algorithm for particle simulations," *SIAM J. Sci. Stat. Comp.*, vol. 9, pp. 669-686, July 1988.
- [12] C. R. Anderson, "An implementation of the fast multipole method without multipoles," *SIAM J. Sci. Stat. Comp.*, vol. 13, pp. 923-947, July 1992.
- [13] K. Nabors and J. White, "FastCap : a multipole accelerated 3-D capacitance extraction program," *IEEE Trans. Computer-Aided Design*, vol. 10, pp. 1447-1459, November 1991.

- [14] K. Nabors and J. White, "Multipole-accelerated capacitance extraction algorithms for 3-D structures with multiple dielectrics," *IEEE Trans. Circuits Syst.-I*, vol. 39, pp. 946-954, November 1992.
- [15] V. Jandhyala, E. Michielssen, and R. Mittra, "Multipole-accelerated capacitance computation for 3-D structures in a stratified dielectric medium," *Int. J. Microwave and Millimeter-Wave Computer-Aided Eng.*, submitted for publication.

CHAPTER 7

SUMMARY AND FUTURE WORK

In this study, computationally efficient and accurate methods to compute the transmission line parameters of interconnections and the equivalent capacitances of discontinuities associated with interconnections were presented based on the quasi-static approximation. An extensive amount of research has already been performed on this subject and various numerical techniques have been developed thus far, as referenced throughout the chapters; however, most of these techniques are applicable to only a certain class of problems or are computationally intensive. For instance, some methods assume conductors to be of zero thickness and are limited by the number of dielectric layers (often two layers), whereas some methods require an evaluation of nested infinite summations, a numerical integration, or modeling of additional unknowns over dielectric interfaces. In contrast, the presented methods are applicable to multiple conductors embedded in multilayered dielectric media, and the cross sections of conductors can be arbitrary although, in the cases analyzed, we have used infinitely thin strips for modeling of discontinuities to simplify the analysis. Moreover, these methods are numerically efficient as they do not involve any of the computationally expensive operations described before.

The computational efficiency of the presented methods is mainly due to the introduction of the closed-form Green's function for a multilayered dielectric medium. Although the concept of the closed-form Green's function first originated in full-wave analysis and had already been applied to a static case using complex images, the closed-form Green's function based on real images, which is computationally more efficient than the method based on complex images, was first developed in this study. In fact, the closed-form Green's function (based on complex images) for static analysis was published at an early stage of this study, and a similar concept using real images was independently inspired by this author. The complete list of expressions for the closed-form Green's functions for a point charge, a uniform line charge, and a semi-infinite uniform line charge, all embedded in a multilayered dielectric medium, was presented in Chapter 2 with the associated closed-form integration formulas for the collocation method.

The closed-form Green's functions derived in Chapter 2 were then applied to solve various electrostatic problems. In Section 3.2, this Green's function was used to solve 2-D electrostatic problems to compute the capacitance matrix of a multiconductor system. In

Chapters 4, 5, and 6, it was used to formulate integral equations in terms of the excess charge distributions to compute the equivalent capacitances of various interconnection discontinuities, such as open ends, bends, various junctions, vias, and crossovers.

The electrostatic solution obtained in Section 3.2 was further used to compute the conductance matrix of a multiconductor system in Section 3.4. The normal component of the electric field at the surfaces of conductors was determined from the charge distribution obtained from Section 3.2; then, it was further related to the shunt current density at the surfaces of conductors and used in the computation of the conductance matrix. Hence, the presented method for the computation of the conductance matrix is perturbational in the sense that the normal component of the electric field at the surfaces of conductors of a lossless system was used to determine the shunt current density.

To compute the inductance and resistance matrices, an analogy between electrostatic and magnetostatic problems was presented in Section 3.3. Then, an equivalent electrostatic problem was solved instead of a magnetostatic problem, and the inductance matrix was obtained from the capacitance matrix of the equivalent electrostatic problem in Section 3.3. The conduction current density on the surfaces of conductors was also obtained from the surface charge density of the equivalent electrostatic problem, and it was used to determine the resistance matrix in Section 3.5. To include losses due to imperfectly conducting ground planes, coupled integral equations were formulated in Section 3.5 to obtain the current densities on the surfaces of the ground planes.

Throughout the chapters, the results obtained from the presented methods were compared with other published results including some experimental results and, in general, a good match was obtained.

The Fast Multipole Method (FMM) is a recently developed algorithm to accelerate the evaluation of potentials in large system. Some authors applied this multipole algorithm to a multilayered case by modeling the polarization charge on dielectric interfaces; however, a more efficient implementation of the multipole algorithm to a multilayered case may be the use of the closed-form Green's function. At the present time, the multipole algorithm has been applied to the closed-form Green's function for only a stratified medium where all conductors are located in the same dielectric layer. In this thesis, this method was considered in the computation of the equivalent circuit of a crossover to obtain further savings in the computation time and memory; a similar approach can also be applied to

computation of the other discontinuities. The implementation of the multipole algorithm to a more general closed-form Green's function, in which conductors can be located in any layer, would be a good subject for future work.

Although only the capacitive nature of the discontinuity is considered in this thesis, in general, the effect of the discontinuity will be far more complex and full-wave analysis must be employed to circuits in the high frequency regions. The author is currently investigating the application of the Finite-Difference Time-Domain (FDTD) method to generate the equivalent circuits of discontinuities to account for the frequency-dependent nature of these nonuniform structures.

APPENDIX A

THE REAL-VALUED EXPONENTIAL APPROXIMATION BASED ON THE RELAXATION OF CURVE FITTING

First, we will assume that a function $y(x)$ to be approximated is real valued and nonoscillatory and, furthermore, that its asymptotic value is zero. The latter assumption can easily be satisfied if the function is limited at infinity. Our goal is to find the right-hand side of

$$y(x) \equiv f_a(x) = \sum_{i=1}^N f_i(x) = \sum_{i=1}^N C_i e^{\lambda_i x} \quad (\text{A.1})$$

Let us for a moment assume that each first-order function $f_i(x)$ approximates the original function $y(x)$ at some interval around one of the approximation points and is decreasing fast enough so that its value is negligibly small at the approximation points corresponding to larger values of the argument x . Then, we can safely determine one of the first-order functions, say $f_1(x)$, by neglecting contributions due to the other first-order functions, which are unknowns to be determined. The parameters of $f_1(x)$ can be easily obtained by curve fitting two values of $y(x)$ for some large value of x . In a similar manner, we can find the parameters of the other first-order functions; however, this time we have to take into account contributions due to the previous ones which are already known.

From the above argument, given $2N$ approximation points, the equations used to determine the parameters for the i th first-order function are then written by

$$\lambda_i = \frac{2\pi \ln(y_i(x_{2i-1})/y_i(x_{2i}))}{x_{2i} - x_{2i-1}} \quad (\text{A.2})$$

$$C_i = e^{-\lambda_i x_{2i-1}} y_i(x_{2i-1}) \quad (\text{A.3})$$

where

$$y_i(x_j) = y_{i-1}(x_j) - f_{i-1}(x_j); \quad j = 1, \dots, 2N \quad (\text{A.4})$$

In the above, $y_0(x_j)$ is equal to $y(x_j)$. Let us now consider the case in which the value of a first-order function is not negligible at the other approximation points. In this

case, if we perform the above procedure, there will be some difference between the original and the approximated functions since we have ignored contributions due to some of the first-order functions. In such a case, to reduce this difference, we can iterate the above procedure including the contributions from all other first-order functions which were obtained from the previous iteration. Thus, for the k th iteration, (A.4) must be modified as

$$y_i^{(k)}(x_j) = y(x_j) - \sum_{l=1}^{i-1} f_l^{(k)}(x_j) - \sum_{l=i+1}^N f_l^{(k-1)}(x_j); \quad j = 1, \dots, 2N \quad (\text{A.5})$$

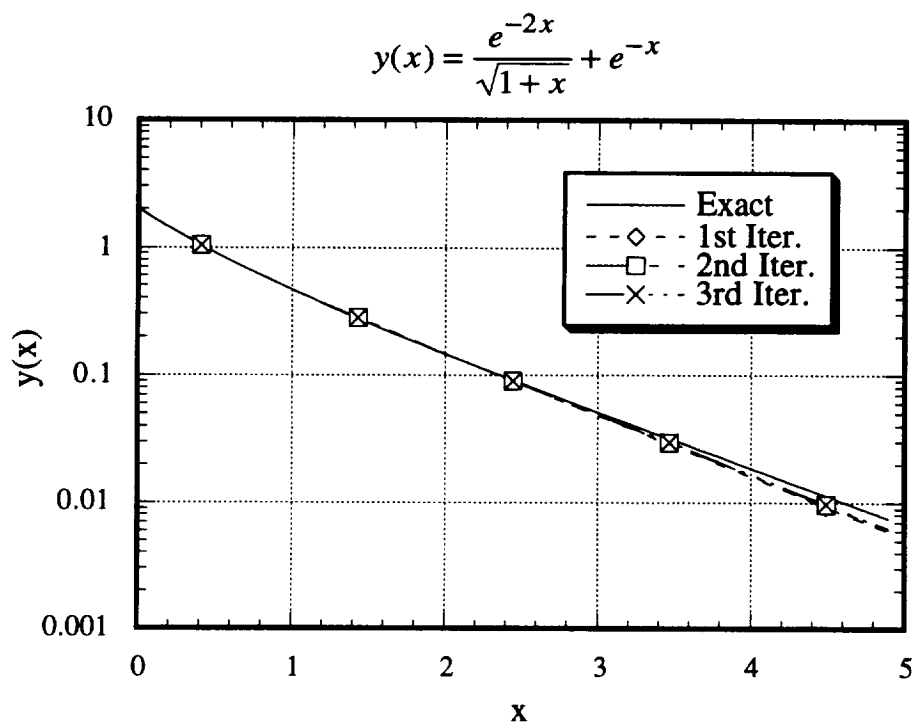
It can easily be shown that if $y(x)$ had N distinct eigenvalues, by iterating the above procedure, the approximate function will converge to the original function. However, in general, the approximate function will never be exact and the iteration must be stopped at some point at which the approximate function is *optimal* in the curve-fitting sense. Since our curve-fitting algorithm, most likely, has the largest relative error for values of x between x_{2N-1} and x_{2N} , one can check the approximated value with the exact value at any point in this interval for the convergence criterion. In some cases, if the desired accuracy can not be achieved, then one should increase the number of exponentials. This case can be determined by checking the difference between the computed parameters of $f_i^{(k)}$ and $f_i^{(k-1)}$.

The described method allows one to find the parameters of an approximating function one-by-one directly without solving a system of nonlinear or linear equations and does not require an original function to be monotonic. Moreover, the limiting values of the approximated function match exactly with the original function.

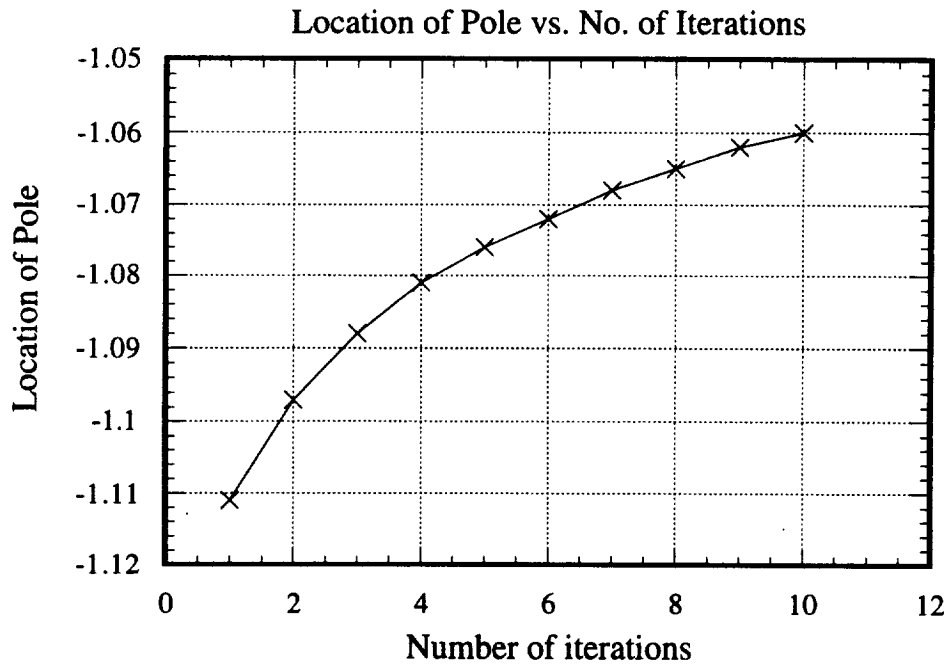
Finally, to demonstrate the method, the following testing function is approximated and the results are shown in Fig. A.1:

$$y(x) = \frac{e^{-2x}}{\sqrt{1+x}} + e^{-x} \quad (\text{A.6})$$

As illustrated in Fig. A.1(b), to find the exact location of the pole at -1 , we need a large number of iterations; however, since our goal is to approximate the overall function, only a few iterations were needed to approximate the function. To locate the poles exactly,



(a)



(b)

Figure A.1. (a) Comparison of approximated and exact values of Equation (A6) and (b) the convergence of the location of the smallest pole (-1) with the number of iterations.

one should consider other methods such as those based on pencil of functions [1] or the Prony approximation [2].

A.1 Reference

- [1] S. L. Marple, *Digital Spectral Analysis*. Englewood Cliffs, NJ: Prentice-Hall, 1987.
- [2] Y. Hua and T. K. Sarkar, "Generalized pencil-of-function method for extracting poles of an EM system from its transient response," *IEEE Trans. Antennas Propagat.*, vol. 37, pp. 229-234, February 1989.

APPENDIX B

THE GREEN'S FUNCTION EXPRESSION FOR A STRIP LINE

Solving Poisson's equation with separation of variables, the Green's function for the strip transmission line case with the distance h between two ground planes (see Fig. B.1) can be written as follows (see [1]):

$$G(x, y|x', y') = \frac{1}{\pi\epsilon} \sum_{n=1}^{\infty} \frac{1}{n} \sin\left(\frac{n\pi y}{h}\right) \sin\left(\frac{n\pi y'}{h}\right) e^{-(n\pi|x-x'|/h)} \quad (\text{B.1})$$

The above expression for the Green's function can be easily integrated analytically over the pulse basis function. This summation is quickly converging due to the decaying exponential factors, and only a few first terms are needed; for instance, four digits of accuracy can be obtained using less than five terms for $|x-x'|/h > 0.5$. However, when $|x-x'|/h$ is small, the summation converges rather slowly, and the use of this Green's function expression should be avoided.

Fortunately, the above series can be summed up using the following formula:

$$\sum_{k=1}^{\infty} \left(\frac{1}{k}\right) e^{-kb} = -\ln|1 - e^{-b}| \quad (\text{B.2})$$

and the resulting closed-form expression is given by [(1.462), 2]

$$G(x, y|x', y') = \frac{1}{4\pi\epsilon} \ln \left[\frac{\sinh^2 \left[\frac{\pi(x-x')}{2h} \right] + \sin^2 \left[\frac{\pi(y+y')}{2h} \right]}{\sinh^2 \left[\frac{\pi(x-x')}{2h} \right] + \sin^2 \left[\frac{\pi(y-y')}{2h} \right]} \right] \quad (\text{B.3})$$

This expression for the Green's function can also be obtained using the conformal mapping and the method of images (see Ch. 10 in [3]). The major disadvantage of this expression compared to (B.1) and (2.24a) is that the closed-form integration over the pulse basis function is unappealing; hence, the numerical integration scheme is unavoidable. Therefore, this form of the Green's function must be only used when $|x-x'|/h$ is small. As discussed in [4], to integrate (B.3) numerically, it is convenient to rewrite this expression by extracting the singularity as

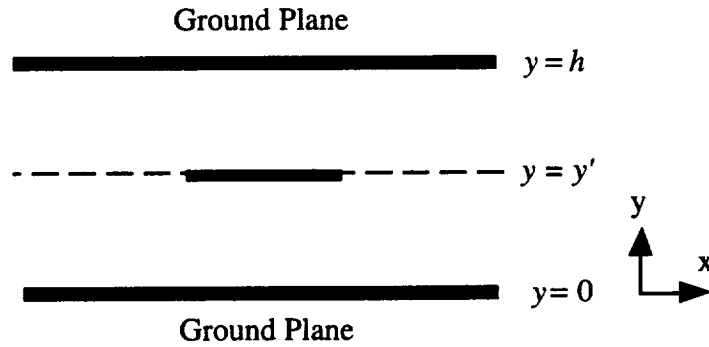


Figure B.1. A strip transmission line.

$$G(x, y|x', y') = -\frac{1}{4\pi\epsilon} \ln[(x - x')^2 + (y - y')^2] + g(x, y|x', y') \quad (\text{B.4})$$

where

$$g(x, y|x', y') = \frac{1}{4\pi\epsilon} \ln \left[\frac{[(x - x')^2 + (y - y')^2] \left[\sinh^2 \left[\frac{\pi(x - x')}{2h} \right] + \sin^2 \left[\frac{\pi(y + y')}{2h} \right] \right]}{\sinh^2 \left[\frac{\pi(x - x')}{2h} \right] + \sin^2 \left[\frac{\pi(y - y')}{2h} \right]} \right] \quad (\text{B.5})$$

Now the first term in (B.4) can be analytically integrated over a line segment using the formula given in [5], but the second term must be integrated numerically.

B.1 Reference

- [1] R. E. Collin, *Field Theory of Guided Waves*, 2nd ed. New York: IEEE, 1991.
- [2] I. S. Gradshteyn and I. M. Ryzhik, *Table of Integrals, Series, and Products*, corrected and enlarged ed. San Diego, CA: Academic, 1980.
- [3] P. M. Morse, *Methods of Theoretical Physics*, vol. 2. New York, NY: McGraw-Hill, 1953.
- [4] W. T. Weeks, "Calculation of coefficients of capacitance of multiconductor transmission lines in the presence of a dielectric interface," *IEEE Trans. Microwave Theory Tech.*, vol. 18, pp. 35-43, January 1970.
- [5] D. R. Wilton et al., "Potential integrals for uniform and linear source distributions on polygon and polyhedral domains," *IEEE Trans. Antennas Propagat.*, vol. 32, pp. 276-281, March 1984.



